CZECH TECHNICAL UNIVERSITY IN PRAGUE

FACULTY OF BIOMEDICAL ENGINEERING
Department of Biomedical Technology

Development of Melt Electro written (MEW) PCL fibrous scaffolds for ligament-bone tissue regeneration.

Master thesis

Study programme: Biomedical and Clinical Engineering

Author of the master thesis: Daan Wolters
Supervisor of the master thesis: Ing. Jakub Rálf, Ph.D.

Kladno, August 2022

MASTER'S THESIS ASSIGNMENT

I. PERSONAL AND STUDY DETAILS

Student's name: **Wolters Daan** Personal ID number: **499485**
Faculty: **Faculty of Biomedical Engineering**
Department: **Department of Biomedical Technology**
Study program: **Biomedical and Clinical Engineering**

II. MASTER'S THESIS DETAILS

Master's thesis title in English:

Development of Melt Electro written fibrous materials for ligament/bone tissue regeneration

Master's thesis title in Czech:

Vývoj vlákenných materiálů pro regeneraci vazivové/kostní tkáně metodou MEW

Guidelines:

Ligament reconstruction using autograft or allograft has significant complications. Melt Electrowriting (MEW) is an emerging technique that could be used to mimic collagen fibres and thus tissue engineer new ligaments. Use MEW to engineer a scaffold that could develop into ligament tissue in the patient's body and integrate into adjacent bone tissue. Design and optimise a scaffold that mimics the crimp and nonlinear mechanical response shown in ligament tissues. Design an intermediate region between the scaffold and already developed bone scaffold, which mimics the bone ligament junction in native tissues. Use 3D CAD models to predict and optimise the nonlinear mechanical response of the scaffold, map and validate the stress distribution in the developed intermediate region and further optimise this region. Biologically evaluate produced scaffolds to improve the performance of the scaffold.

Bibliography / sources:

[1] Robinson, T. M., Hutmacher, D. W., Dalton, P. D. , The Next Frontier in Melt Electrospinning: Taming the Jet, Advanced Functional Materials, ročník 29, číslo 44, 2019, https://doi.org/10.1002/adfm.201904664
[2] Rossetti, L., Kuntz, L. A., Kunold, E., Schock, J., Müller, K. W., Grabmayr, H., Stolberg-Stolberg, J., Pfeiffer, F., Sieber, S. A., Burgkart, R., Bausch, A. R, The microstructure and micromechanics of the tendon–bone insertion, Nature Materials, ročník 16, číslo 6, 2017, https://doi.org/10.1038/nmat4863
[3] Lim, W. L., Liau, L. L., Ng, M. H., Chowdhury, S. R., Law, J. X., Current Progress in Tendon and Ligament Tissue Engineering, Tissue Engineering and Regenerative Medicine, ročník 16, číslo 6, 2019, https://doi.org/10.1007/s13770-019-00196-w

Name of master's thesis supervisor:

Ing. Jakub Ráfl, Ph.D.

Name of master's thesis consultant:

Dr. David Hoey, Associate Professor, University of Dublin

Date of master's thesis assignment: **02.03.2022**
Assignment valid until: **30.09.2023**

doc. Ing. Martin Rožánek, Ph.D.
Head of department

prof. MUDr. Jozef Rosina, Ph.D., MBA
Dean

DECLARATION

I hereby declare that I have completed this thesis with the topic "Development of Melt Electro written (MEW) PCL fibrous scaffolds for ligament-bone tissue regeneration**.**" independently, and that I have attached an exhaustive list of citations of the employed sources.

I do not have a compelling reason against the use of the thesis within the meaning of Section 60 of the Act No. 121/2000 Sb., on copyright, rights related to copyright and amending some laws (Copyright Act).

In Kladno 11-08-2022

Daan Wolters

ACKNOWLEDGEMENTS

I would like to thank my consultant dr. David Hoey for the support and guidance throughout the entire project. I would like to express my gratitude to both Angelica Federici and Carolina Martins, for their training and guidance on operating the MEW printer during the year. Additionally, I would like to thank Peter O’Reilly for help and training with the mechanical testing of the MEW printed scaffolds. Finally, I’d like to express my gratitude the team of Hoey Lab for support.

Master Thesis title:

Development of Melt Electro written (MEW) PCL fibrous scaffolds for ligament-bone tissue regeneration.

Abstract:

Anterior Cruciate ligament (ACL) injury is a common soft tissue injury. The ACL plays an essential role in the stability of the knee joint and, due to its poor vascularity, has limited healing capacity. Current ACL injury treatments have several disadvantages, including osteoarthritis and ligament rupture, leading to the need of tissue engineered (TE) solutions to ACL injury. [74] Melt Electrospinning Writing (MEW) is a recently developed technology which allows for the fabrication of controlled fibrous architectures reminiscent of the native extracellular matrix (ECM) of ligament and bone tissues. [47] Printing methods for a suitable scaffold for bone TE has been established, and ligament scaffolds have been explored in the Hoey lab. [68] This study aims to further explore the development of a suitable scaffold for ligament tissue engineering, and to develop a biphasic MEW printed scaffold which includes a bone and a ligament region.

Key words:

Melt Electrowriting, tissue biomechanics, ligament tissue engineering, biphasic scaffold design, FEA

Table of Contents

List of symbols and abbreviations

ACL: anterior cruciate ligament
BLJ: Bone Ligament Junction
TE: tissue engineering
MEW: melt Electrowriting
ECM: extracellular matrix
CTS: critical translation speed
TS: translation speed
FEA: finite elements analysis
MPa: Mega pascal
Wave printing speed: TS at which the crimped fibres are printed
Vertical printing speed: TS at which the vertical cross fibres are printed in the wave model.

List of tables and figures

1 Introduction

Ligaments are tissues that mainly contain type I and type IX collagen, proteoglycans and a small amount of elastin. Ligaments play a crucial role in the stabilization of joints. Unfortunately, ligaments are prone to injury, in fact one of the most prevalent soft tissue injuries is an Anterior Cruciate Ligament (ACL) injury. Injuries to this ligament often require medical solutions, 200.000 ACL reconstruction surgeries are performed annually in the United states, resulting in a significant economic burden. [1] To make matters worse, the rate of ACL injuries has been increasing significantly in the past decade, especially under athletic young adults and adolescents. [77] This trend is particularly worrisome as ACL injury often requires the patient to undergo ACL reconstruction, one of which side effects is the development of osteoarthritis in the knee joint 20 years after operation. [78]

The current gold standard for ACL reconstruction is to harvest a piece of another tendon or ligament from the patient's body to replace the damaged, or broken ACL. [4] This procedure has significant complications including donor site morbidity, degradation of knee cartilage and mechanical graft failure. [12,79] Resulting in a growing clinical interest in alternative solutions to substitute the injured ligament. Several solutions have been proposed including synthetic grafts or harvested collagen sheets. [8, 37]. Despite numerous attempts to mimic the native tissue, mimicking the biomechanics and native tissue's extracellular matrix (ECM) has proven to be quite elusive. [26] Ligaments are highly organized and consist of collagen fibrils with a crimped architecture. [4] This architecture is responsible for high tensile strength and a nonlinear response to tensile loading. [11] There have been several attempts at mimicking this nonlinear response. The problem is that current solutions match the mechanical properties but lack the porosity necessary for proper biological integration. [34,44] Or that the scaffolds do have the necessary porosity, and promote cell integration, but lack sufficient mechanical strength to bear the loads usually placed upon an ACL. [8]

1.1 Overview of the current state of the art

1.1.1 Ligament

A ligament is a band of regularly oriented, poorly vascularised, dense connective tissue that is connected to two different bones, with its primary function being to transmit force as well as limit movement between two said bones. [1]

A specific ligament which biomedical research has focussed on, is the anterior Cruciate Ligament (ACL), which connects the femur and the tibia to one another at the knee joint. The ACL is one of the most frequently injured ligaments. The ACL serves there as a joint stabiliser, opposing anterior tibial translation, and medial rotation of the knee joint. The ACL is named for its relationship with the posterior cruciate ligament (PCL), both ligaments together resembling a cross, with the ACL being located anterior to the PCL.

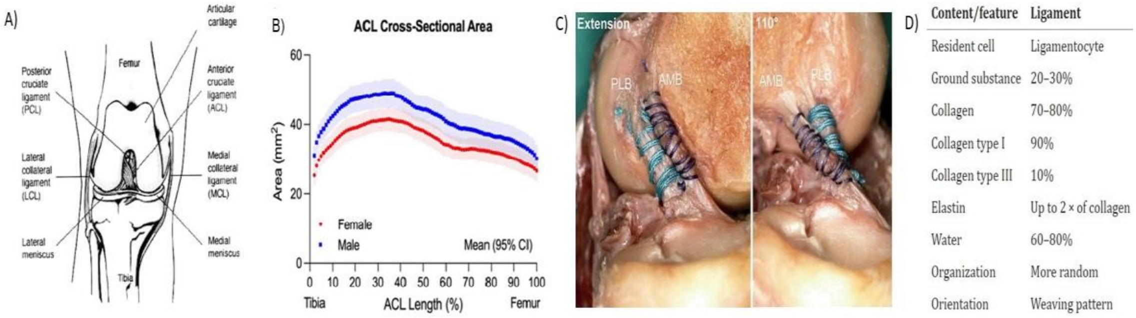

Content/feature	Ligament
Resident cell	Ligamentocyte
Ground substance	20–30%
Collagen	70–80%
Collagen type I	90%
Collagen type III	10%
Elastin	Up to 2 × of collagen
Water	60–80%
Organization	More random
Orientation	Weaving pattern

Figure 1: A) Ligaments surrounding the in the knee joint. [5] B) Plot of cross section area of ACL compared to position along ACL length for each sex. [3] C) Photo image of the anteromedial bundle (AMB) and the posterolateral bundle (PLB) in the ACL, the AMB and PLB are not isometric, and the AMB is tightened during rotation and flexion [2] D) Table of content of a ligament, percentages of. [4]

The ACL is surrounded by a synovium of the knee joint, resulting in the ACL being both extra-synovial and intra-articular.[6]

The ACL itself is white in colour, has a mean length of 32 mm, and ranges between 22 and 42 mm, varying individually. The shape cross-section of the ACL can only be described as irregular. The size of the cross-sectional area varies throughout the length of the ligament, ranging from 30 to 41 mm^2 and is generally larger in Males as seen in figure 1b. [3] The ACL is generally viewed as being made up of two main bundles, the anteromedial bundle (AMB) and the posterolateral bundle (PLB), named after their respective positions in the ACL. Both bundles have different loading patterns, as the AMB shows a greater increase in length during flexion, this is showcased in figure 1c. [2]

1.1.1.1 Ligament composition

Ligaments, such as the ACL, are tissues with a relatively small cell population in relation to the tissue size, with the cell population only making up a small percentage of the tissue volume. 90-95% of the cell population consists of ligamentocytes, which are ligament specific fibroblast. These cells are responsible to maintain the homeostasis of the tissue, are involved in Extracellular Matrix (ECM) synthesis, and have a low metabolic rate. The rest of the cell population consists of chondrocytes, synovial or vascular cells. [2]

The main component of a ligament is the ECM, which is mainly made up of collagen fibres, surrounded by elastin and organised in bundles in the longitude direction of the ligament. Collagen fibres make up 70-80% of the dry mass, the collagen is predominantly Collagen type I (90% of collagen), with collagen type III being present. The rest of the dry mass is made up ground mass consisting of elastin (5% of dry-mass) proteoglycans (<1% of dry mass), and adhesion proteins. [4] The main functions of ground mass are to support the binding of cells to the matrix, to trap and store water, and to act as a medium to support diffusion/transport between blood and ligamentocytes. The proteoglycans serve to attract water, which makes up 60% of the wet mass of a ligament.[12]

1.1.1.2 Ligament structure

The ACL has an anisotropic, highly organized structure with collagen fibres being organized into bundles parallel to the longitudinal axis. These collagen molecules are organised into collagen fibrils, the fibrils being organised into fibres, subfascicles, fascicles, and tendon units, this organisation is further detailed in figure 2A. [4] These bundles are organised hierarchically into larger and larger bundles, and strongly resemble the structural organisation of a rope. These bundles are largely responsible for the ligament's ability to resist mechanical loading in the longitudinal direction.

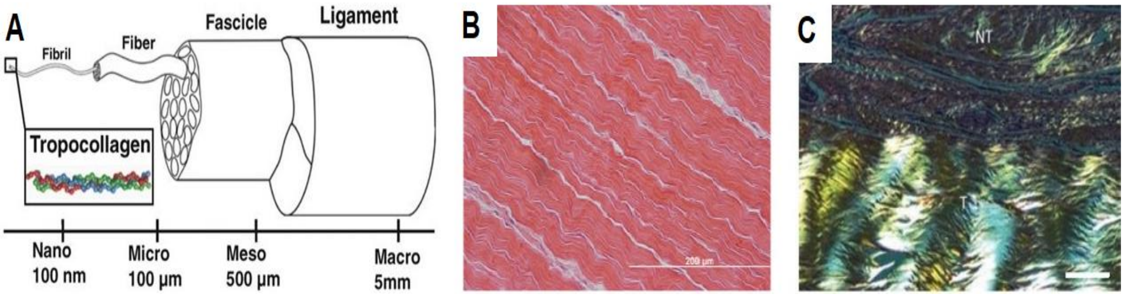

Figure 2: A) schematic overview of the hierarchical organisation of a ligament. [4] B) H&E staining of sheep ACL, scale bar notes 200µm [7] C) Polarised light microscopy of ACL tissue (T) next to newly engineered tissue (NT) lacking the same crimped pattern, scale bar denotes 10mm [8]

In the ACL, both the collagen fibrils and fibres, show a longitudinally repeated crimp pattern. This pattern can be observed in figure 2B, C, and is repeated for every 45-60µm, dependent on its location in the ligament. Therefore, one crimp is between 22-30 µm in length, [2] being 25µm on average, with 5 µm being the average height of these crimp patterns. [9]

This crimp pattern plays a key role in the viscoelastic properties of the ligament, when the ligament is placed under stress, the crimp pattern becomes undone, and the collagen fibres stretch out into a straight line, without offering much resistance. [11] This crimp pattern is being caused by Actin filaments and myofibroblast. Actin filaments and myofibroblasts exert a contractile force on the collagen fibres, causing it to fold and to assume its curved crimp pattern. [10] Later research also showed a link between the density of myofibroblasts and the frequency of the crimp pattern. [9]

1.1.1.3 Biomechanics

Ligaments (and tendons), when placed under a tensile load in the longitudinal direction, have a quite unique non-linear stress response. The stress/strain curve of a ligament under these circumstances can be divided up into three different parts: A toe region, a linear region and a failure region. This non-linear response is related to the discussed crimp pattern. At a low strain, only the actin filaments, responsible for keeping the collagen fibres in a crimped pattern, are strained, allowing the collagen fibres to stretch out to a straight line.[12] When at 2-3% strain, the collagen fibres have completely lost their crimped pattern and the linear region of the ligament starts. In this region, the straight collagen fibres show a linear elastic stress response. Both deformations are elastic, and when the stress is removed the collagen fibres are shown to regain their crimped patterns. [13] After 6% strain, while still showing a linear stress response, microscopic mechanical failures in the ligament start occurring. These failures allow the collagen fibres to slide past one another and result in single fibres rupturing. These microscopic failures cause the ligament to be unable to return to its pre-loaded state. Therefore after 6% strain, when these microscopic failures start to occur, the ligaments undergo plastic deformation.[14] These microscopic failures continue to build up during elongation, eventually resulting in complete failure of the ligament. Rupture of the ligament itself is usually observed around 10 percent strain, hence this region is referred to as the failure region.[7] These elastic properties of the ligament play a key role in protecting the joint, as a ligament can

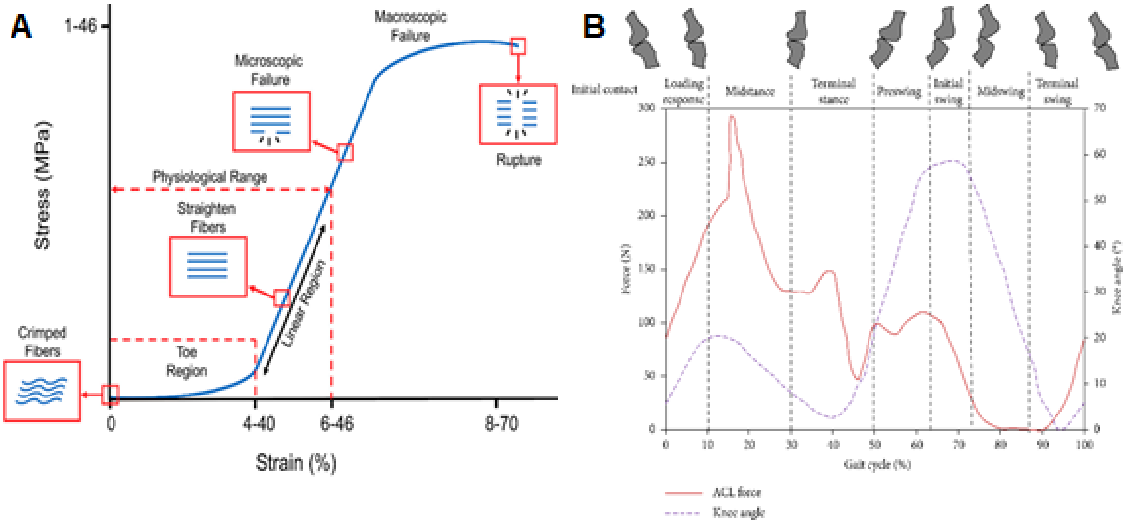

Figure 3: A) The stress strain curve of a ligament [14] B) Load placed upon the ACL in Newtown during the different phases of the gait cycle. [15]

elastically stretch for up to 6% strain, without compromising its tensile strength, allowing the ligament to function as a shock dampener. [13]

The force that is placed on an ACL during the gait cycle when walking, was first calculated by Morrison. the ACL is placed under loads varying from 155N during heel swing, while reaching up to 300N of force during midstance, when walking. Additional calculations of him showed the force on the ACL reaching 450N while walking up the stairs. Indicating that any solution used to replace the ACL must be able to bear at least 450 N. [15] [16]

Several factors affect the strength of a ligament, this is especially the case for the ACL. The most notable factors are age and sex, which affect the strength of the ACL significantly. Age significantly decreases the ultimate strength and stiffness of a ligament. Histological evaluation of ligaments showed the degree of organisation of a ligament decreases during aging. Calcium deposition in the ligament was detected in subjects aged above 60. [20] Sex is the second major factor in the strength of the ACL, as women are 4 to 6 times more likely to suffer from an ACL injury. Several biomechanical, hormonal, or anatomical factors are responsible for this change. Resulting in the fact the ACL cross-section area is smaller in females, even when adjusted for length. [3] Additionally the concentration of collagen fibrils was found to be higher in males, resulting in a stronger ACL. [22] This difference can be observed from as early an age as 11.[19]

To measure the strength of an ACL a tensile test is preformed, this can be done either with the bone parts attached to the ACL, or with the bone parts removed. Generally testing the ligament with the bone parts attached is favoured, as ligaments themselves tend to slip when being placed in tensile clamps. Additionally, there are two orientations that Ligaments have been mechanically tested in, the tibial and the anatomical orientation.

In the tibial orientation the tensile load is applied perpendicular to the attachment sites of the ACL, distorting the angle present in these sites. In the anatomical orientation, the load is placed in the longitudinal direction of the ACL, this orientation represents the loading the ACL normally experiences more accurately. [17] From said measurements, the failure load of the ACL has been established to be ranging from 2160N (age 22-35) to 658N (age 60-90) in the anatomical orientation. In the tibial orientation the failure load ranged from 1602N to 495N. [18] In table 1 the different findings from mechanical studies in the anatomical direction are shown. Due to different investigations choosing different age groups, the studies are shown seperately.

Study	Age group (years)	Sex N number	Stiffness (N/mm)	Failure load (N)	Energy absorbed (Nm)	Youngs modulus (MPa)
Woo et al. [18]	60-90	Mixed (7F, 2M)	180 ± 25	658N ± 129	1.8 ± 0.5	-
Woo et al. [18]	40-50	Mixed (6F,3M)	220 ± 24	1503 ± 83	6.1 ± 0.5	-
Woo et al. [18]	22-35	Mixed (7M, 2F)	242 ± 28	2160 ± 157	11.6 ± 1.7	-
Noyes et al. [21]	16-26	Mixed (2m, 4F)	182 ± 56	1730 ± 660	12.8 ± 5.5	111 ± 26
Noyes et al. [21]	48-86	Male, 20	129 ± 39	734 ± 266	4.89 ± 2.4	63 ± 24.0
Chandrashekar et al. [23]	26-50	Male, 8	308 ± 89	1818 ± 699	7.28 ± 3.6	128 ± 35
Chandrashekar et al. [23]	17-50	Female, 9	199 ± 88	1266 ± 527	4.69 ± 3.6	99 ± 50

Table 1: Different findings of mechanical testing of human-ACL, showing a decrease in mechanical strength with age, as well as a difference in strength between males and females.

1.1.1.4 Bone-ligament interface

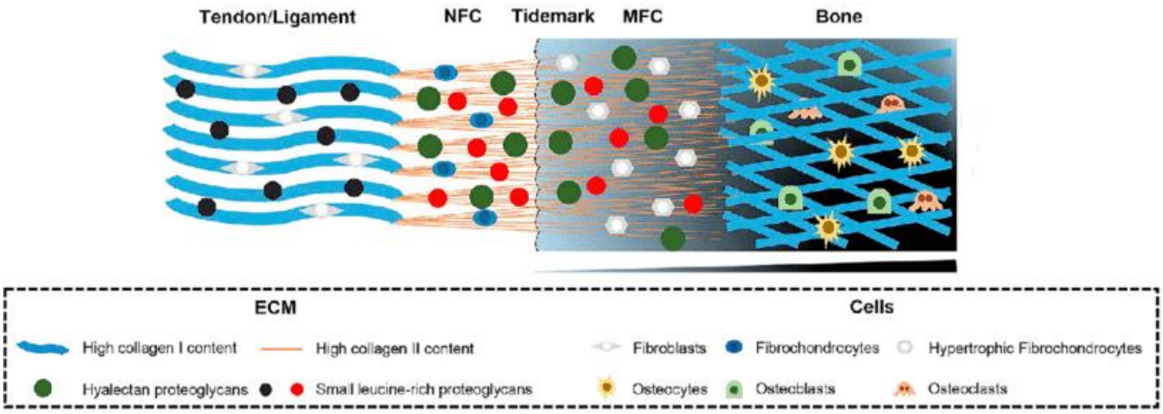

Figure 4: Schematic overview of the ligament bone interface. [27]

Ligaments have a distinct interface region between the ligament itself and bone, connecting the two. This interface can be seen as a complicated composite biomaterial, that allows transfer of force between two tissues with vastly different mechanical properties. This interface is necessary as directly connecting two tissues with different mechanical properties comes with a high chance of mechanical failure. [24] This interface region, called an enthesis in literature, is made up of 4 different regions: the ligament, fibrocartilage, calcified fibrocartilage, and bone. Figure 4 shows a schematic overview of the enthesis, while figure 5 shows electron microscope and histologic images taken from the enthesis. The enthesis can vary significantly depending on the ligament, in the ACL the enthesis is between 300 μm and 500 μm in size. The two fibrocartilage zones are completely avascular, much like other cartilage. These two zones are a slow gradient, changing from a ligament tissue to bone tissue, and feature collagen II fibres connecting form the ligament to the bone, these fibres lose organisation and anisotropy the closer they get to the bone, while increasing in mineralisation. [25] Between the unmineralized and mineralised fibrocartilage there is a basophilic line called the tidemark, this line

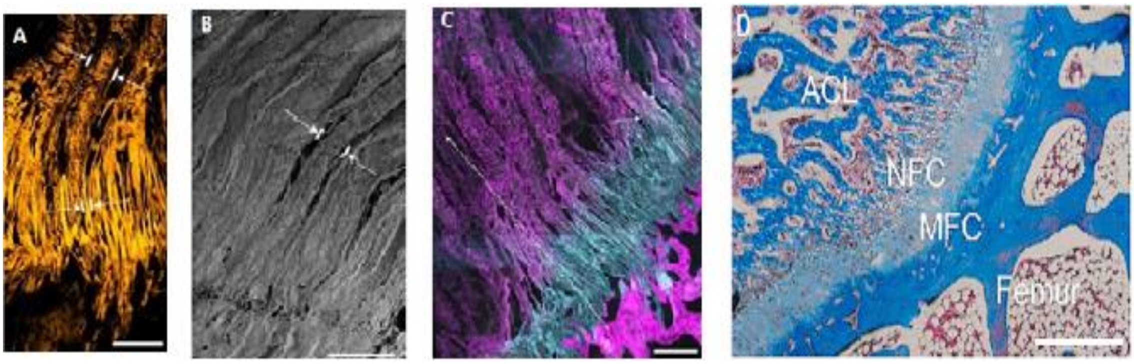

Figure 5: A) Confocal microscopic B) Scanning electron microscopic, C) Immunostaining (Collagen type I is pink, Collagen type II is blue), images of the Bone Ligament Junction [24], scale bar corresponds to 250μm, D) Masson staining of the Bone ligament junction, NFC is non-mineralised fibrocartilage, MFC is mineralised fibrocartilage.

considered to be the line between the soft and hard tissue and protects the soft tissue from injury during mechanical loading. [26] In histology the enthesis can easily be identified by staining for collagen I and II, as bone and ligament feature collagen I, but lack collagen II. While the fibrocartilage lacks collagen I and heavily features Collagen II. When doing so the collagen fibres can be seen running through the enthesis, giving the impression that these fibres seem to be splitting up. [24]

1.1.1.5 Ligament injury

Due to the ACL's very limited regenerative capabilities and the mechanical placed upon it, an injury to the ACL very often requires Ligament reconstructive surgery. The gold standard is to preform either one or two incision surgery, using an autograft (the patient's tissue) or an allograft to replace the ACL. In both procedures, small incisions are made to allow access to the ACL, remove the damaged ACL, and install the graft as closely to the ACL as possible. [28] In ligament reconstructive surgery either a piece of the patient's own tendon or ligament is taken (options include the hamstring, bone patellar tendon bone), and used to replace the damaged or torn ligament (autograft). Or a piece of tendon from a donor is used, which is called an autograft. Generally using an autograft brings an additional risk of pain and donor side morbidity, and a longer operation as well as a longer rehabilitation tract. However, allografts suffer from shortage of sufficient donor tissue, a longer integration time of the graft, a risk of transferring diseases as well as a risk of immune rejection. [30] [4] This procedure does generally result in a lower quality ACL compared to the ligament before the injury. A systematic review performed in 2016 showed that overall, 50% of patients who underwent ACL reconstructive surgery, had to undergo additional surgery in the knee joint within 5 years. [51] Figure 6 shows two viable alternatives, these first being the usage of suture tapes, such as Internal brace, in order to reinforce a damaged ligament, allowing the limited healing capabilities of the

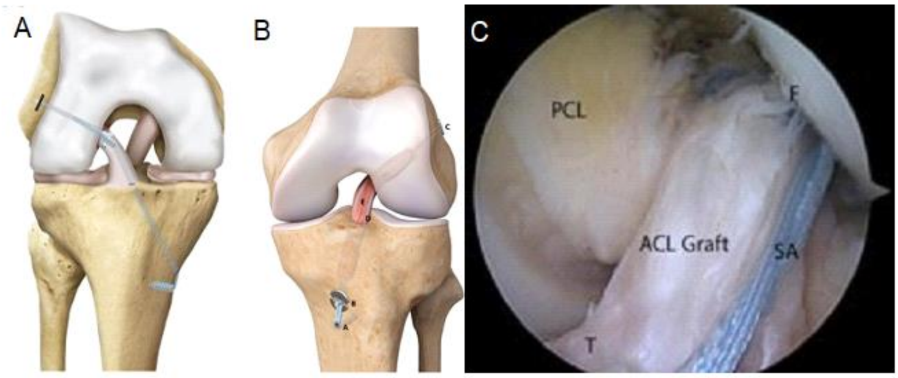

Figure 6: A) Reinforcing the ACL using Anthrax's Internal brace), B) Reinforcing an ACL autograft using internal brace, C) close up into the patient of the reinforced graft, T=tibia PCL=posterior cruciate ligament, F=fibula, SA=suture augmentation [29]

ligament to slowly repair itself, while this technique shows promising short-term results, thus far only a two year follow up study has been performed. [31] Additional research showed that similar suture augmentations could be used alongside a graft, in order to reinforce said graft, and speed up post-surgery rehabilitation. [32]

1.1.2 Tissue engineering (TE) of a ligament

Tissue engineering is a relative new approach in medicine to instead of trying to repair or replace an organ, to guide the body to grow another one. Tissue engineering generally relies on correctly integrating three different factors correctly in order to grow the desired tissue. These three factors are cells, growth factors and a scaffold. The cells are a key component, responsible for the integration and management of the new tissue. The scaffold provides mechanical stability, should be aimed to mimic the new tissues, while also providing a site for cells to migrate and propagate. The last factor are growth factors, these are responsible for chemical signalling between the scaffold, the cells and the host body. Growth factors are responsible for guiding cell differentiation, promoting cell migration, and maturation. [33] It has generally been agreed upon that a proper scaffold is the most crucial factor in Ligament tissue engineering due to the low cell population as well as the mechanical load placed upon the native tissue. [34] While significant advancements have been made in the last decades, the ideal scaffold has proven to be elusive. In a large part this is due to the unique mechanical and biological factors that would be needed for a successful ligament scaffold. The scaffold needs to match the ligaments unique toe region and tensile strength. But at the same time be biocompatible, to not be rejected by the body and to allow cells to immigrate and proliferate. Additionally, the scaffold needs to be porous as well, to allow cells to migrate, and to allow nutrient diffusion. Other requirements, include slow degradability, and morphology.[26]

To meet these requirements, several biological and synthetic materials have been tested. The most popular and researched materials are collagen sponges or hydrogels, due to their excellent biocompatibility, slow degradation rate as well as their reasonable mechanical strength. [38] Studies have shown that pure collagen sheets placed next to the ACL do in fact promote new ligament tissue generation, however this process took 52 weeks in a sheep model and provides little to no mechanical strength in the first weeks after implantation.[8] Another natural material that is widely used is silk, as its mechanical strength matches that of the ACL, and it features a slow degradation rate, as well as good biocompatibility. [39] Besides natural materials several polyhydroxy esters have been used for Ligament Tissue engineering as well, owing to their mechanical strength and that they can be degraded by the body by hydrolysis, examples include which include poly(ε-caprolactone), poly (DL-lactide) (PLA), and poly (DL-lactide-co-glycoside) (PLGA). [37] More recent studies focus on combining synthetic and natural materials, and a variety of composite materials have been produced, producing multifaceted scaffolds which mimics the morphology of a ligament closer. [40]

1.1.2.1 FDA approved TE solution: Biobrace enhances ligament regeneration.

A successful application of combining synthetic and natural polymers is the Biobrace. The Biobrace is a bio-inductive scaffold which is composed of porous type I collagen and poly(L-Lactide) (PLLA) microfilaments, which has been FDA approved for clinical trials this winter. [42] This scaffold is 80% porous and allows for cell migration and new tissue formation. For this implant the PLLA filaments together with the suture tape on both ends provide the strength of the implant, while the collagen sheets provide the biocompatibility and facilitate emigration. Limitations of this implant however is that it requires being placed next to an existing ligament, to adapt its crimped fibre structure, and it is unable to bear the full load normally placed on an ACL. It is still a promising improvement and can certainly help to lower the need of reconstructive surgery for ligaments. However, if the ligament is sufficiently damaged, surgery will still be needed. [43]

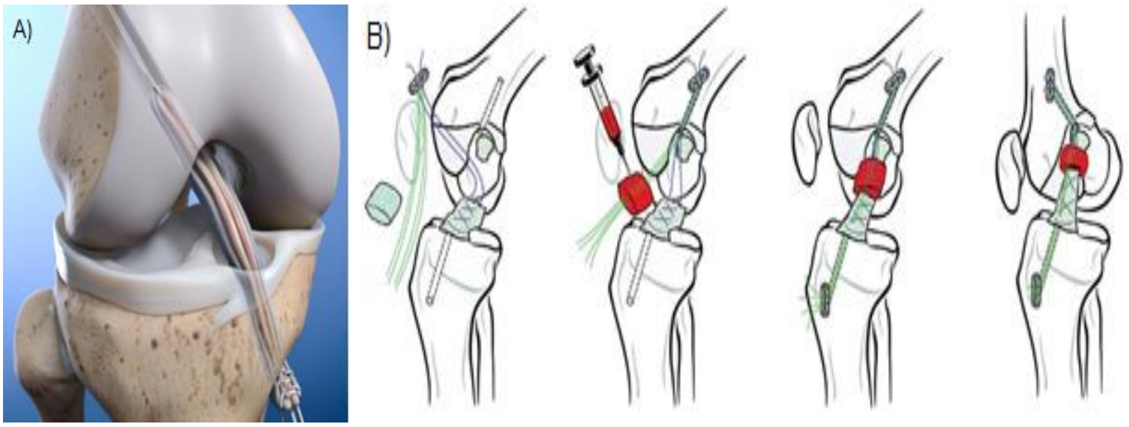

Figure 7:a) The Biobrace, a composite scaffold designed to enhance ligament repair. [41] b) schematic representation of the BEAR procedure. First holes are drilled into the femur and tibia. Next the scaffold is injected with the patients' blood and connected

1.1.2.2 FDA approved TE solution: Bridge enhanced ACL Restoration

Another application of ligament repair, currently in trails on human recipients is Bridge enhanced ACL restoration (BEAR). This procedure utilises bovine ligament tissue, which is decellularized and broken down in a mixture of ECM components, with collagen being the most abundant, being at a minimum concentration of 10mg/ml. This collagen mixture was lyophilised, and a scaffold of 22 by 30 mm was made, which were sterilized and stored at room temperature. [48] When placed in the patient, the produced scaffold is placed between both end of the broken ligament and attached to the femur and tibia trough sutures drilled the respective bones and injected with the patients' blood. The general idea is that a blood clot is formed in the scaffold, which along with the collagen, and the broken end of the ligament connecting to the scaffold, induces a wound repair response. This response leads to the resorption of the scaffold, and forming of new ligament tissue in its place, reconnecting the broken ACL pieces. [49] This procedure has gained FDA approval in 2020, and a recently published study showed BEAR results were like ACL reconstruction surgery. [49] While an additional study showed that 6 months after surgery, BEAR patients were more often cleared to return to sports activity compared to ACL reconstruction patients. However, this difference was not visible 24 months after surgery, with both groups showing similar results. [50] These results are very promising, as it would remove the need for graft surgery in most cases. Yet longer follow up studies are required to monitor the long-term effect. There in one limitation to this solution which is, that if the bone ligament interface is damaged, ACL reconstruction would still be needed.

1.1.2.3 Tissue engineering of the bone ligament Interface

A very important point to note is that both solutions only engineer ligament tissue and use sutures/the remains of the original ligaments to connect the ligament tissue to the bone. This is because tissue engineering a functional Bone Ligament interface, and which properly connect the new tissue to the bone is the bottleneck in tissue engineering. [52] Current clinical solutions bypass this problem by placing sutures or screws in the adjacent bones and connecting the new tissue to the bone in this way. While this design is effective, it is also very painful for the patient. And the mechanical mismatch between the suture and the bone does cause stress shielding as well. [29][30][42][48] Research has showed that when placed in a dual phased scaffold, with a bone and a ligament region, cells can differentiate in fibro chondrocytes and form an interface layer. [54] Limited success has been seen with bio inks. These procedures 3d print a scaffold using a hydrogel containing bioactive molecules or even dissolved ECM. [52] These scaffolds consist of a ligament layer, containing ligament promoting biomolecules, followed by an interface layer, containing both bone and ligament promoting biomolecules, and finally a bone layer, containing bone promoting biomolecules. [53] These scaffolds, when placed in a defect in the interface region, did show an improved regeneration of this defect. However, the newly formed interface regions were significantly less organised than the original tissue. [52][53] A recent study showed very promising results using a biphasic electrospun scaffold, in order to provide directional guidance for the cells. [55] Underscoring the importance of providing directional guidance to the cells when tissue engineering a ligament and its bone interfaces.

1.1.2.4 Material fabrication techniques to provide directional guidance

Ligaments are highly anisotropic tissues, mainly consisting of fibres oriented in the longitudinal direction. To successfully tissue engineer a ligament this degree of anisotropic structure has to be mimicked. To achieve this, it is necessary to provide directional guidance for the cells to produce ECM in the correct direction and mimic the ECM of a ligament more accurately. A heavy focus has been placed on manufacturing techniques, using producing fibrous materials, as these resemble the collagen fibres or fibrils in the ligament. The fibres are most often knitted or braided in specific patterns, which leaves the material with a structure like the ligaments crimp pattern, mimicking the toe region. Examples are both braided silk [35], and PLA microfibres [36]. The downside to these scaffolds is that they mainly focus on matching the ligaments anisotropic mechanical properties, and lack porosity, preventing cells from migrating and forming new tissue. [34] It has been established that a 200-250µm diameter pores are needed for optimal cell migration. [44] However adding those pores to the scaffold, would weaking it significantly, reducing its effectiveness.[1] A successful way to increase the porosity of the collagen-based scaffolds, is freeze-drying. Freeze-dried collagen sheets showed improved porosity and an improved cellular response. [57] While these scaffolds show an improved cellular response and can be shown to form ligament tissue. This process is very slow, due to the low regenerative capacities of the ligament, and freeze-dried collagen sheets by themselves do not provide enough mechanical support to allow for ligament growth.[8] Both of the previous FDA approved solutions bypass this issue by reinforcing the collagen sheets by microscopic polymer fibres. [41][49] Another technique that produces small fibres is electrospinning. Electrospinning can produce micro-or-nanoscale fibres. The process places electric charge on a droplet of viscoelastic solution, creating an electrostatic repulsive force on the surface, countering the surface force and stretching the fibre out. This process allows the production of fibres with far smaller diameters traditionally produced. The downside to this process is that electrospinning provides poor control over the placement of these fibres. [45] These fibres can be used to provide topological guidance for cells and increase the degree of organisation in a scaffold. [46] By combining the principles form electrospinning with 3D-printing additive manufacturing principles, it is possible to create a new method of manufacturing: Melt Electrowriting. Melt Electrowriting allows us to combine the small fibre diameter from electrospinning, with the controlled placement of 3D printing. [47]

1.1.3 Melt Electrowriting (MEW)

Melt Electrowriting (MEW) is an emerging electrodynamic additive manufacturing technique, which combines the principles of 3D printing. MEW can be utilised to produce scaffolds consisting of precise and porous fibres with a diameter ranging from 2-50µm. [56] Additive manufacturing and specifically MEW has recently gained popularity in Tissue engineering, due to their high manufacturing precision, allowing to produce scaffolds which better mimic the tissues ECM. In short, there are three principles behind MEW production. The first is a syringe, filled with a fluid, which possesses a low flow rate, a prime example being a polymer with a low melting temperature and high viscosity, such as PCL. The second principle is a metal needle connected to said syringe. Enough pressure will be placed upon the syringe, to make a droplet of molten PCL trough the needle, but not enough pressure for the PCL to start to flow down to the collector plate. The final principle is to place an electrostatic charge on the needle, and the molten droplet of PCL. This charge results in an electrostatic force, which stretches out the PCL, countering the surface tension. This drawing results in the formation of a small fibre running from the charged needle to a grounded collector plate. This process results in well-defined fibres, opposite to fibres produced by electrospinning, which are difficult to position and layer accurately. [58, 56, 47] Various patterns have currently been printed using mew, mostly consisting of box structures or straight fibres. [47]

Melt Electrowriting is shown to be a promising technique as its porous design has shown to provide better directional guidance to cells compared to electrospun scaffolds, while simultaneously allowing improved porosity and increased manufacturing control. [46]

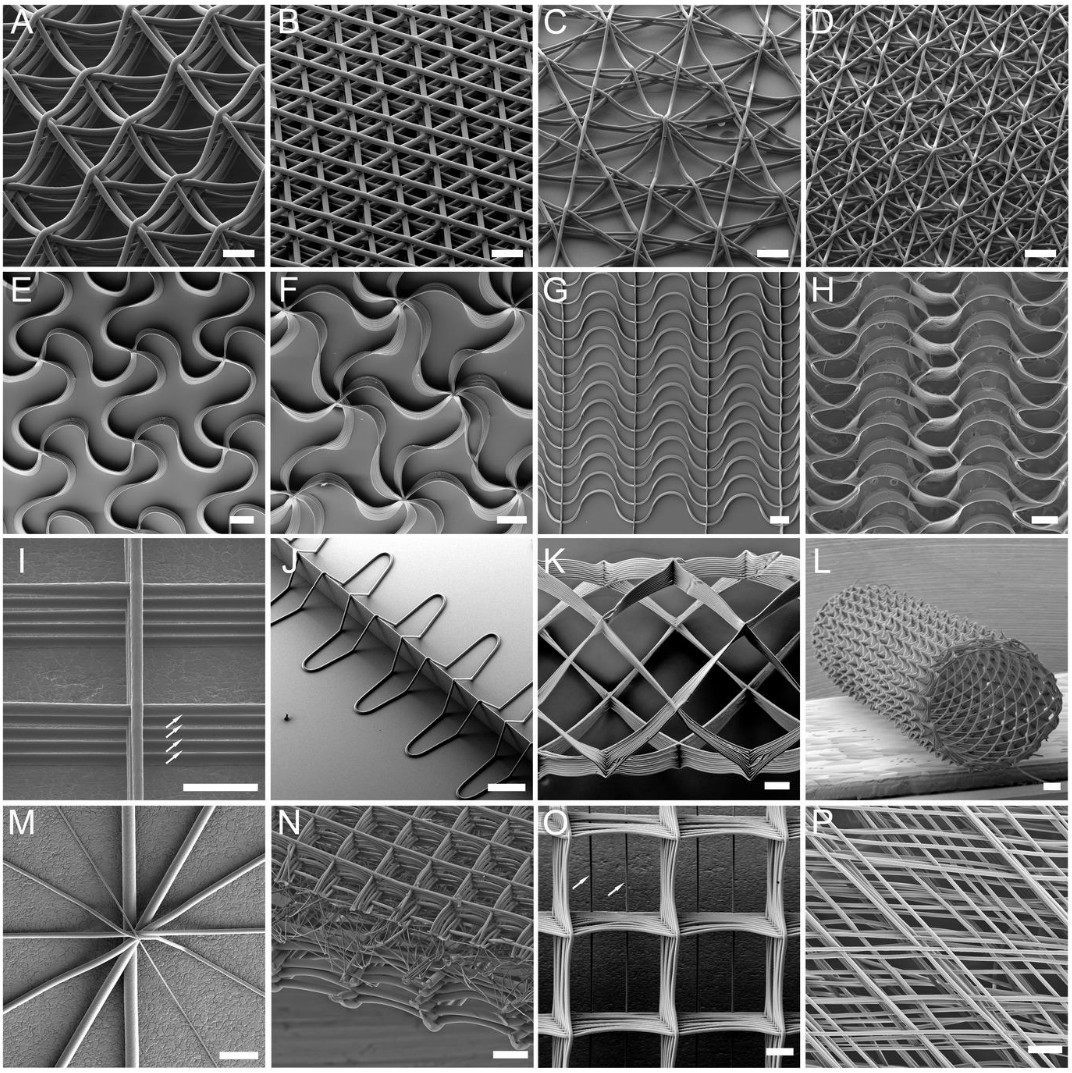

Figure 8: Several Melt electro written designs that have been produced., note the crimped pattern (G), the box plot (O), and the diamond fibres (P)[47]

The previously mentioned PCL is currently the golden standard for MEW. Primarily due to its semicrystalline nature, rapid solidification and low melting temperature of (60°C) and it solidifies rapidly after deposition [59]. Additionally, as PCL is biodegradable, and FDA approved for medical purposes. [37] A challenge to utilise PCL for ligament tissue engineering is the fact that pure PCL is mechanically weaker than a Ligament, and MEW scaffolds, as seen in figure 8 are very porous, significantly decreasing the scaffolds strength. [60][61][21][23]

1.1.3.1 Design considerations for MEW

There are several factors to consider when it comes to designing a mew scaffold. These factors include the distance placed between the printed fibres, the diameter of said fibres, as well as the printing pattern. For the diameter of the fibres, research has shown that when fibres are printed in such a way that a square pattern is formed (figure 8O), from now referred to as a box plot. For a box plot the ideal pore size for optimal cell adherence is 200 µm. [62] In addition, it has been established that a scaffold for ligament tissue engineering should ideally have a pore size of at least 220-250 µm. [34] This research however is based on freeze-dried and braided scaffolds. Because of the more porous nature of a MEW scaffold, this value is likely to be lower, resulting in 200 µm pore size being a good reference point for designing a MEW scaffold.

The fibre diameter is another design factor, the fibre diameter is for the largest part decided by the pressure placed on the syringe and the charge applied to the needle. [47] For ligament tissue engineering, the ideal fibre diameter would match the size of collagen fibrils, to efficiently mimic the ECM. The diameter of collagen fibrils is 1-30µm, with the average being 15 µm. [4] Therefore the ideal fibre diameter for a ligament MEW scaffold would be around 15 µm. One important factor that should be considered is the fact, when a fibre is being printed, it is electrostatically attracted to already printed fibres. This interaction is stronger with a higher fibre diameter, or when more voltage is used (which usually results in a thinner fibre). [63] Because of this, the pore size and fibre diameter are subject to change, in order to ensure printability.

The final consideration is the printed pattern. For ligament tissue engineering, utilising a pattern that induces similar mechanical properties to a ligament is crucial. As PCL fibres do not possess the toe region a ligament has, this mechanical property will have to be induced trough the printing pattern. The most logical option would be to print the fibres in a crimp pattern similar to the print pattern observed in a ligament. There have been several studies who attempted to print a crimp pattern, which showed that the crimp width and length affect the mechanical properties. The smallest crimp printed in literature was 500 µm, with a 60 µm crimp height. [65] While another study produced a crimp pattern with a 2mm wavelength, but the crimp height was 160 µm, a relatively smaller crimp height. [66] These crimp waves are several factors higher than the ligaments crimp length of 26 µm and height of 5 µm. [2]

In general, there are two ways of producing a crimped pattern, one way is to move the printing syringe over the collector plate at a slower pace than critical translation speed

(CTS). CTS is the speed at which the polymer flows from the syringe trough the needle at the exact same speed the syringe moves compared to the collecting plate. When printing below the CTS, the print pattern becomes a sinusoidal wave. This is due to the polymer being extruded faster than it can be deposited, and the electrostatic charge preventing an increase in fibre diameter. [67]

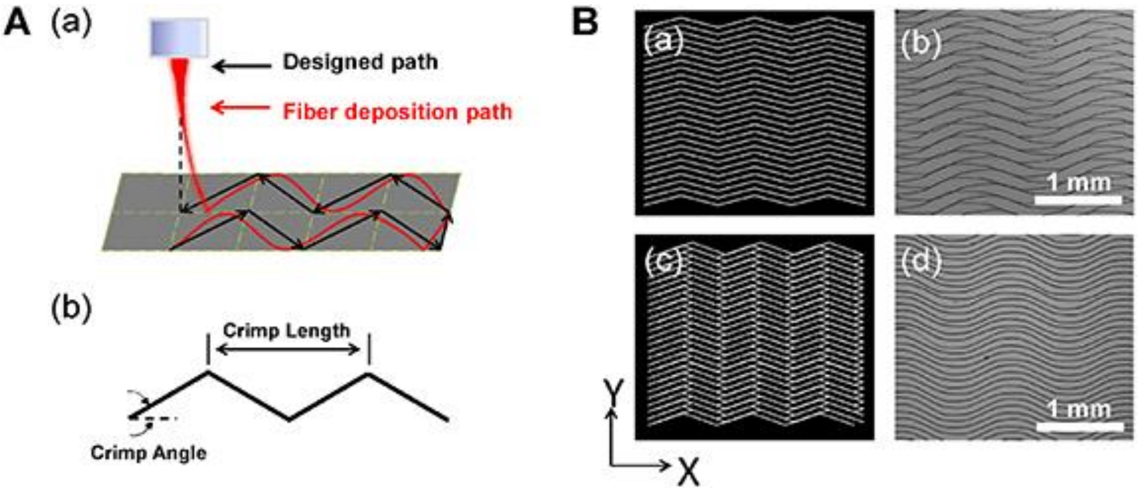

Figure 9: A) The printing path and its theorised trajectory(a), schematic overview of the printing path (b), B resulting printing patterns using the triangular crimp printing method, underlining the importance of optimising the printing pattern. a, c) showcasing two different printed patterns, b, d) showcasing the resulting prints. Scale bars note 1mm. [66]

The second method is to design a printing pattern that results in a crimped pattern. This can be done by either encoding the collector plate to move a circular printing pattern, or by encoding a triangular one. The second method relies on the printing jet lag, this is the phenomenon that the fibre is always being deposited behind the actual location of the needle, due to its relative movement. In this method the collector plate is moved in a triangular pattern and the actual crimp pattern is formed due to the printing jet lag. Figure 9 shows the general idea behind this triangular crimp printing pattern.

A previous study in the Hoey lab focussed on producing crimped fibres and compared said methods. This study showed the triangular method to be the most accurate method, this method still showcased significant printing variability when compared to more traditional straight line scaffold designs. Crimped fibres with a 300µm crimp length and 50 µm crimp height were produced. [68]

Another method, which does not rely on printing jet lag, is to print the scaffold in a diamond pattern. For hearth tissue engineering a hexagonal scaffold was printed with a 45° angle. This pattern has shown a 10% toe region. [69] Diamond scaffolds printed at an 30° angle showed toe regions as well. [65] However, the ligament features a 2-3 percent strain toe region, which requires the diamond pattern to be printed at a smaller angle. Studies have shown that printability decreases if the angles between printed fibres decreases. [56]

In conclusion, PCL scaffolds have been shown to achieve a similar non-linear stress response as ligaments. However, the crimp pattern method has shown to be inaccurate to print, while the diamond pattern currently only has been printed at greater angles, and a greater toe region.

1.2 Aims of thesis

The main aim of this thesis is to develop a biphasic scaffold for bone-ligament tissue engineering using Melt Electrowriting (MEW). This aim is divided into three separate aims, which each contain their own sub aims.

1. *To use MEW to develop a scaffold for ligament tissue engineering.*
    1.1. *To print crimped fibres and produce a crimped fibre scaffold.*
    1.2. *To produce a diamond square scaffold*
    1.3. *To compare both scaffolds mechanically and on printability.*
2. *To develop an FEA model to predict the mechanical response from a MEW scaffold.*
    2.1. *Develop a FEA model of the printed scaffolds.*
    2.2. *Validate the FEA model by comparing it to mechanical testing data from printed scaffolds*
    2.3. *Use the FEA model to finetune the parameters of the MEW printed scaffolds.*
3. *Design and print a biphasic scaffold with a bone and ligament compartment.*
    3.1. *Design a scaffold with a ligament and bone part.*
    3.2. *Use the FEA model to monitor the stress distribution and optimise the design.*
    3.3. *Try to print the biphasic scaffold.*

2 Methods

2.1 Melt Electrowriting.

A custom build melt Electrowriting printer was used, the setup contained a printhead, this contained a syringe filled with medical grade PCL, connected to a 22G metal needle at the bottom. The printing head encased the syringe in a heating system keeping the temperature of the printer head at 80°C and the metal needle at 85°C. These temperatures are far higher than PCL’s melting temperature of 60°C. A higher temperature than the melting temperature is needed to prevent the polymer from resolidifying during the printing process. Raising the temperature does increase both viscosity and the degradation rate of PCL. As PCL degrades when in contact with oxygen, and MEW prints, have a very high surface area compared to bulk mass.[59] A metal ring is placed around the needle, applying voltage. Several voltages have been tried and 6kV was found to be the lowest voltage which produced a fibre that was homogenous in its diameter. The pressure needed for MEW was applied using compressed air, which is regulated trough a PID regulated pressure controller. The pressure used for printing was set at 0.5 Bar for printing. The printhead is shown in more detail in figure 10 and described in more detail by Eichholz et al. [70].

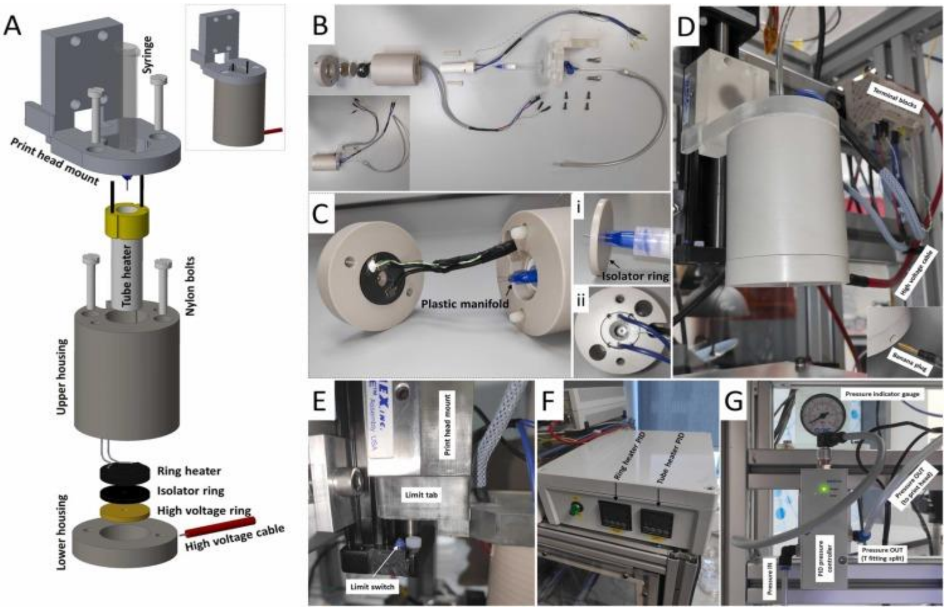

Figure 10: Print head for MEW printer. A) CAD design of X-Y stage and print head assembly. B) Exploded view of print head assembly with detail showing thermocouple attachment to ring heater. C) Assembled upper and lower print head sections showing placement of heater and wiring. D) **Completed print head mounted to linear slide.** E) **Limit tab on print head mount to home slides and accurately define nozzle height while also ensuring the print head cannot collide with the plate.** F) **Temperature control unit with a PID controller for each of the two heaters.** G) **Set-up for accurate PID control of air pressure for material extrusion. [70]**

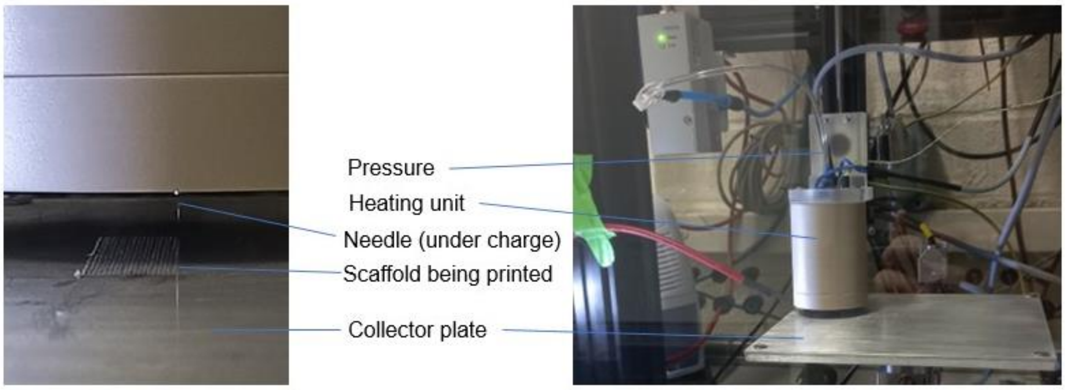

Figure 11: A simplified overview of the custom MEW printer used

The produced fibres were deposited on a grounded aluminium collector plate, which was set to be 5mm away from the print head. Movement of this collector plate was controlled trough two motors units and two sliders, allowing movement in the x and y direction respectively. All the printing parameters, pressure, voltage, temperature and movement of the collector plate are controlled trough a Trio basic Code in motion perfect v4.3 software. This software allows for one central computer unit to be able to control all parameters. This has several advantages, for example it is possible to change the speed of the collector plate mid-print, or it is possible to encode all the components to shut off after the print. Figure 11 shows a more general overview of the MEW printer used.

The final variable is the speed of the print head moving compared to the collector plate, this speed is also called the translation speed (TS). When the other parameters, such as

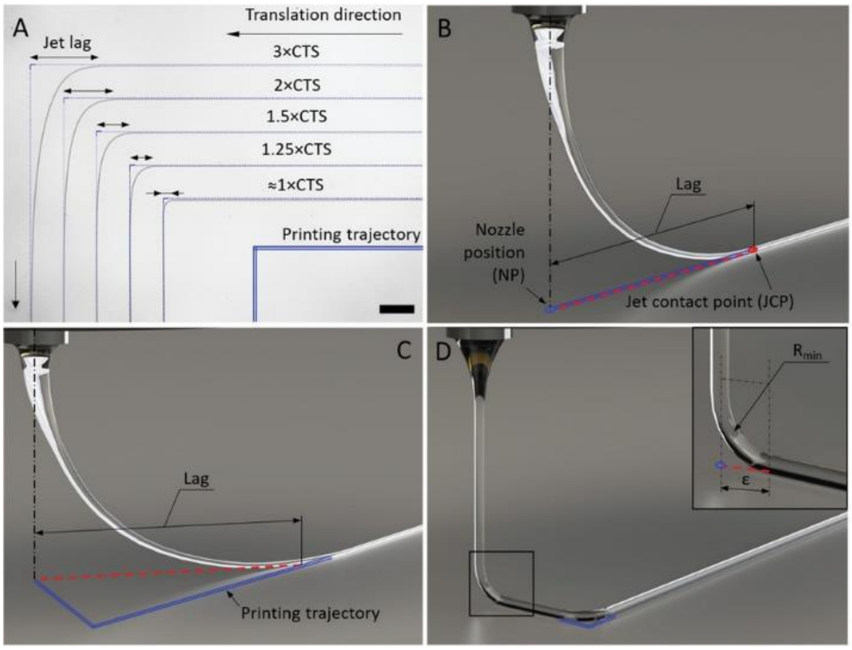

Figure 12: Difference between the print head and collector trajectory at varying collector speed. Scale bar: 1.5 mm. B) Schematic of an MEW jet, printed along a straight line above CTS. C, D) Schematic of a MEW jet near a path turning point while the collector is moving faster than CTS(C) and at the CTS(D) [72].

air temperature, pressure, humidity and voltage remain the same, the TS is largely responsible for the polymer jet that can be seen while MEW printing, this jet is shown in figure 12. The critical translation speed (CTS) is the TS which is equal to the speed of the polymer jet reaching the collector plate. Going below this speed results in the coiling of polymer, which resembles a crimped pattern. While going above the CTS, the deposited fibres generally follow the encoded print pattern, with a delay, or printing jet lag shown in figure 12, which increases if the speed is increased. For printing a fibre in a straight line, an increase in this delay generally means a thinning of the fibre. [71] Because crimp fibre printing relies on using mentioned printing jet lag, a small alteration in this lag, can significantly affect the accuracy of the crimp pattern. Therefore, an increase in the translation speed decreases the print accuracy. As a result of this, for every scaffold, samples were printed at different speeds starting slightly above CTS. Ironically, the opposite is the case for the diamond pattern, because in the diamond pattern the fibres cross each other at a very small angle (10-20°), and the smaller the angle is between two crossing fibres the stronger they are attracted to one another, and the higher the chance that these fibres clump together instead of crossing one another. This problem can be overcome by decreasing the attraction force between the fibres. The two ways to do this are to either lower the voltage on the printing needle, or to decrease the fibre thickness. [72] To do so one of the three factors has to be changed: the voltage, the pressure or the TS. Both the voltage and the pressure cannot be lowered, as the amounts used (6kV, and 0.5 bar respectively) to print the scaffold shown in figure 13 are at the lowest value to reliably MEW print, with the current setup. This is due to Mew printing being a careful balance between all discussed parameters. For example, a lower voltage would result in an uneven fibre diameter due to Plateau–Rayleigh instabilities, while a lower pressure would result in the printing jet requiring more voltage to reach the collector plate. [76] The final option is to increase the TS, which in turn lowers the fibre diameter, resulting in a weaker electrostatic interaction, and a more accurately printed diamond scaffold. The downside of increasing the TS with the goal of altering the fibre diameter, is that it reduces the printing accuracy.

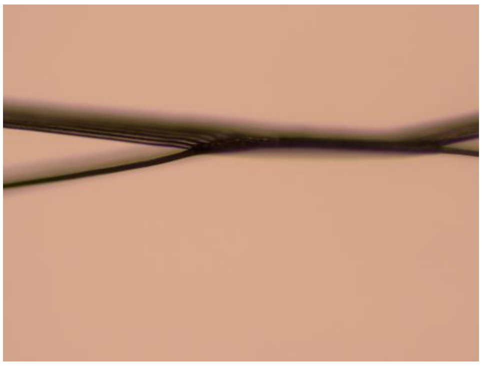

Figure 13: An example of two fibres clumping together due to electrical attraction

2.1.1 Printing designs.

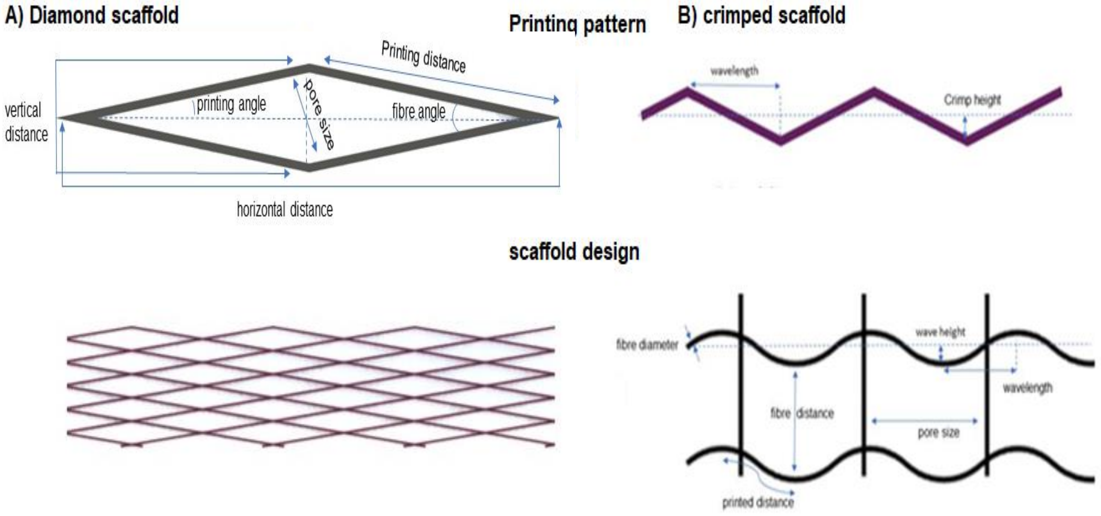

Figure 14: The printing pattern and desired scaffold design for A) the diamond model and B) the crimped wave scaffold.

Two scaffold designs have been made in order to achieve the toe region in the print. The first design features simple diamond structure made using the function MOVE (horizontal distance, vertical distance), shown in figure 14a. While the other scaffold is a crimped waveform design inspired by native collagen. As previous work has shown that the triangular method described earlier is the most accurate to achieve a crimped pattern, this method will be used. [68] Aside from the crimped fibres which provide the toe region when stretched, there will be vertical fibres placed as well. These fibres serve as structural support for the scaffold, the scaffold and its printing pattern are shown in figure 14b. This triangular pattern is achieved using the MOVE function: MOVE (wavelength, crimp height), MOVE (wavelength, -crimp height) To calculate a potential toe region, and to try and characterise the scaffold, several parameters were defined. For the diamond scaffold, those factors are the printing angle, which is the angle of the fibres regarding the tensile load being applied during testing. The fibre angle is the small angle between two fibres who cross one another, and equal to twice the printing angle. The pore size is the shortest possible distance between two parallel placed fibres. The horizontal distance is the distance between two parallel fibres in the direction the tensile load is applied, while the vertical distance is the distance between two fibres in the direction perpendicular to the applied tensile load. The printing distance is the distance between two fibres, following a fibre crossing both. All these parameters are shown in figure 14**.** The maximum possible elongation is calculated using trigonometric formula of cosinus:

$$\cos(\text{printing angle}) = \frac{horizontal\ distance}{2*\, printing\ distance} \rightarrow$$

$$2 * \text{ printing distance} = \frac{horizontal\ distance}{\cos(printing\ angle)}$$

$$\%\ elongation = \frac{\frac{horizontal\ distance}{\cos(printing\ angle)} - horizontal\ distance}{horizontal\ distance} * 100\%$$

$$\%\ elongation = (\frac{1}{\cos(printing\ angle)} - 1) * 100\%$$

For the crimped pattern the formula is a little more difficult, the parameters for the crimped pattern are printing distance: this is the length of the crimped fibre if one crimp pattern is fully elongated. The wavelength is the distance of one crimp pattern in its crimped state in the direction of applied tensile load. The wave height is the amplitude of the crimp in the wave pattern. The crimp height is the amplitude of the triangular printing pattern, used to achieve the crimp wave. These parameters are shown in figure 10b. To calculate the % elongation it is assumed that at the start and end the angle of the crimped fibre is equal to the angle of the triangle used to form the crimped pattern. The formula for an inscribed angle is used to determine the printed distance. [73] For the crimped pattern a scaffold with 10% theoretical elongation is chosen, mimicking the elongation of the natural ligament. And as previous work showed that said theoretical elongation matches the toe region of the natural ligament.

$$\%\ elongation = \frac{printed\ distance - wavelenght}{wavelengt} * 100\%$$

$$printed\ distance = inverse\ angle\ (radian) * r$$

$$inverse\ angle\ (radian) = 2 * \arcsin\left(\frac{wavelength}{2 * R}\right)$$

$$r = \frac{wave\ height}{2} + \frac{wavelength^2}{8 * wave\ height}$$

$$printed\ distance = \arcsin\left(\frac{wavelength}{2 * R}\right) * (wave\ height + \frac{wavelength^2}{4 * wave\ height})$$

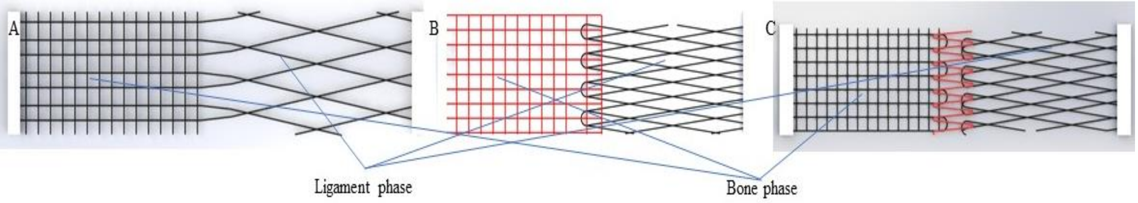

Figure 15: Designs for a biphasic scaffold, a) continuous print design, b) bone (red) scaffold is partially printed over the ligament scaffold (black) c) a suture (red) is printed between the bone and ligament scaffolds (black) to connect the two.

For the bone scaffold a simple square box design was used, as research has shown this to be the ideal model for bone tissue engineering. For a biphasic scaffold three main designs shown in figure 15, were considered. [75]

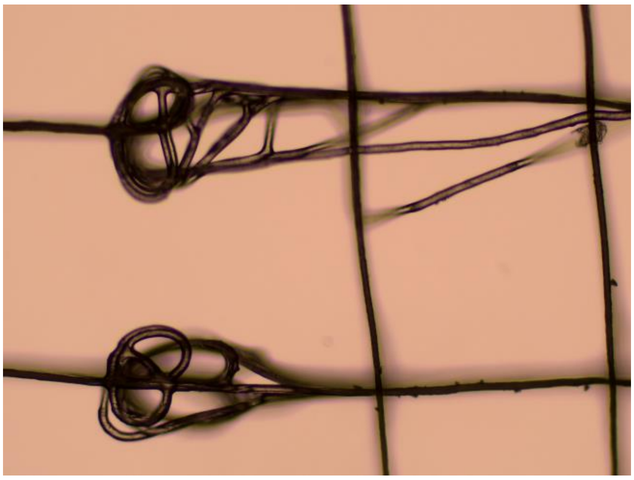

Figure 16: The result of implementing a longer printing pause, resulting in curled fibres as well as a significant decrease in pore size

For the printing of a biphasic bone-ligament scaffold, three designs were considered, these designs, consist of a continuous model (figure 15a), a printed over model (figure 15b), and a suture model (figure 15c). he continuous model the fibres from the bone scaffold continue onto the ligament scaffold, this model allows for the best fibre guidance. The problem is that the previously mentioned increase in TS to achieve the diamond scaffold, this higher TS comes with a reduced printing accuracy, as an increase in the TS means an increase in the printing jet lag. This decrease in accuracy can be detrimental in trying to print continuously from the diamond to straight fibres. This problem can be solved by including a small pause in the movement of the collector plate during printing, this small pause then allows the printing jet to catch up with the collector plate. However, the length of this pause needs to be determined with precision, if the pause is too small the effect will be insufficient, and the print will still be inaccurate. However, if the pause is too long it will result in an accumulation of polymer in one spot, decreasing the accuracy again. Figure 16 shows an example of the printing pause being too big. In order to adjust this problem scaffolds were printed with different pause lengths in order to find the optimal pause length. The other two models, the print over model and the suture model rely on printing the ligament and bone sections separately. In the print over model the ligament and bone sections are partially printed on top of one another in order to connect them. The advantage is a much higher increase in printing accuracy, at the cost of less directional guidance for fibres. The final model the suture model involves printing a third print in between both scaffolds connecting them. The advantage of this is that the suture in between the scaffolds can be designed to function as an intermediate area, however this comes at the cost of a much higher fibre density, and a general decrease in accuracy as three prints are being made next to one another.

All scaffolds are printed first with a higher pore size, to see if printing inaccuracies arise from the printing design, rather than from fibres being placed too close to another and interacting. The crimped scaffold was printed with a pore size of 500 µm first, to achieve the correct parameters for the crimp pattern. The pore size was later decreased to 350 µm, as these are the smallest parameters currently attainable. [68] The designs will first be printed at different speeds above CTS in order to find the optimal printing speed, or TS for this design. Once this speed is found, smaller pore size and crimp length will be attempted to be printed. The crimp height will be chosen to achieve a 10% possible elongation, similar to natural ACL [4]. For the diamond scaffold, designs are printed with a pore size of 500 µm first, which was then lowered to 200 µm in 100 µm increments, or until print accuracy decreased due to fibres interacting. The printing angle was obtained by developing a FEA method detailed below. The printing angle resulting in a toe region of 3% strain, again mimicking the ligament [13] was chosen to be printed. To obtain the diameter of a MEW printed fibre at any given set of parameters, a single layer of straight fibres was printed onto a glass sheet, which was used to determine the fibre diameter. MEW scaffolds were imaged using brightfield microscope in 100x magnification, while the dimensions and accuracy of the scaffolds was accessed using ImageJ software.

Making syringes for MEW printing.

This methods section mentioned PCL filled syringes being used in the MEW process, these are fabricated in the following process. A syringe with a volume of 1ml was partly filled with PCL resin (Purasorb 12, Corbion). The PCL resin was lightly tamped to remove air. Then the PCL filled syringe was heated to 80°C for 10 minutes to let the PCL melt. Next the syringe was centrifuged at 1950g for 5 minutes to remove any air bubbles and heated to 80 °C for 10 minutes again to remove stresses placed upon the syringe during centrifugation. This centrifugation and heating cycle was repeated 3 times. Syringes were stored at – 20 °C until used.

2.2 Finite elements (FEA) analysis of MEW scaffolds using Ansys.

A great deal of time could be saved finetuning the MEW scaffold if it were possible to use finite elements methods in order to correlate a toe region with a theoretical elongation. Especially for the diamond pattern, it is very unlikely for the diamond angles to fully elongate to a straight-line pattern, without a considerable force needed to be applied. Secondly, for the manufacturing of biphasic scaffolds, FEA analysis could give a clear overview of how the scaffold will react to this change in patterns, whether it leads to a build-up of strain or a more gradual interface. Another consideration is that mew scaffolds, are very delicate samples to mechanically test. Making mechanical testing difficult, especially when finetuning small details.

For these reasons a FEA model is developed to predict the mechanical response of a mew printed scaffold using ANSYS 2021 R2 explicit dynamics software. For the modelling of the mew scaffold 1000 times enlarged solid works model is made of one single layer print of the desired scaffold. Modelled scaffolds were either 1000mm by 700 mm, 2250 mm by 750mm or 3000 mm by 750mm. First modelled scaffolds were 1000 by 700mm as 700mm as 700mm is the smallest width that would allow for three different crimped fibres, or three full diamonds being placed after one another in the direction perpendicular to the applied displacement. The second reason was that for mechanical testing of actual printed scaffolds, the width of the samples was limited to 7mm due to the size of tensile grips available. The length was chosen to reduce the size of the scaffold to reduce computation time needed for the model. Longer scaffold models were produced to investigate if the length to width ratio of the scaffold had any effect on the mechanical properties of the scaffold. Fibre diameter was set at 20 µm, or 20 mm in this model.

On both sides of the scaffold, a rectangular block is placed, and set to merge with the fibres of the scaffold. This block will represent the mechanical clamps normally used in a tensile test. This step is necessary to achieve an equal force distribution between the fibres, and to reduce the computational time by simplifying the model. This block must be made in the same model, so that it is seen as one object and Ansys will treat the scaffold fibres as if they are embedded in the block. This solution has been used as adding friction between the fibres and the block overcomplicates the model, increasing the computational time significantly, and has led to the fibres slipping away. PCL was programmed to be a linear elastic material with a Youngs modulus of 343MPa, and a Poisson’s factor of 0.42,

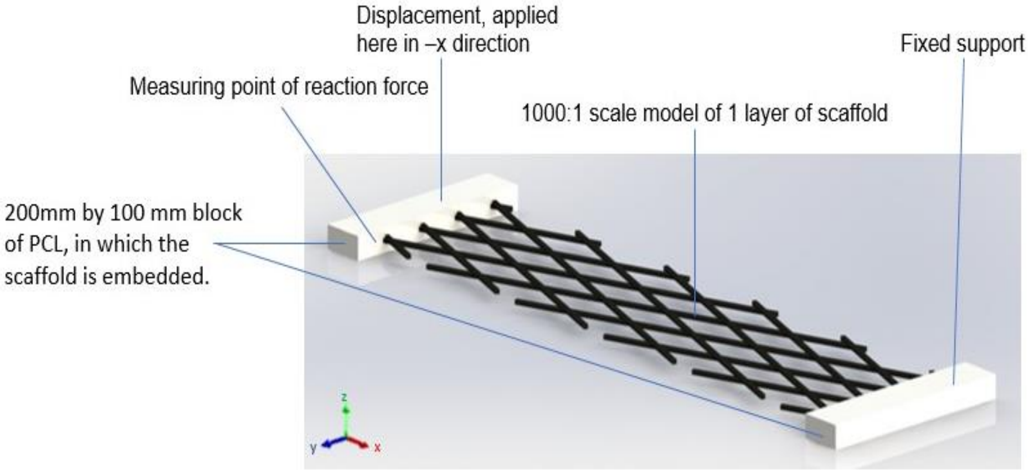

Figure 17: A systematic overview of the Ansys model to predict the toe region.

after literature values for bulk PCL. [60] [61] Maximum internal stress was set at 12 MPa, as necking occurs at this value, and the toe region has to fully occur in the elastic deformation region. [80]

In the model, on one bar at the end, an encoded rigid displacement would be placed, which would equal up to 20% strain of the scaffold. Because natural ligaments undergo critical value between 6 and 10% strain, simulating a scaffold more than twice beyond the failure strain would not give relevant results. A rigid displacement means that the displacement is equal along the entire geometry the displacement is placed, e.g., the bar itself is programmed to not bend. Additionally, movement and rotation of said bar (but not the scaffold itself) is limited to only the direction of the displacement, henceforth called x direction. Finally, the mesh size of the model is set to half the size diameter of the fibres (10mm).

Figure 17 shows the current model, on the opposite side of the displacement, a fixed support is placed, to limit the displacement to only the fibres. From this simulation a rection force probe is placed on the same bar the displacement is placed upon, to measure the force needed for the mentioned displacement. Additionally, the internal stress, strain and displacement are collected from every mesh point, with the maximal value, average and minimal value overall being recorded. These values are plotted against the strain of the scaffold in percentage (to adjust for the scale) and compared with the results of mechanical testing form printed scaffolds. The reaction force will be divided by 1,000,000 in order to adjust for the scale, as enlarging a model 1000-fold results in a 1,000,000-fold larger cross-section. To find the toe region for diamond scaffold design the MEW scaffolds shown in table 2 are simulated.

Printing angle (°)	Horizontal distance (mm)	Vertical distance (mm)	Pore size (mm)	Calculated elongation (%)	Surface area (mm^2)
5	2295	201	200	0.38	$1.15 * 10^5$
7	1641	202	200	0.75	$8.4 * 10^4$
10	1152	203	200	1.5	$5.8 * 10^4$
15	773	207	200	3.5	$4.0 * 10^4$
20	584	213	200	6.4	$3.1 * 10^4$
30	400	231	200	15	$2.3 * 10^4$

Table 2: Differences in parameters when the printing angle is adjusted, while keeping the pore size unchanged.

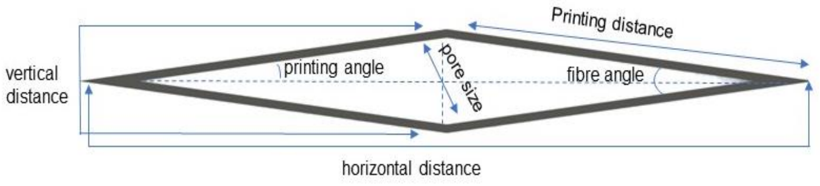

Figure 18: An overview of the parameters for the diamond scaffold

For the biphasic bone ligament scaffold, the main goal of the simulation is the ascertain whether or not there is a build-up of stress at the intersection between the two parts. The second goal is to see when the scaffold is stretched out, whether or not one of the two part stretches out more than the other. To do so, two additional displacement probes are placed onto the models These displacement probes, which are visible as probe 1 and probe 2 in figure 19, are placed with an 800mm (800µm on the scaffold) distance between one another on either side of the interface between the ligament and bone model. These displacement probes are used to determine the distribution of strain between the different parts of the scaffold, when the entire scaffold is stretched out for an encoded amount.

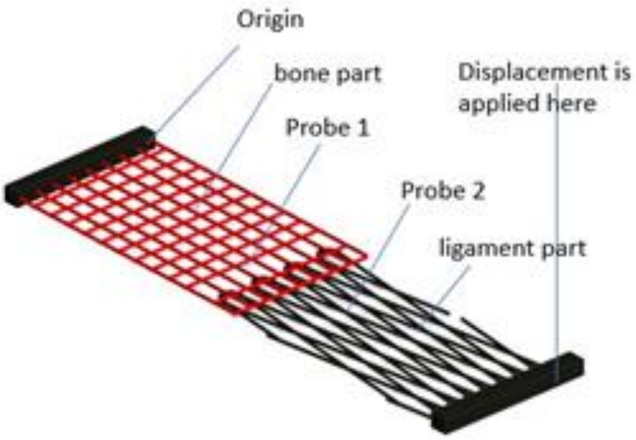

Figure 19: A schematic overview of a biphasic scaffold being analysed.

2.3 Mechanical testing of the MEW scaffolds

The printed MEW scaffolds samples with 10mm length and 7 mm width or 28mm length and 7 or 4 mm with, and 200µm height were clamped in a pair of metal tensile grips using 2000 grip sandpaper to prevent sliding of the samples, shown in figure 20. The tensile clamps were attached to a 5N Twin column load cell and a Zwick Roell Z005 mechanical testing machine. After referencing the crosshead position and the grip-to-grip separation, the scaffolds were tested using a uniaxial tensile testing method. The tests were performed at 1% strain/minute, as to mimic the loading speed of normal walking, while the tests were set to continue until 20% strain. [16] The tests were stopped after 20% strain since the failure strain of a ligament is 10% strain, and mechanical behaviour past twice the failure strain of a ligament is not relevant, as the scaffold should not reach said strain when implanted. [7]

From the resulting tests the stress (σ) was calculated by dividing the force value by the cross-sectional area of the MEW scaffolds. The cross-section area of the MEW scaffolds was obtained by multiplying the number of layers printed by fibres printed (scaffold width/pore size) and multiplying the result with the fibre diameter squared.

Stress strain curves were plotted from where the main properties were characterised. These properties include the toe-region as the x-axis intercept point of the linear region of the stress strain curve. The Youngs modulus was calculated for said linear region, as well as the Ultimate stress (the highest stress seen in the curve), the tensile stress was

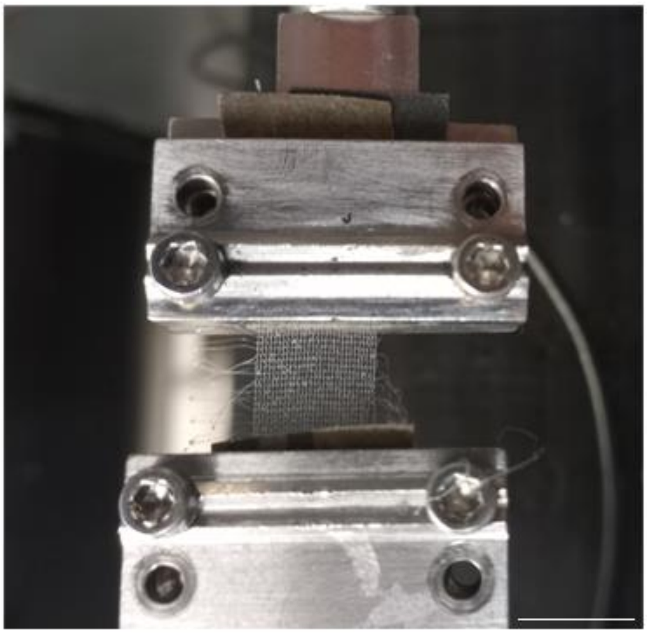

Figure 20: Mechanical testing setup for a crimped mew scaffold, scale bar denotes 7mm

obtained by when the directional coefficient of stress strain curve decreases by more than 2% of its value.. The data analysis was mainly GraphPad Prism 9 (GraphPad Software), and Microsoft Excel. To look for statistical significance One-way ANOVA followed by Tukey tests were performed.

2.3.1 Adjustments to the mechanical testing procedure.

Several adjustments have been tried to improve the mechanical testing procedure. The main problem with mechanical testing is that the MEW scaffolds are very delicate, only requiring 1-2N in force to break, and even the tiniest amount of force can already disrupt the toe region. Because of this adjustments have been tried to improve the mechanical testing. Due to the general 2D structure of a MEW printed scaffold, when this scaffold would be applied for ligament tissue engineering, it would likely be rolled up, to better match the dimensions of the ACL. Therefore, an interest is in mechanical testing of MEW scaffolds when rolled up. However due to their delicacy and small size, rolling up a MEW scaffold is difficult. A protocol was developed to roll up the scaffold, shown in figure 21. The first step was to carefully connect the mew scaffold to a piece of cigarette paper on both sides. This step with cigarette paper was necessary as an in between medium to prevent the scaffold from being damaged by the rolling process.

The second step involved rolling the cigarette paper around a small pin, rolling up the scaffold as well. The cigarette paper was then placed in a small 3d printed O ring, in order to keep the scaffold rolled up, while being placed in the tensile grips.

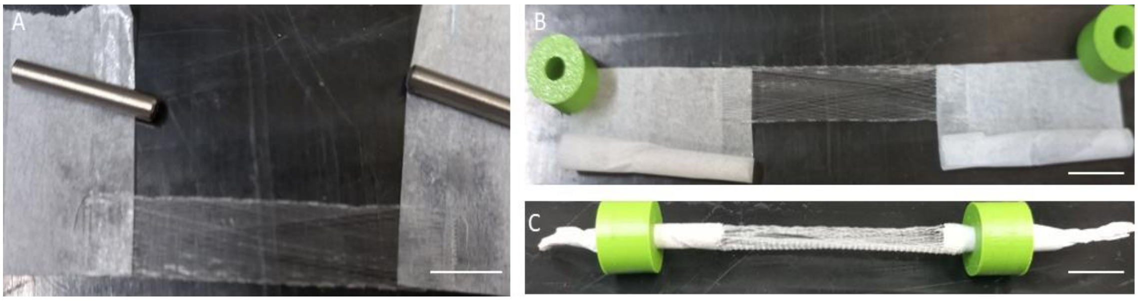

Figure 21: The process of rolling op a scaffold using cigarette paper, two metal pins (diameter 2.9 mm) and two 3D printed O-rings, having a 3.1 mm diameter. First the scaffold is placed on and attached to a piece of cigarette paper on each side (a), then the cigarette paper is rolled up around the pins (b), when the cigarette paper is fully rolled up, rolling up the MEW scaffolds as well. It is crucial that both sides are rolled up simultaneously to prevent the scaffold from being twisted. Finally, the rolled-up scaffold/cigarette paper is placed between the two O-rings (c). This step is to keep the scaffold rolled up when it is placed in the tensile clamps, and to allow the metal pins to be removed. All scale bars note 10 mm.

3 Results

3.1 Model development

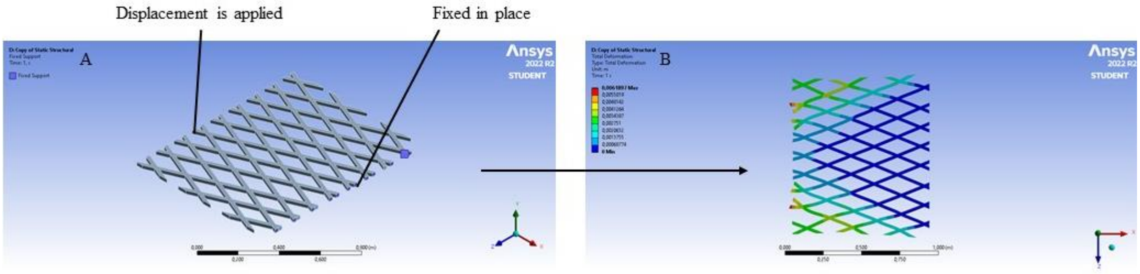

Figure 22: Displacement map of a diamond model without the bars being placed on either side. A) before simulation, B) after simulation. A wide model is shown to show the distribution of displacement in the direction perpendicular to the direction of applied displacement. All scale bars denote 1000 mm.

The first runs of the FEA model for a 1000:1 enlargement of a single layer of MEW, had a significant amount of finetuning that needed to be done. The first issues were related to the fact that Ansys is designed to model massive, non-porous constructs, and was not made to analyse a fibrous, heavily porous model. As a result, the mesh size had to be set extremely small (10mm, or half the fibre diameter). This resulted in an incredible amount of mesh points needed for calculations (A 1000 by 750 mm model already features over 10.000 mesh points.). Which resulted in long computational times, ranging from 10 hours to over 120 hours for the biphasic scaffolds. An additional problem was that when the scaffolds were modelled by themselves (as in the 'Bars' present at both ends as shown in the methods, is not present.) showed the fibres would only bend at the edge of the model and the displacement would not be distributed properly over the scaffold. This is due to

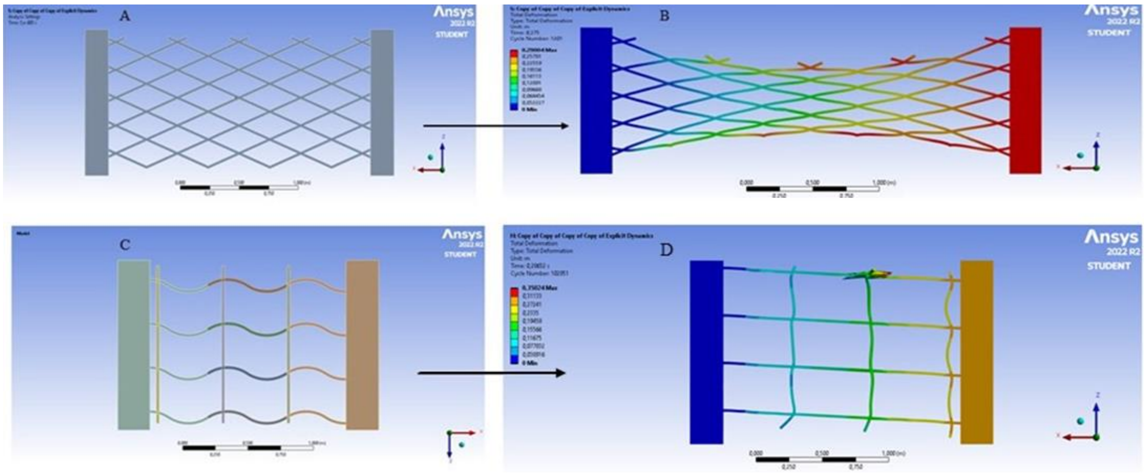

Figure 23: The Distribution of displacement for the diamond and the wave model, left side was fixed in place, right site was displaced for 20% of original length. A) Diamond 30° model before simulation. B) Diamond 30° model after simulation. C) Crimped model before simulation. D) crimped model after simulation. All scale bars denote 1000 mm.

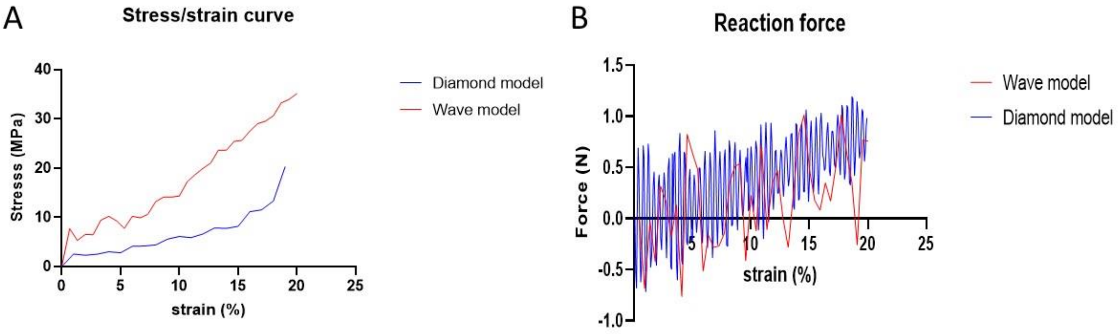

Figure 24: Stress strain, and Reaction force/strain curves of the models shown in figure 22. The high degree of oscillation making it impossible to determine a toe region of the scaffold.

Ansys trying to calculate the displacement in every single fibre, instead of trying to simulate the entire construction being torn apart. To remedy this the two bars shown in the methods were added and the test parameters, (one being fixed in place, on the other a slow displacement being placed) were encoded to be placed on said bars. This methods mimics an actual mechanical test more, simulating the tensile clamps the scaffold would be placed in between. Figure 22 shows the model without the bars, while figure 23 show the model with both bars being placed. This improved model showed promising results. The total displacement showed that the scaffold was stretched out uniformly, as shown in figure 23. However, there was one major drawback, due to no friction being encoded, the scaffolds oscillate heavily when being drawn out. Resulting in a heavily oscillated and generally unreadable internal stress/strain and reaction force/strain curves, these curves are shown in figure 24. These oscillations, also called force vibrations, cause both internal stress/strain and Force reaction/strain curves that are not sufficiently usable.

To try to limit the remedy this high degree of oscillation, it was tried to increase the number of computational cycles of the model, in order to decrease the speed at which the displacement was applied and decrease the oscillation of stress/strain curves.

How this process works, is due to the general mechanism by which Ansys derives the shown curves. Every cycle Ansys calculates how the model deforms when x amount of displacement is applied, then notes down the data, and calculates the effect of another x amount of displacement on the model, etc. This process stops when one of the elimination terms is reached. These terms are either a maximum value set is reached, for example the maximum value of the internal stress (set at 12MPa in these simulations, see methods), or until the maximum encoded displacement is reached (200mm in these simulations, as deformation is applied until 20% strain is reached, length of the model used is 1000mm). For example, in the case of 2 cycles/strain, every cycle Ansys calculates how the scaffold

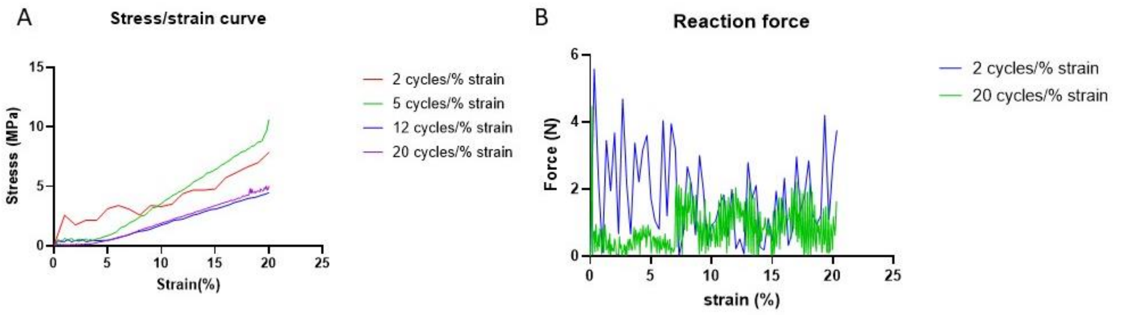

Figure 25: Stress/strain (a), and Reaction force/strain (b) curves of the Ansys model with different speed of applied deformation. Ansys works in cycles for which it calculates the internal stress/, the force, how the model deforms in every cycle. 2 cycles/% strain means that two of each cycles are performed for every percent strain applied to the entire model.

deforms when the amount of deformation that results in 0.5% strain is applied, saves the data, and starts the next cycle, etc. The results of this optimalisation attempt can be seen in figure 25.

This optimalisation shows that while the oscillations in the Reaction force do decrease, when increasing the amount of work cycles, the reaction force/strain curve is still far too oscillated in order to be used, requiring an additional improvement to become usable. However, the internal stress is a different story. As shown in figure 25, the oscillations seen in the internal stress/strain curve does decrease significantly if the number of computational cycles in Ansys is increased. For this reason, the first simulations comparing different printing angles were done using the internal stress as the main output

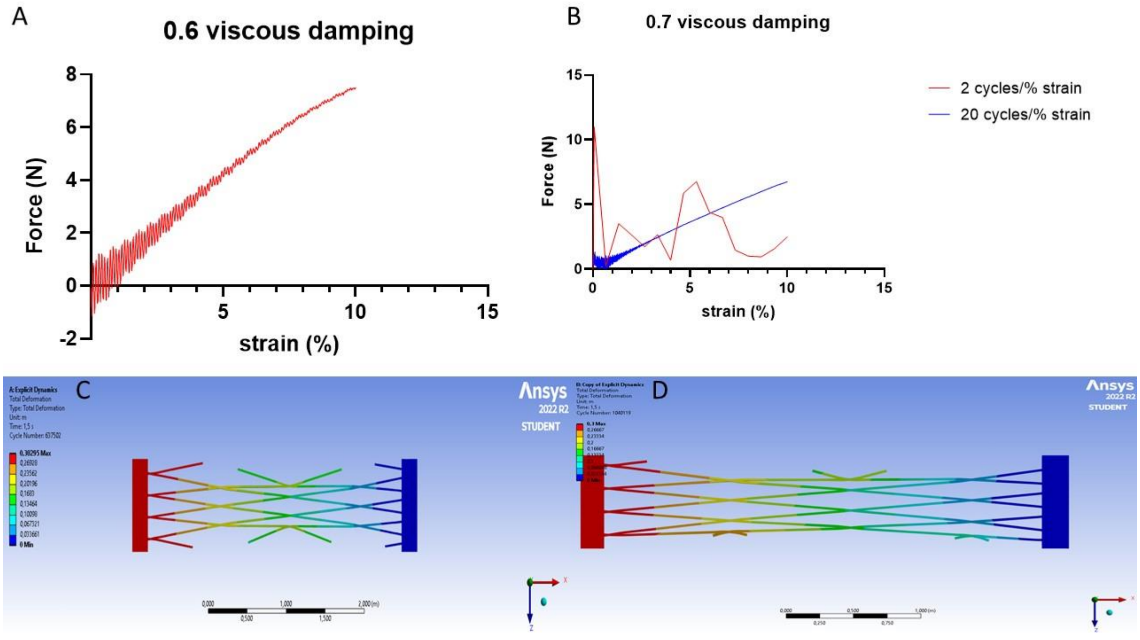

Figure 26: Force reaction/strain curve for a viscous coefficient of 0.6 (a) and 0.7 (b), a 0.7 viscous damping model was also modelled at 2 cycles/% strain opposite to the 20 cycles/% previously discussed, to showcase that both the low displacement/calculation cycle and the viscous damping is necessary. The displacement map of the 0.6 (c) and 0.7 (d) models show that the displacement is still equally dispersed over the scaffold.

variable to find the toe region. The main reasoning behind this was time, at a similar time as this process the printing of the wave model was finetuned sufficiently, and a diamond model needed to be chosen for comparison between both models. Especially since it needed to be confirmed whether or not the diamond model could even be printed at a small angle. This being said, in order to improve the reaction force curve of the model, an additional alteration to the model needed to be made. This last adjustment is the introduction of viscous damping to the model. There are two types of damping in Ansys, viscous (Rayleigh) and static (Coulomb) damping. Viscous damping was chosen as unlike static damping, it is related to the velocity of the movement. Meaning that the viscous damping will reduce the speed of oscillations significantly but affect the slow movement of fibres caused by the displacement being applied much less, as the oscillations occur at a higher speed compared to movement of fibres itself. [81] Multiple simulations using different viscous damping coefficients found that a coefficient of 0.7 (70%) was found to reduce the oscillations to the point that the Reaction force can be read, yet the displacement is still dispersed equally over the scaffold. Figure 26 show the Force/strain curves when a viscous damping coefficient of 0.6 and 0.7 are used, together with the model's displacement map, showing the displacement is still being distributed equally. This success with damping begs the question if the previously mentioned increase in calculation cycles was necessary. To answer this question, the model with 0.7 viscous damping coefficient was modelled at both 20 calculation cycles/% strain, and at 2 calculation cycles/% strain. The resulting graph in figure 26B shows clearly that this is not the case, when the model is computed with 2 cycles/% strain, then the oscillations are too severe for the damping to handle. Alongside aforementioned changes applied to all mentioned scaffolds, there are two additional adjustments made to specifically the diamond scaffold. The first of these changes has to do with how the diagonal fibres in the diamond model cross one another. Originally the diamond model was modelled fully 2-dimensional, having both fibres fully merge when they intersect. This solution led to a high build-up of stress at the intersection between fibres, as shown in figure 27C, and is not a realistic model as well, seeing that the fibres are placed on top of one another and melt together. To resolve this problem, a model was developed with the fibre's half

Intersecting model

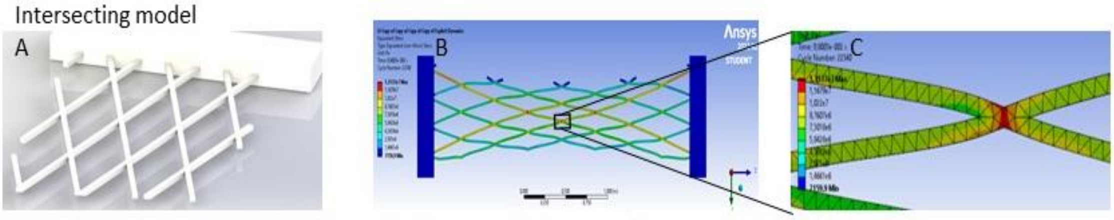

Half intersecting model, which allows for far more displacement

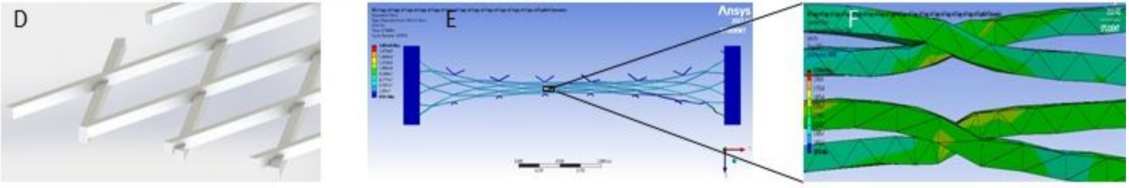

Figure 27: The original full intersecting model a) render of the cross-section, scale bar notes 200µm b) stress distribution of a 20 degrees model, scale bar notes 1000µm c) magnification of one fibre cross section from b, scale bar notes 50 µm. And the new half-intersecting model d) render of the cross-section, scale bar notes 200µm, e) stress distribution of a 20 degrees model, scale bar notes 1000µm f) magnification of one fibre cross section from e, scale bar notes 50 µm.

intersecting. This model is shown in figure 27 d-f and was found to distribute the stress much more evenly along its fibres and allow for a single diamond to elongate more.

The final adjustment for the diamond model is adjusting the size of the diamond model. The first models showed the point of failure being the fibres in the corner of the scaffold. This is caused by the fact that when the diamond model is stretched out in the one direction (x-direction from now on), then it the model shrinks in the direction perpendicular (y-direction) to the applied displacement. However, because the fibres are embedded in the blocks on both sides, preventing the shrink in y-direction, and resulting in stress shown by the sites. Because the size influences the behaviour of the diamond model, diamond models will be computed as a 3000 mm by 750 mm model. The first

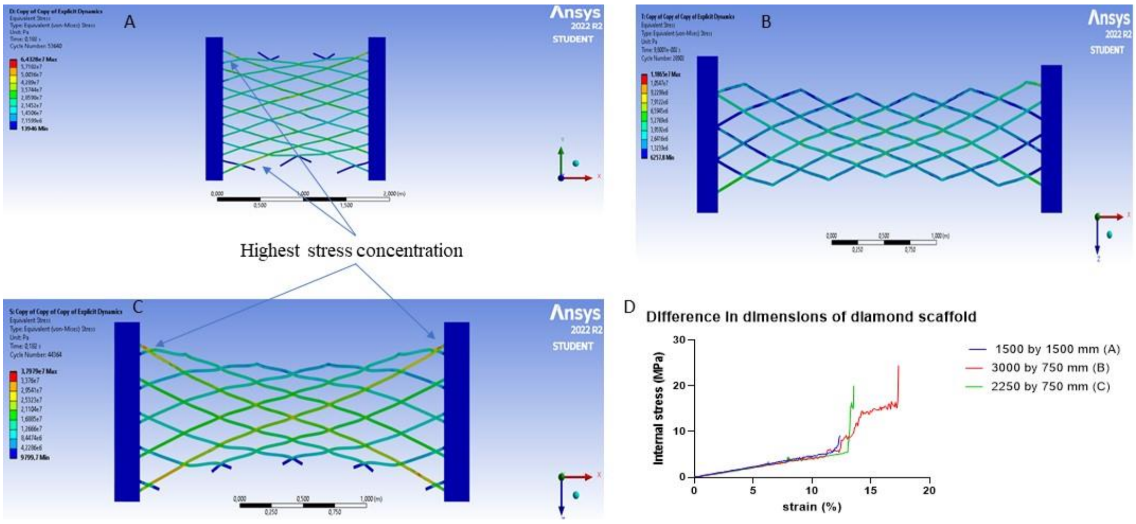

Figure 28: 20 degrees diamond model simulated with the size of the scaffold being the only difference. Model A is 1500 by 1500, scale bar denotes 2000 mm, model B is 3000 by 750 mm, scale bar notes 1000mm, model C is 2250 by 750 mm, scale bar notes 1000 mm. D) stress strain curve of model A, B, and C, showcasing that model A has a shorter toe region compared to model B and C.

reasoning is that the average length of a ligament is 30 mm [3], and a synthetic graft for a ligament is 7-9 mm in width. [82] By choosing values with a similar ratio between the length and the width (4:1), the prediction of mechanical properties will be more accurate. Another consideration is that with the current setup, only scaffolds that are 7mm in width can fit in the mechanical clamps and be tested.

3.2 FEA results

To find the optimal toe region for the diamond model, several diamond scaffold designs with printing angles of 5°, 7°, 10°, 15°, 20° and 30° printing angle were modelled for both maximum internal stress as well as the force reaction. The main reason the maximum internal stress was modelled was due to time constraints, as a printing angle was needed to be chosen for the diamond model to be developed. Because the adjustments needed to achieve a readable force reaction curve needed more time than planned, it was decided to rely upon the current available results to decide on an angle, to be tested alongside the wave model. This decision was further influenced by the fact that literature works stated that a printing angle as large as 30° could lead to a decreased accuracy; making it questionable whether or not the printing angle of the final diamond model would be decided based on the FEA model or on printability. Alongside the diamond models, the chosen wave model, with 10% elongation was modelled as well, to evaluate the accuracy of the FEA model for multiple scaffold designs. Figure 29 shows the resulting Maximum internal stress/strain curve. Resulting graphs showcase that the diamond models have toe regions ranging from 4% till 30% elongation, depending on the printing angle. Similarly, the 10% elongation wave model shows a toe region of 4% and matches the expected

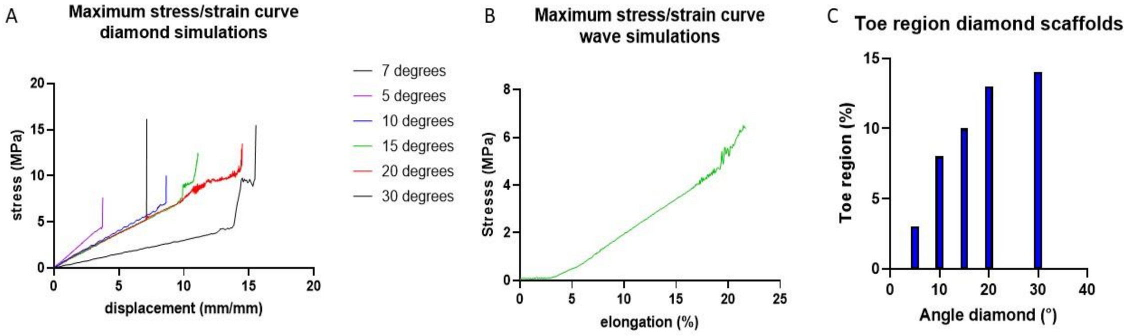

Figure 29: Results of FEA simulations using maximum internal stress. a) Maximum internal stress/strain curve for plotted diamond models. b) Maximum internal stress/strain curve for the chosen wave model c) Toe region was established by the sudden peak in the internal stress for the diamond model.

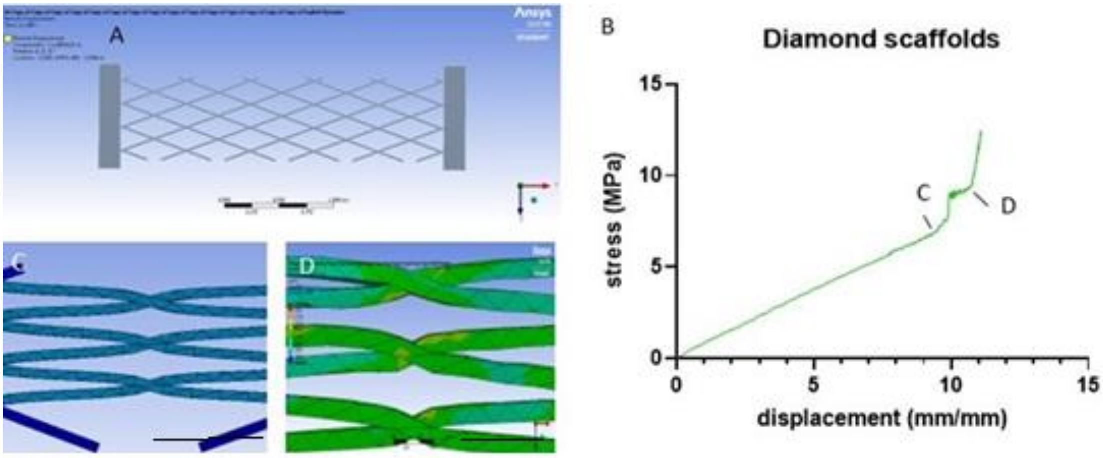

Figure 30: Change in scaffold at the point of the internal stress peak. a) the modelled 15° printing angle scaffold scale bar notes 1000mm, b) stress strain curve of modelled 15° printing angle scaffold, c) close up of scaffold just before said stress peak, denoted by C on figure b, scale bar notes 500mm, d) close up of scaffold after said stress peak, noted by D on figure b, scale bar notes 500mm.

stress/strain curve for the wave model. The diamond model however does not match the expected stress stain curve. To determine the toe region the sudden peaks in internal stress, visible in figure 29a were chosen, these peaks and image of the FEA model at said peak are showed in figure 30, showing that the elongate until said stress peak. Based on the results shown in figure 29, a 5° printing angle was chosen for the diamond model to be printed. As the diamond models did not show the expected stress strain curve, adjustments discussed previously were made to improve the reaction force model.

Figure 31 shows the simulated reaction force for all scaffolds modelled in figure 29. The reaction force obtained trough said Ansys models were still oscillated. It was possible, using a moving average of 10 data points, to achieve a readable force/strain curve. Wave model showed the exact same toe region of 4%, and the force reaction curve had a similar

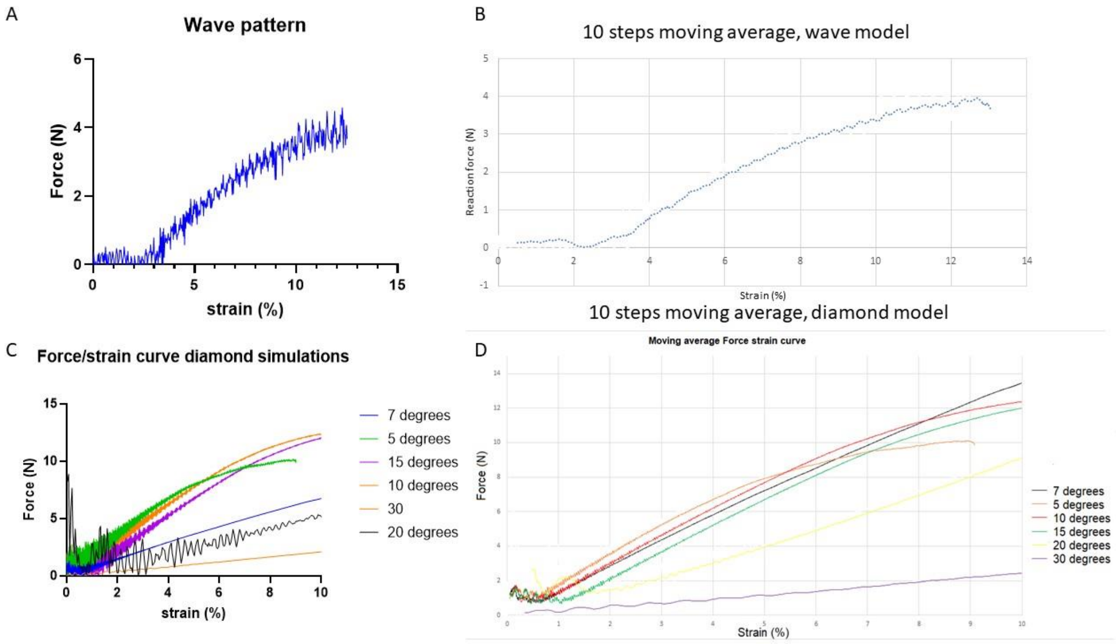

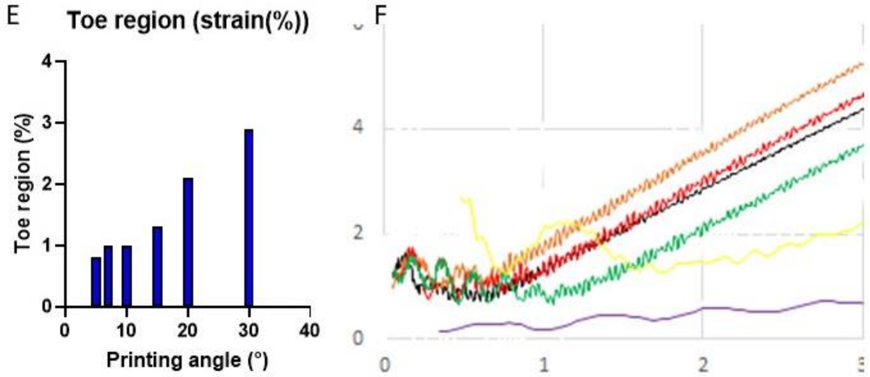

Figure 31: Results of FEA simulations using Reaction force. a) Force/strain curve plotted for wave models, b) Moving average (10 points) of force/strain curve of wave models to improve readability c) Force/strain curve plotted for diamond models, d) Moving average (10 points) of force/strain curve of diamond models to improve readability, e) Toe region of diamond force/strain curve, displaying more realistic values. f) Enlargement of toe region area of force/strain curve d.

shape. For the diamond model, the force/strain curve had a drastically different shape, closer to the expected shape and the shape of the force/strain curve of the wave. Toe regions were obtained by determining the intersect point from the linear region from the force strain curve. The found values for the diamond model were ranging between 0.8 and 2.9% strain, which are more realistic values. And pointing out that a printing angle between 20° and 30° would match the ligaments 2-3% toe region. The fact that mentioned difference between the force/strain and the maximum stress/strain curve, only occurs in the diamond model is most likely due to the difference in fibre orientation. In the wave model, only the crimped fibres are loaded parallel to their orientation and the angle between the crimped fibres and the straight vertical fibres remains unchanged, as the vertical fibres are not placed under load. While in the diamond model, both fibres are loaded at an angle compared to their orientation. As the diamonds stretch out, the angle between the fibre’s changes, causing high internal stress at the intersections between the fibres, disrupting the simulated stress/strain curve.

3.3 Finetuning of MEW scaffold printing

For the finetuning of the MEW printing, the fibre diameter needed to be determined. The Translation speed of the collector plate is proportional to the diameter of the deposited fibres. Since, if the speed is increased, the fibre diameter decreases, as the polymer is stretched out. The decrease in fibre diameter with increased speed does feature diminished returns, an increase from 3mm/s to 4 mm/s decreases the fibre diameter far more significantly than an increase in speed from 7 mm/s to 8 mm/s. As all of the scaffolds printed were printed at a speed of 20mm/s or lower, the fibre diameter was only determined up to 20 mm/s. Aside from speed the length of the fibre alters the diameter as well, as the printing jet lag does need time to be build up, and short fibres do not allow for enough jet lag to be build up to significantly stretch the fibre out. In order to determine the fibre length, multiple fibres of 100mm in length were printed on a glass sheet and analysed to obtain the fibre diameter obtained for a certain TS. Figure 32 shows the measured fibre diameters, for reach TS used. The values are obtained using ImageJ, and the encoded distance between the fibres as a reference.

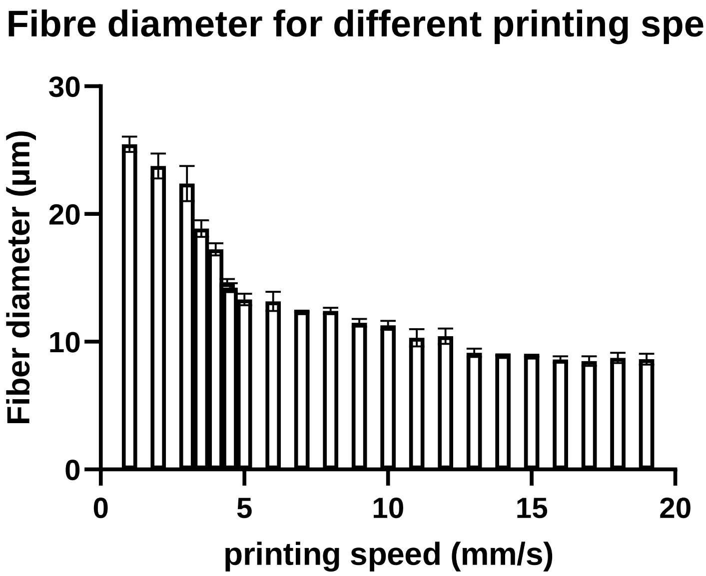

Figure 32: MEW fibres printed at different printing speed or TS, while using 0.5 Bar pressure and 6kV as voltage. Shown fibre diameter ranges from 26 to 8 µm depending on the TS.

3.3.1 Finetuning of crimped fibre printing.

The printing of crimped fibres is a delicate and very sensitive process, where even small adjustments to the parameters can fully disrupt the printing pattern. Because of this several parameters have to be carefully determined, in order to achieve a reliable print of a crimped wave pattern. The first parameter that was adjusted was finding the right TS both for the crimped fibres themselves as for the speed at which the vertical fibres are printed, form now referred to as the wave TS and the vertical TS. The vertical fibres have to be printed at a higher speed than the horizontal fibres, as the vertical fibres were observed to interfere with the crimped pattern. This interference decreased if the vertical fibres were printed at a higher speed, reducing their fibre size and potential for electrostatic interaction. To find the optimal parameters for printing of crimped wave patterns, several crimped models have been printed with speeds ranging from 3.0 to 4.6

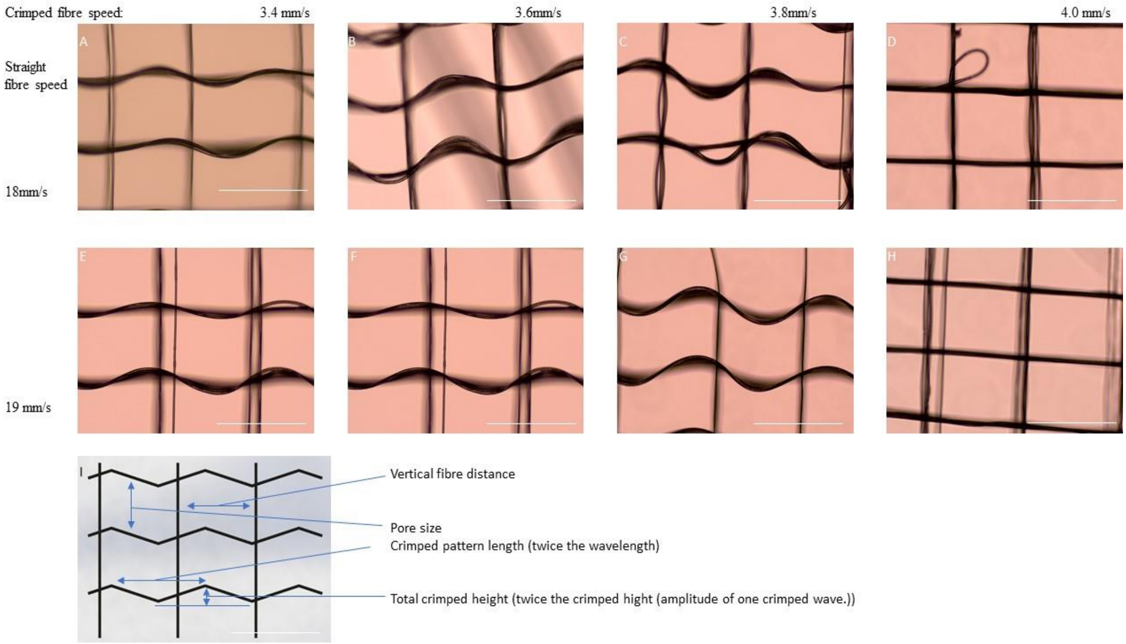

Figure 33: The 10% elongation diamond model printed at different crimped fibre and straight fibre speeds. Upper row (a, b, c, d) 3.4 mm/s (a), 3.6mm/s (b), 3.8 mm/s (c) and 4.0 mm/s (d) crimped fibre speeds with a vertical fibre speed of 18 mm/s. Middle row (e, f, g, h) 3.4 mm/s (e), 3.6mm/s (f), 3.8 mm/s (g) and 4.0 mm/s (h) crimped fibre speeds with a vertical fibre speed of 19 mm/s. i) The encoded printing pattern used to print shown scaffolds. Pore size was 350µm, fibre distance 500µm. All scale bars note 500 µm

mm/s in the crimped fibre direction. Speeds of 10 to 19 mm/s have been tried in the vertical direction. Results show that a wave TS of 3.6 or 3.8 mm/s as well as a vertical speed of 18 or 19 mm/s was necessary to be able to print crimped wave fibres. Figure 33 showcases scaffold that have been printed with a crimped fibre speed ranging from 3.4 mm/s to 4.0 mm/s, with a vertical fibre speed of 18 or 19 mm/s. A more accurate description would be to say that the crimped fibre speed is 0.6 mm/s faster than the CTS. This is because it is the difference between the CTS and the TS is what additionally stretches the fibre out (and disrupts the crimped pattern). And the exact value of the CTS is different depending on parameters as Needle temperature, pressure, voltage and humidity. The result is that the based on the humidity, a different TS will be ideal for printing. For example, a TS of 3.8mm/s was found to be ideal in figure 33, which was performed at 35% humidity. While at 40% humidity the ideal speed is up to 4.2 mm/s, the difference is shown in figure 34.

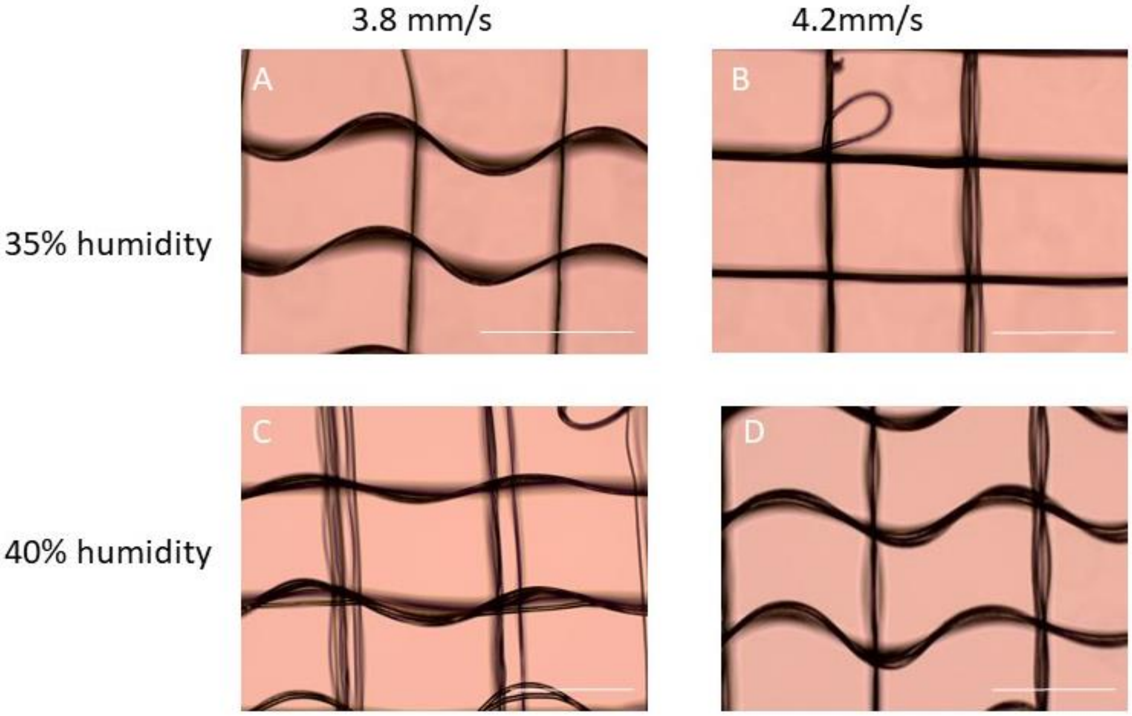

Figure 34: The ideal crimped pattern TS is dependent on the CTS, which is dependent on the humidity. At 35% humidity 3.8mm/s was ideal for producing waves (a), and 4.2mm/s would only yield straight lines (b), while at 40% humidity 3.8mm/s produces an irregular wave pattern (c), while 4.2 mm/s produces regular crimped fibres. (d) All scale bars note 500 µm.

Another variable that requires adjustment is the direction of printing. Due to the jet lag between the print head and the collection plate, there is a small phase shift between the print head and the collection plate. This lag results in printing patterns, when printed in opposite directions are not symmetrical, as there is a small difference in distance between the encoded start of the wave pattern, and the actual start of the wave pattern. Similarly, there is a delay between the encoded end of the wave pattern and the actual end of the wave pattern. This difference is visible in figure 35, where a vertical fibre is printed on the exact point encoded to be the end of the wave pattern, yet the wave pattern continues on for a bit longer. This difference leads to a small inconsistency in the placement of fibres when printed in opposite directions, causing the fibres to be placed closer to one

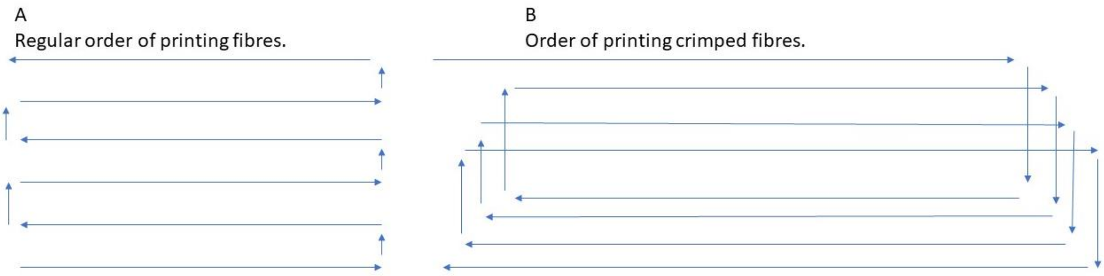

Figure 35: The regular order of placing fibres (a) and the order to place down fibres used for the production of crimped scaffolds (b). Important note is that the small (vertical) arrows are placed distanced from one another, and not on top of one another to keep the scaffold height consistent and keep the collector plate/printhead distance the same.

another than intended, resulting in electrostatic interaction between said fibres, this causes the fibre to be placed closer to the next fibre than intended. This process is repeated even stronger in the next layer, causing a loss of the crimp morphology, irregularities in pore size and sometimes even the cause the fibre to 'jump over' from one fibre to the other. The result of this interaction is shown in figure 37. This process can be prevented by increasing the pore size to the point that the distance weakened the electrostatic interaction, preventing said process. However, for better cell proliferation and adherence on the scaffold, it is better to decrease the pore size of the scaffold. To remedy this problem, it is possible to simply just print a crimped fibre, loop back to the start position, and print the next fibre. However, this is very time and polymer inefficient. Therefore, figure 36 shows a different order of laying down the fibres which has been adapted in order to place the fibres in the same printing direction as the fibres next to it. This solution allows for a smaller pore size of 350 µm to be reached without interaction between the fibres. All pictures previously shown were printed with a 350 µm pore size, using the method shown in figure 35.

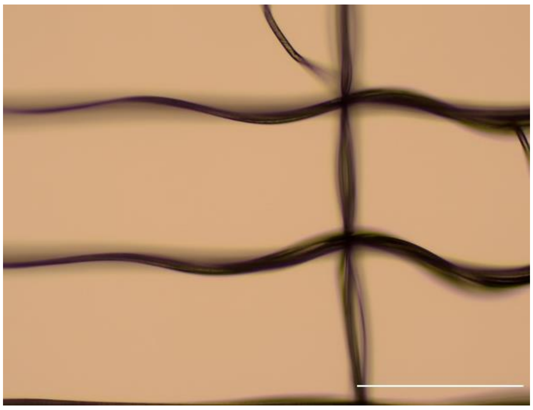

Figure 36: Delay between encoded end of wave pattern (vertical printed line) and the actual end of wave pattern visible on the image. Scale bar notes 500 µm.

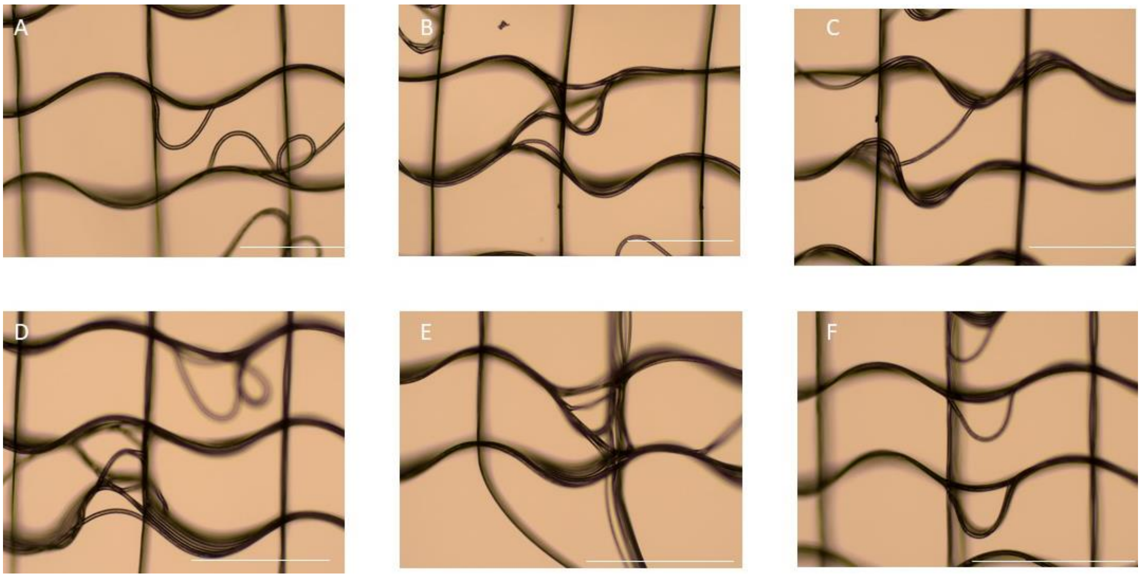

Figure 37: Examples of electrostatic interference between the printed crimped wave fibres. Above (a, b, c) shows electrostatic interaction due to fibres being printed in the opposite directions, at 350 µm pore size. Below (d, e, f) shows electrostatic interaction between fibres printed in the same direction at 300 µm pore size. Important to note is the fact that in below the fibres are in phase with one another, while above the fibres are not, an important distinction to differentiate fibre interaction due to a small pore size or due to the fibres being out of phase. All scale bars note 500 µm.

To further optimise the pore size, a pore size of 300 µm was printed using the same solution. However, the decrease in pore size did cause previously mentioned electrostatic interaction between the fibres, which is shown in figure 37. Hence why the wave model was printed at 350 µm pore size, at 0.6mm/s above CTS for the crimped fibres themselves.

3.3.2 Finetuning of diamond scaffold printing

The finetuning process of the diamond scaffold was significantly shorter than the finetuning needed for the crimped wave scaffolds. As shown form the Ansys simulations, a 5° printing angle was chosen as the optimal angle and 10° was chosen as the biggest angle still acceptable, if printing the 5° angle was not feasible. One major factor in this is the fact that there is no difference between the printing pattern and the resulting print. There was only one major obstacle to overcome, which is finding the correct TS. As the diamond scaffold is printed at a very small angle, there is the issue of electrostatic interaction between said fibres. As described in the methods, it is possible to simply

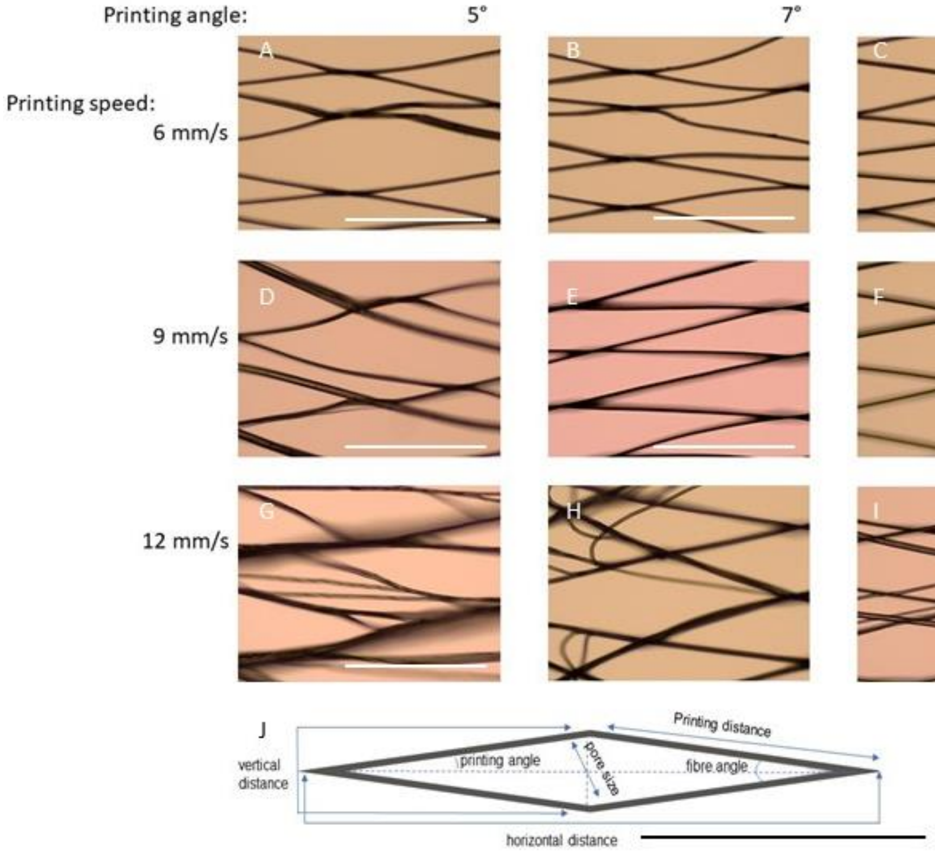

Figure 38: Optimalisation of the printing angle and speed for the diamond scaffold. Above: 5° (a), 7° (b) and 10° (c) printing angle diamond model printed at 6 mm/s TS. Middle: 5° (d), 7° (e) and 10° (f) printing angle diamond model printed at 9 mm/s TS. Below: 5° (g), 7° (h) and 10° (I) printing angle diamond model printed at 12 mm/s TS. J encoded printing path and parameters. Note the fibres interacting and sticking together at smaller speeds instead of crossing one another. While at a high speed the fibres are not being placed accurately. All scale bars note 1000mm

increase the speed, to thin the fibres out, problem is that if the speed is increased too much, the printed accuracy will decrease. To find the optimal parameters, scaffolds with a printing angle of 5°, 7° and 10° were printed with a TS ranging from 6mm/s to 12 mm/s. The results of which these optimisations are shown in figure 38. Both the 7° and 10° scaffolds were found to be printable, as long as the TS stayed below 12 mm/s, but above 6 mm/s. This is due to the fact that as the increase in speed decreases the accuracy in the fibres but decreasing the TS too much increases the fibre diameter, which in turn causes the fibres to interact with one another at the intersection. Significantly reducing the print accuracy and interrupting the diamond pattern. The 5° angle was found to not be reliably printable, as the range of speed where the fibres still interact to one another overlaps with the range of speed where the fibres themselves are not placed accurately anymore and become inaccurate. Because the 5° angle is not reliably printable, but the 7° angle model is, the 7° printing angle diamond model was chosen for further testing.

3.3.3 Comparison of diamond and wave scaffolds

In order to properly compare the printing accuracy, the difference between the encoded values and the actual printed values were compared between the optimised wave model and the optimised diamond model. Data points were collected from images of 3 different scaffolds. The following values were compared: The wave height and wavelength were measured for the wave model, as these were found to be the least inaccurate parameters. For the diamond model, the fibre angle, vertical distance and horizontal distance were compared, as all the other parameters can be calculated using these three.

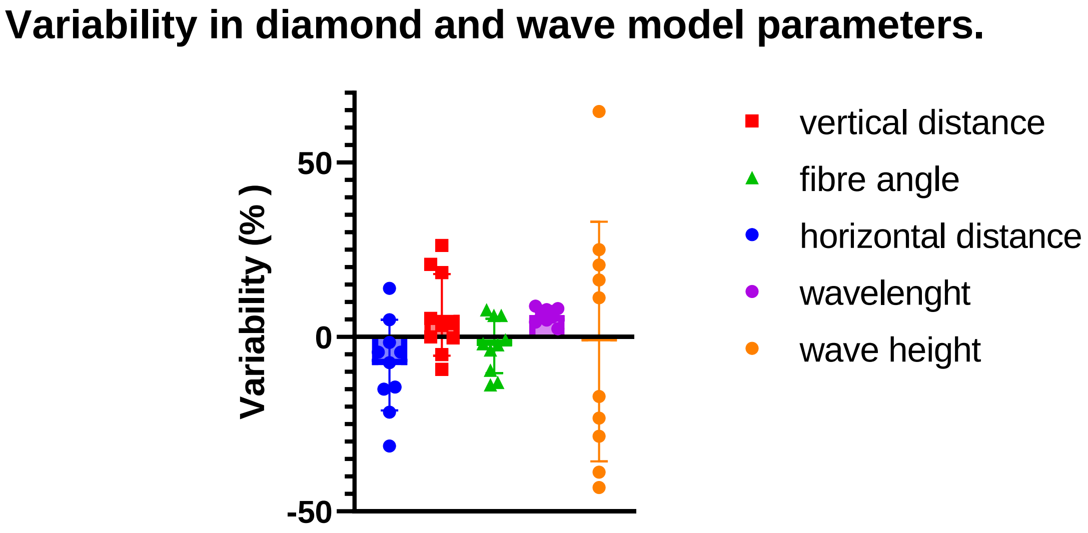

Figure 39: The variability of measured parameters in percentage of the encoded parameter

In figure 39 the compared results are shown. From this figure there is one parameter that is far more variable compared to the original encoded parameter, which is the wavelength in the wave model. The two least variable parameters are the wavelength in the wave model and the fibre angle in the diamond model. The factor most of interest is how the mentioned variability would affect the mechanical properties, most notably the toe region. Of the mentioned factors, the wavelength on its own does barely the mechanical properties, it is the ratio between wave height and wavelength that determines the mechanical factors. Given that the wave height is the most variable, opposed to the wavelength, it has to be concluded that the mechanical properties (the toe-region) experience severe variability. For the diamond model, the factor that influences the toe region the most is the fibre angle, which is shown to be very stable. The vertical and horizontal distance do show considerable variability, yet less variability than the wavelength, bringing the conclusion that the diamond printed model shows less variability.

Another, very significant factor to consider is that for the wave model, several scaffolds that were meant to be mechanically tested were rejected. This rejection was due to the scaffolds not showing a wave pattern at all. In other samples one fibre did show the wave pattern, but the next fibre did not, this problem did mostly show when printing larger scaffolds for mechanical testing. While for the diamond scaffold no scaffolds needed to be rejected. This lack of a wave pattern is based on the CTS, as the TS for the wave pattern is very closely related to the CTS, opposite to the diamond model. This CTS can change during the print due to a small change in humidity, small changes in the fibre yet due to the effect of continuously printing for hours. This change then can disrupt the wave pattern. It is possible to remedy this problem by testing for the CTS for every print starts, but this is not 100% effective, and the optimal par. Said problems have not once occurred during the printing of diamond models, once the parameters discussed in 3.3.2 were established, despite a larger number of diamond scaffolds being printed. Due to the fact that diamond scaffolds show less variability and can be printed far more reliably, MEW printing wise, the diamond would be favoured for usage, provided it can match the mechanical properties of the wave model.

3.4 Mechanical testing MEW scaffolds

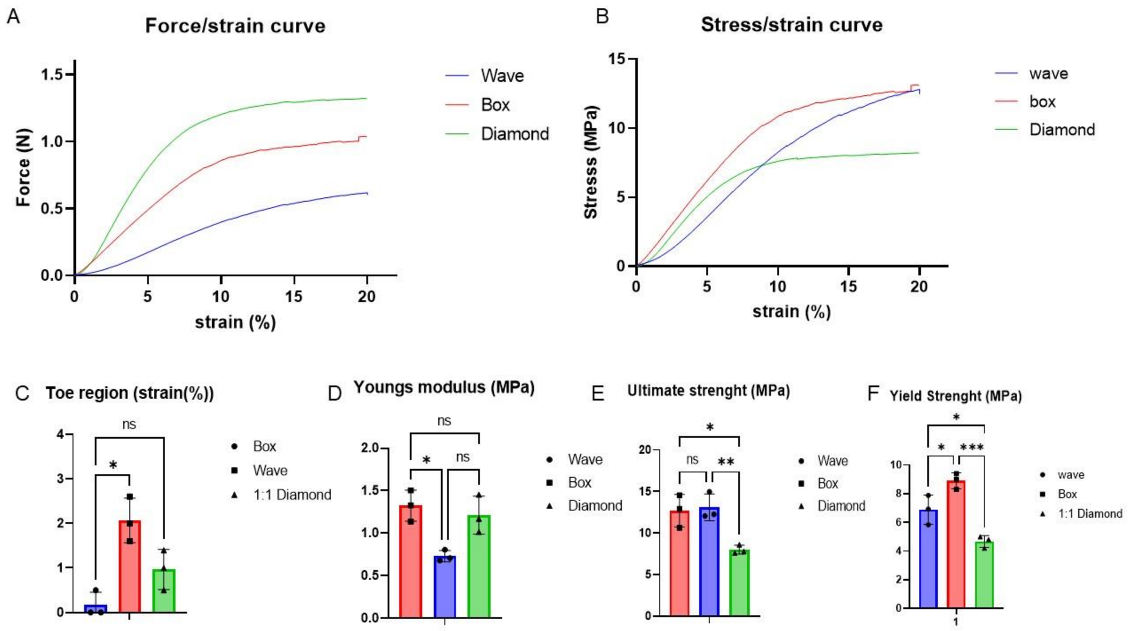

Figure 40: Tensile mechanical properties of the developed wave model and diamond scaffolds, a square box plot is used as a control, n=3. a) averaged force strain curve, b) averaged stress/strain curve, c, d, e, f) box plots of toe region in percent strain (c), Youngs modulus (d), Ultimate strength (e) and Yield strength (f) * notes $p<0.05$ significant difference, ** notes $p<0.001$ significant difference * notes $p<0.0005$ significant difference**

Three groups underwent tensile mechanical tests, the developed wave and diamond models, and a square box plot, consisting of fibres printing in a straight line. The results can be seen in figure 40. The latter serves as a control group, to confirm that the printing pattern is responsible for the toe region. The control group showed next to no toe region (mean of 0.1%), while the wave and diamond models showed mean toe regions of 1.0% and 2.1 % strain respectively. The latter being comparable of the toe region of the native ligament, which is 2-3%.

The crimped architecture of the wave model is shown to impact the Youngs modulus, and the Yield strength, but not the Ultimate strength. This can be explained by the variability in the wavelength discussed prior. The toe region is produced when the waves with the smallest wave height are fully elongated and start to give resistance. All the while the waves with a higher wavelength slowly elongate further during the linear region, eventually offering resistance once those are fully elongated as well. This would explain the significantly lower Youngs Modulus in the linear region, as not all the fibres are fully elongated and offering resistance. It also explains why the ultimate strength is very similar to the straight fibre pattern as the wave fibres are transformed into straight fibres, once the failure region is reached, and should offer similar resistance to the box plot.

In the diamond model, the Youngs modulus is slightly, but not statistically significantly affected. However, the Yield strength and Ultimate strength are. This can be explained by the fact that the fibres are not printed in the direction of the tensile load, while both the wave and box control models are, and neither do they fully elongate in said direction as well, resulting in weaker fibres. It should be noted from figure 40 A that out of all the models tested the ultimate Force of the diamond model was by far the highest, despite the tested scaffolds having the same width (7mm) and height (200µm). The main reason for this is that the diamond model is far more dense in fibres, due to its diamond design, as there are two diagonal fibres in the diamond model for every straight fibre in the square box model per mm in width. This difference between the reaction force and calculated stress is due to the stress is calculated using the cross-section area of the fibres. The empty space between the fibres is not included in the model. Resulting in a far higher cross-section in the diamond model, in turn resulting in lower stress values. Yet it is important to note that when including the empty pores between the fibres in the stress calculations, the diamond model will be far stronger than any of the other models.

3.4.1 Mechanically testing altered diamond scaffolds.

As shown in the section 3.1, the FEA model showed that the toe region of the diamond model increases when its length is increases, as well as the fibres in the corner being the point where failure occurs. To validate this prediction, the previously tested diamonds were tested at a length of 10 mm (grip-to grip separation), and 7 mm grip. Additional diamond scaffolds being 30 by 7mm and 30 by 4 mm were tested. The goal was to see if a change occurs if the diamond model is longer, and to see if the width of the diamond model plays an additional role in the process. Finally, a 30 by 7 diamond was rolled up, as specified in the methods. This was done because unlike the wave model, the diamond model needs to decrease in width, to elongate the diamond structure, in order to have a toe region. By rolling the scaffold up the diamond, the model changes from a 2-dimensional model into a 3-dimensional model. And as a result the scaffold can thin in two dimensions, being elongated in the third. While previously the model could only decrease its width in 1 of the 2 dimensions, as MEW prints are mostly 2 dimensional. The second reason is that to match the dimensions of the ligament in the patient’s body, the MEW scaffold will most likely be rolled up when placed in the patient. Figure 41 shows the models being tested, while the results are displayed in figure 42.

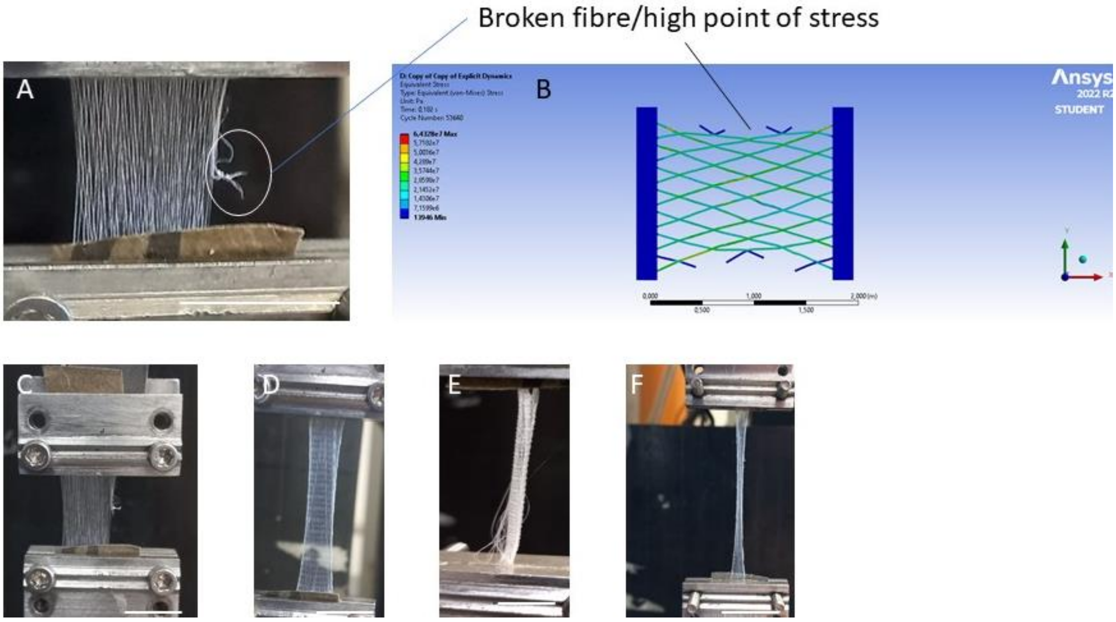

Figure 41: a, b) comparison between Ansys model and mechanical test performed, both pointing to the same point of failure, scale bar in b notes 2000mm. c) original 7 x 10 mm diamond model, d) 30 x 7 diamond model, e) rolled up 30 x 7 diamond model being tested. f) 30x 4 diamond model. Scale bars in a, c, d, e, and f note 5mm

It was shown that printing a longer scaffold does not significantly increase the toe region, going from 1% to 1.5% at most with the 30 by 7 mm scaffold, however these changes are not statistically significant. In addition, the toe region did not change between the 30 by 4 mm scaffolds, compared to the 30 by 7 scaffolds. Indicating that while the length of the diamond model might play a small part in the toe region, the width by itself does not.

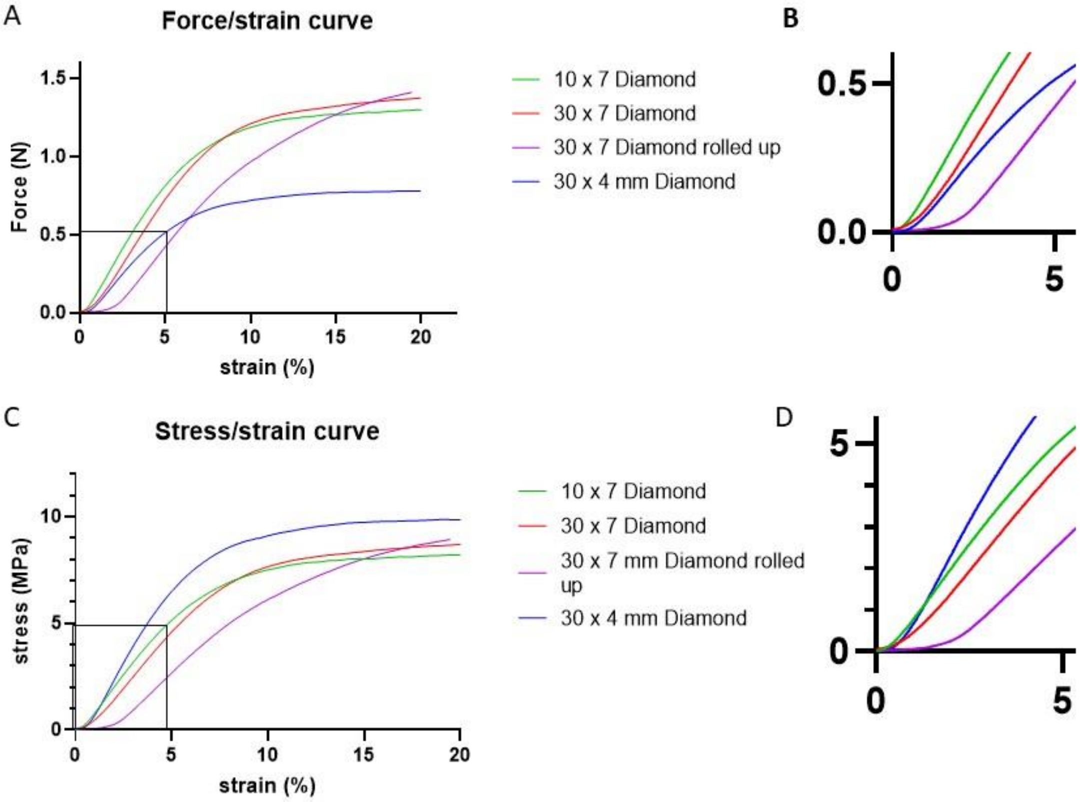

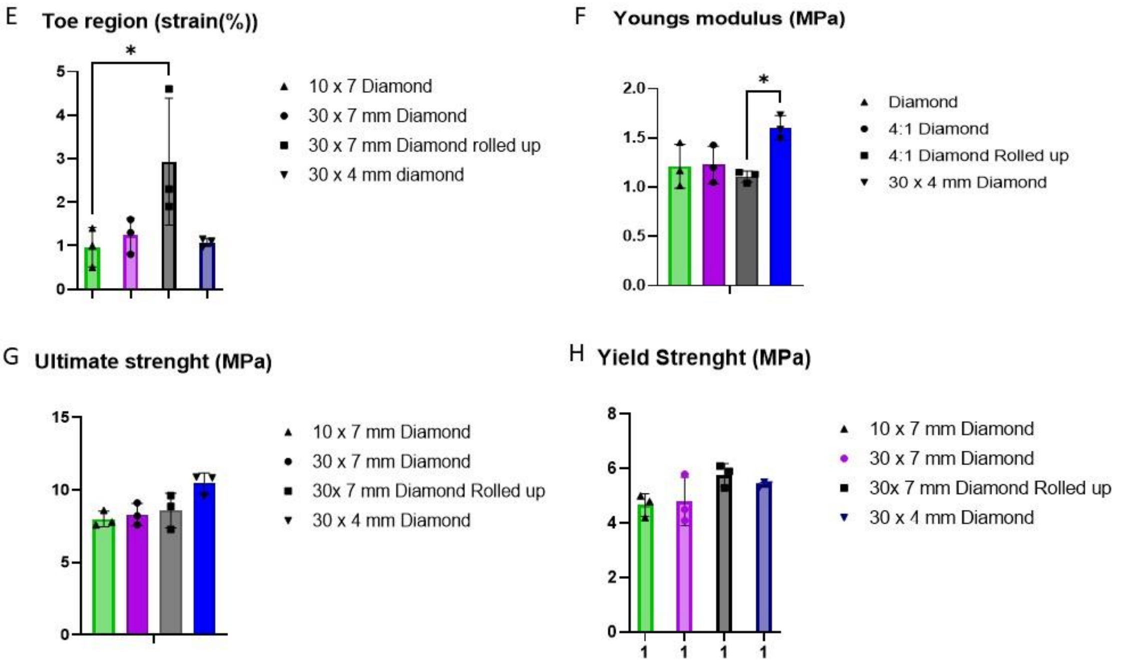

Figure 42: Tensile mechanical properties of the adjusted diamond scaffolds n=3. a) averaged force strain curve, b) averaged stress/strain curve, c, d, e, f) box plots of toe region in percent strain (c), Youngs modulus (d), Ultimate strength (e) and Yield strength (f) * notes $p<0.05$ significant difference, ** notes $p<0.001$ significant difference * notes $p<0.0005$ significant difference.**

The main find is in the rolled-up scaffold model, which has a statistically significant increase in the toe region, doubling its toe region and increasing up to an average of 2.9% and matching the toe region found in native ligament. This difference again is most likely due to the fact that only a part of the diamonds on the edge fully elongate, this is especially visible in 44B. By rolling up the diamond scaffold this edge is increased, allowing more of the diamonds to elongate. The Ultimate and Yield strength have not noticeably changed, which is expected, as the same model is being tested. And rolling up a scaffold or decreasing its size should not change the stress in the scaffold. Due to the ease of printing for the diamond scaffold, combined with the fact that it can be used to accurately achieve a toe region, the diamond model is chosen for the development and testing of a biphasic scaffold.

3.4.2 Comparison of mechanical tests with FEA model results.

To accurately compare the mechanical testing data with the FEA model, and account for the difference in dimensions. The stress was calculated from the force/reaction curve of both the wave and 7° printing angle 30x 7 mm diamond models, using a cross section of $40mm^2$ for each fibre. The resulting stress/strain curves are shown in figure 43.

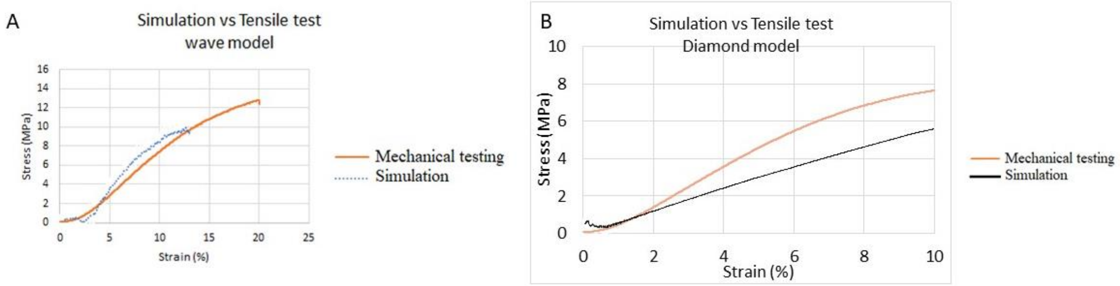

Figure 43: Comparison of stress/strain curve, calculated from reaction force, between simulation and tensile testing, for the wave model (a), and the diamond model (b).

Results between mechanical testing and simulation are remarkably close. For the wave model, testing showed a toe region of 2.3%, simulation showed a toe region of 4%. This difference could be explained by two different reasons. The first reason is that of pre-load, a preload of 0.001N was applied to the scaffold to ensure it was fully stretched out and the toe region did not originate from the scaffold being placed improperly. The issue being the accuracy of said preload, and the fact that the samples are very delicate. A load of 1N is enough to for plastic deformation, and a load of below 0.1 N is enough to fully stretch out the toe region. Because of this, it is very likely that the toe region of both the wave and diamond scaffolds was already slightly extended at the start of the test.

The next reason has to do with the previously discussed inaccuracy in wave height, and the fact that the ratio between wavelength and wave height heavily influences the toe region. Therefore, the waves which have a lower wave height, will have a smaller toe region and start to offer resistance sooner, resulting in a shorter toe region.

For the diamond model, both the simulation and the mechanical test arrive at a toe region of 1.0%, however the Youngs modulus of the simulation is shown to be lower, compared to the mechanical testing. An explanation could be that the current way the fibres are partially merged in the simulation, as shown in figure 27, is not fully accurate compared to how the fibres are melted together in the real model. This would make it easier for the fibres to move compared to one another, and affecting the mechanical stiffens. In conclusion, this comparison shows that it is possible to accurately predict a MEW printed scaffolds mechanical response using FEA. Provided the reaction force is used as the output of the simulation.

3.5 Using FEA to test biphasic scaffold design

To establish a biphasic scaffold design, the Ansys FEA model was deployed in order to map the deformation occurring in the interface region. Said deformation was used to calculate the strain occurring at that specific section in the scaffold, which was plotted against the strain occurring in the entire scaffold. In addition, the model is used to scan for stress build-up, to ensure that the difference in mechanical behaviour does not lead to stress shielding, leading to failure at the interface site. The two different sections of the scaffold were made up of region designed for ligament tissue engineering, the other being designed for bone tissue engineering. The ligament region was made up of the previously established diamond model. The bone region of the scaffold was made up of a square box

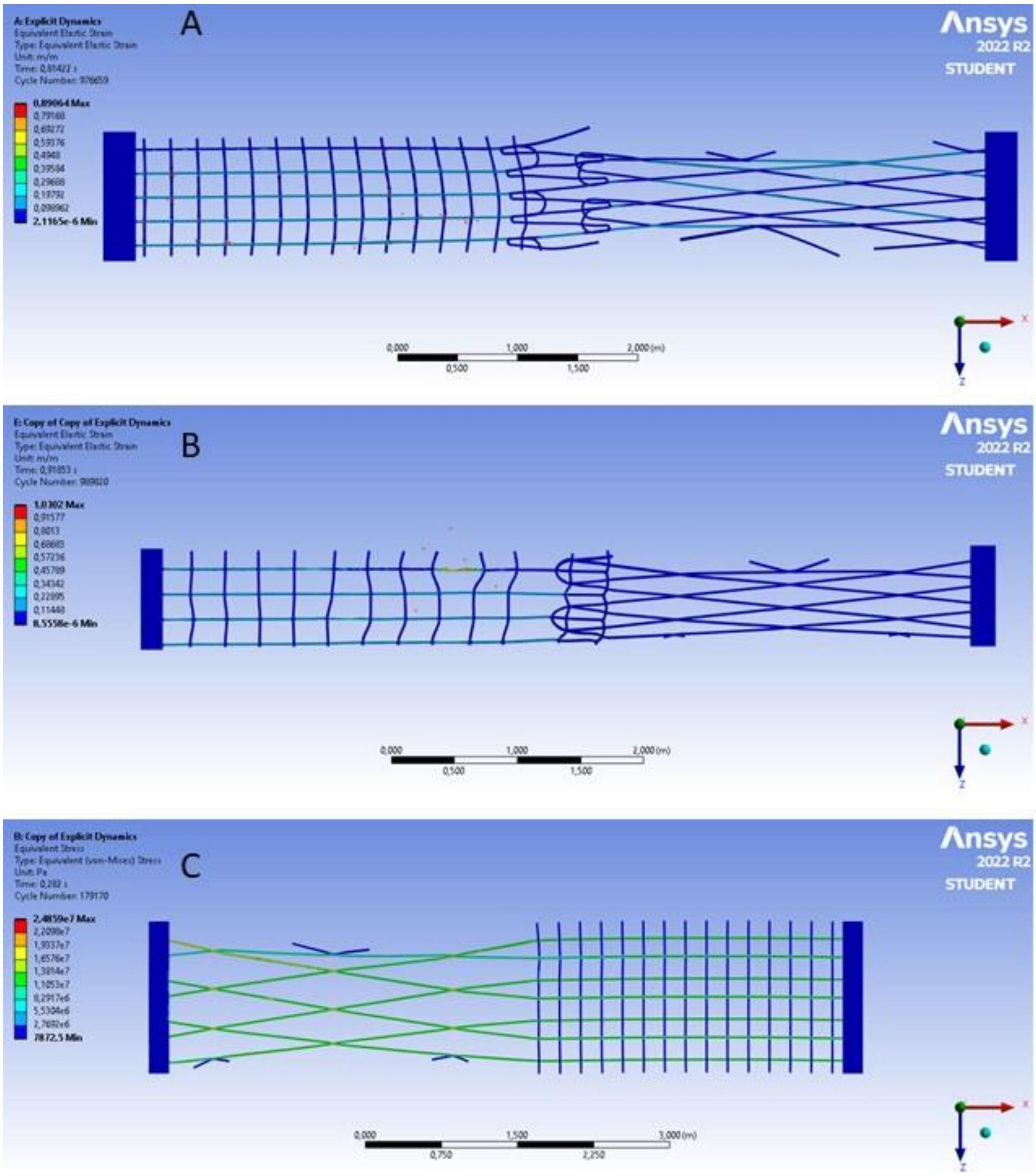

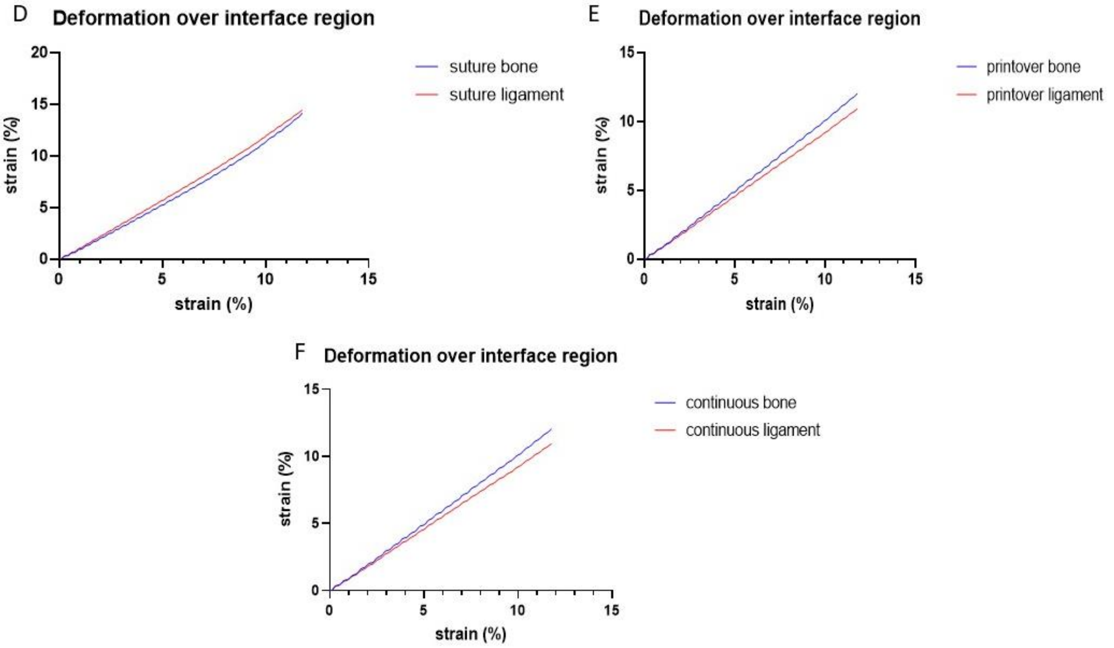

Figure 44: FEA analysis of the three biphasic designs. a) The suture model, b) the print over model, c) continuous model, continuous model shows the highest stress followed by the suture model. Scale bars note 3000mm. below the strain occurring at either site of the interface, distance between probes is 800mm, plotted against the strain for the entire scaffold for the suture model (d), the print over model (e) and the continuous model (f).

plot, the same which was used as a control in the tensile tests. Previous work done by Eichholz et al. [75] had shown that a square box plot is optimal for bone tissue engineering. Three different models were simulated, according to the designs specified in the methods section. A model where the fibres were printed continuously from one region to the other (the print over design). A model were both regions were printed separately, connected by a third print printed on top of both models (suture model). And a model were both regions were printed separately but were partially printed on top of one another to connect both scaffolds. All simulated scaffolds were simulated till established internal stress limit of 12 MPa was reached. Figure 44a, c show the results of the FEA simulation, both suture and print over model showed the highest stress in the bone region of the scaffold, while the continuous model showed the highest stress in the ligament region. This difference is most likely a result form the fact that the ligament region in both the print over and the suture model have a far higher fibre density than the ligament region in the continuous model. To choose a model to MEW print, the deformation probes placed on either side of the interface between both scaffolds (800mm distance between said probes). Using the results from the displacement probes strain that was occurring at the specific placement of the probe was calculated and plotted against the strain occurring in the entire scaffold. The resulting plots are visible in figure 44d, f. The goal of these probes was to quantify strain occurring in the interface region, and to establish which model did allow for a small amount of strain to occur in the interface region. While not causing a build-up of stress. The idea being to create an interface region whose mechanical properties are in between those of the bone and ligament region. Since the ligament region allows for a small amount of displacement without offering resistance. Ideally after the toe region in the ligament scaffold is reached, the interface region would then allow for little strain, after which the entire scaffold shows stiff behaviour. Two out of three of the modelled scaffolds show this mentioned small difference in strain, while one scaffolds does not show any strain occurring in the interface region. For this reason, the two scaffolds who did show strain occurring in the interface region, the print over and the continuous model, were chosen to be printed and mechanically tested.

3.6 Finetuning MEW printing of biphasic scaffolds

The printing of a continuous biphasic scaffold is a more complicated process than the printing of a scaffold with just one design. The main problem is the printing jet lag, as the polymer being printed takes the shortest route between the printing needle and the point where the fibre reaches the plate. Reducing the printing accuracy when changing the direction of the fibre being printed, making printing a scaffold with multiple designs difficult. This problem can be averted by reducing the TS, the issue is that the TS must be around 9mm/s in order to accurately the diamond pattern, as discussed in chapter 3.3.2. In order to still be able to print the two discussed scaffolds, a waiting step must be introduced when going from printing one design to the other. A waiting step is an encoded

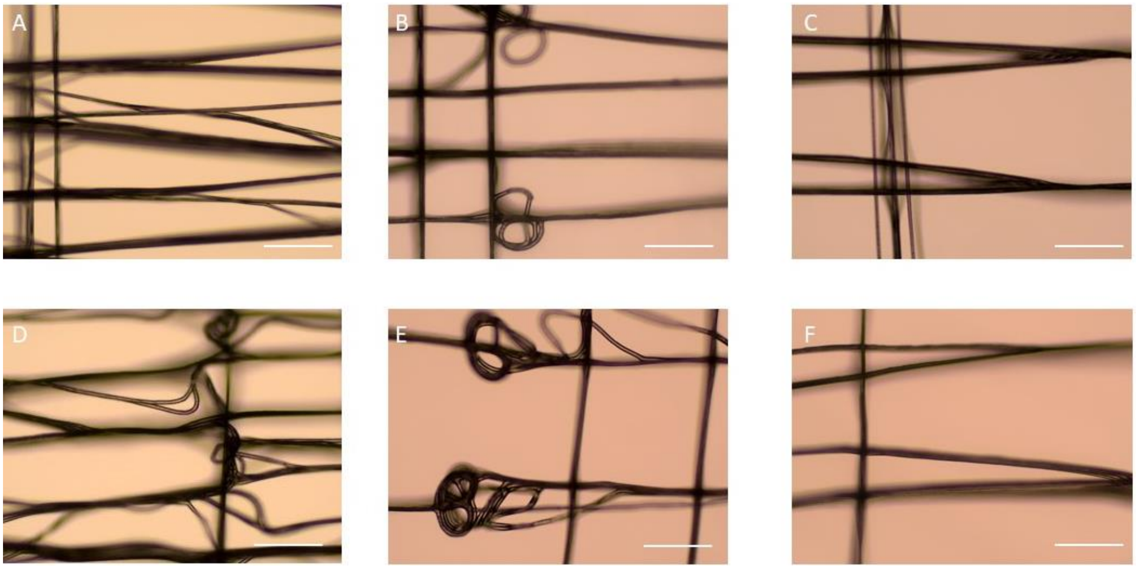

Figure 45: Optimisation of the continuous MEW model, left (a, d) interface between the two scaffolds with a waiting step of 300ms, decreasing printing accuracy. Middle (b, e) interface between the two scaffolds with a waiting step of 500ms, showing build-up of excess polymer at the interface border. Right (c, f) interface printed at 440ms waiting step, which was found to be the best middle way.

pause where the print head does not move compared to the printing plate, allowing the printed fibre to catch up and reducing the jet lag. The issue is that this waiting step must be carefully finetuned, as a short waiting step results in a low printing accuracy, while a higher waiting step results in a build-up of fibre at the print. Additionally, because the printing jet lag builds up during the printing of a continuous fibre, the waiting step needed is different depending on the TS and on the length of the previous fibre printed. To find the optimal waiting step, scaffolds were printed with a length of 30mm, to mimic the length of the ACL and therefore the length a tissue engineering scaffold for the ACL should be. A waiting step of figure 45 showcases the result of a low and high printing step, as well as scaffolds printed with a waiting step of 440 mms, which was found to be the best middle way between both extremes.

The printing of a print over model was a simpler affair, while similar issues arose due to the jet lag, there was one main optimisation to make. Scaffolds were printed with a ligament part of 30mm in length and a bone part of 30 mm in length, the overlap between both scaffolds was chosen to be 0.5 mm, mimicking the bone ligament interface, which is measured to be between 350 and 500 µm. Which is to have the same waiting step of 440 mms when the printhead just printed a straight fibre, but only a waiting step of 250 mms after moving the pore size and before printing the next fibres. Encoding both scaffolds to have a waiting step of 250 mms causes the fibres to cut the corner short and both scaffolds do not encounter one another. Examples are shown in figure 46.

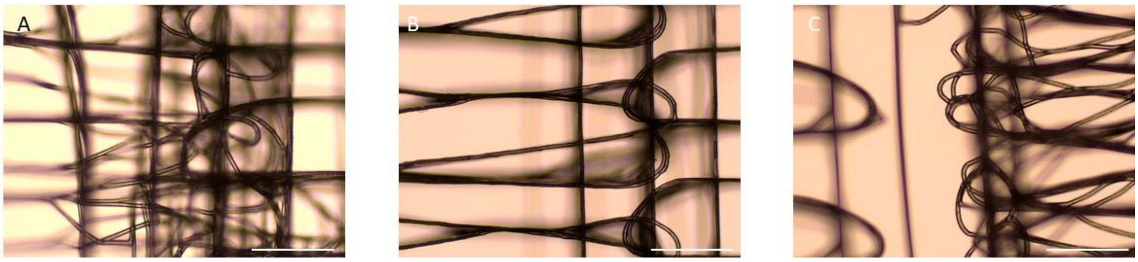

Figure 46: Optimisation of print over model, a) when the printing pause is 440 ms for both turns results in additional deposition of polymer, decreasing the printing accuracy, b)encoding the first printing pause to be 250 mms and the second printing pause to be 250 mms was found to achieve reliable results, c) encoding a printing pause of 250 ms for both turns resulted in an inaccurate deposition of fibres in the diamond model, as well as the two scaffolds to not come into contact.

3.7 Mechanical testing of biphasic scaffolds

Samples from both the print over and continuous print scaffolds underwent tensile mechanical testing (N=3). Tests are shown in figure 47 Sample width was 7mm, sample length was 60mm in total, 30mm consisting of the bone part, and 30 mm

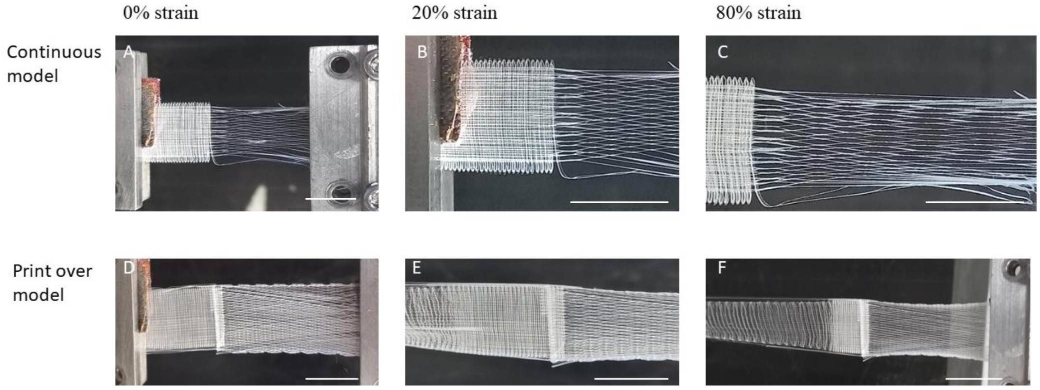

Figure 47: Photo images of the mechanical tests performed on the biphasic scaffolds. Upper: Mechanical test performed on the continuous model, form 0% strain (a), 20% (b), and 80% strain (c), images show the plastic deformation occurring in the ligament compartment. No mechanical failure was observed. Below: Mechanical test performed on the print over model, form 0% strain (d), 20% strain (e), 80% strain (f), images show the plastic deformation occurring in the bone compartment, starting at e and fully visible in f. Ligament compartment was shown to be thinner in e and f, compared to d, indicating the presence of a toe region. No deformation was observed in the interface region between both compartments. All scale bars note 7mm.

consisting of the ligament part. Samples were placed under up to 100% strain, to observe the failure mechanics and by observing which part of the scaffold shows plastic deformation, be able to tell the weak link in the scaffold (either the bone segment, the ligament segment or the interface in between.) Scaffolds were not rolled up for the tensile testing, to be able to better observe the interface region. Both models show toe region at 0.5% strain, exactly half the value of the toe region from only a diamond. A clear sign that the diamond half of the scaffold retains the nonlinear tensile response. For the print over model two different stresses are calculated, as both sections of the scaffold feature a different fibre density, and therefore a different cross-sectional area. Stress values were calculated for both the ligament (diamond) and the bone (square box) parts. Using the calculation for the bone scaffold, mechanical properties match those of the box plot tested previously, while using the calculation for the ligament scaffold, again the results matched the calculations used for the ligament scaffolds. Ultimate force however matched the ultimate force obtained from the box plot/bone scaffold for the print over Model. This can further be seen in figure 48, which also contains the parameters obtained from the control box scaffold, and the 30 x 7 mm diamond scaffold for comparison. It is shown that for the print over model, when placed under sufficient strain, it is the bone part that stretches out, indicating the bone part is the weakest link in the scaffold, due to its lower fibre density. Again, reinforcing that both sections in the scaffold retain their own mechanical properties. The Yield strength was not significantly different from ultimate force observed in the individually tested box plot, indicating similar mechanical strengths, as the bone part was observed to be the weakest section of the scaffold. The Youngs modulus was observed to be higher in the combined scaffold than in than in the tests of the single scaffold, but not statistically significantly different. For the continuous printing model, the ultimate strength and yield strength were observed to be slightly, but not significantly lower than those of the previously tested box scaffold. This is most likely due to the ligament part being the part that showed plastic deformation, indicating that with a similar fibre density the ligament model is slightly weaker than the bone model. That the ligament model is weaker, with similar number of fibres, can be explained by the direction of loading, the bone model is loaded in the direction the fibres are orientated, while

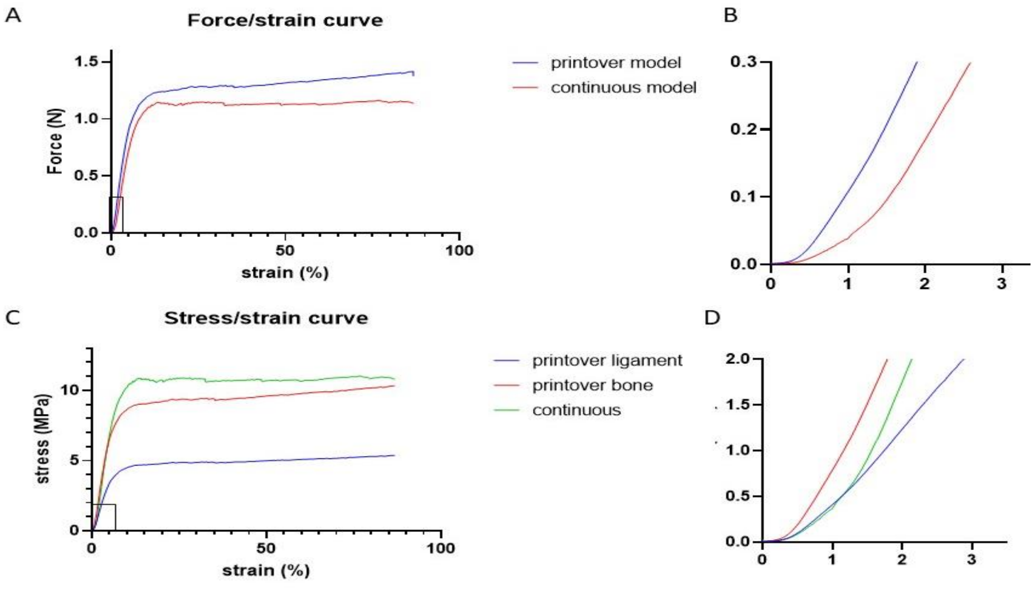

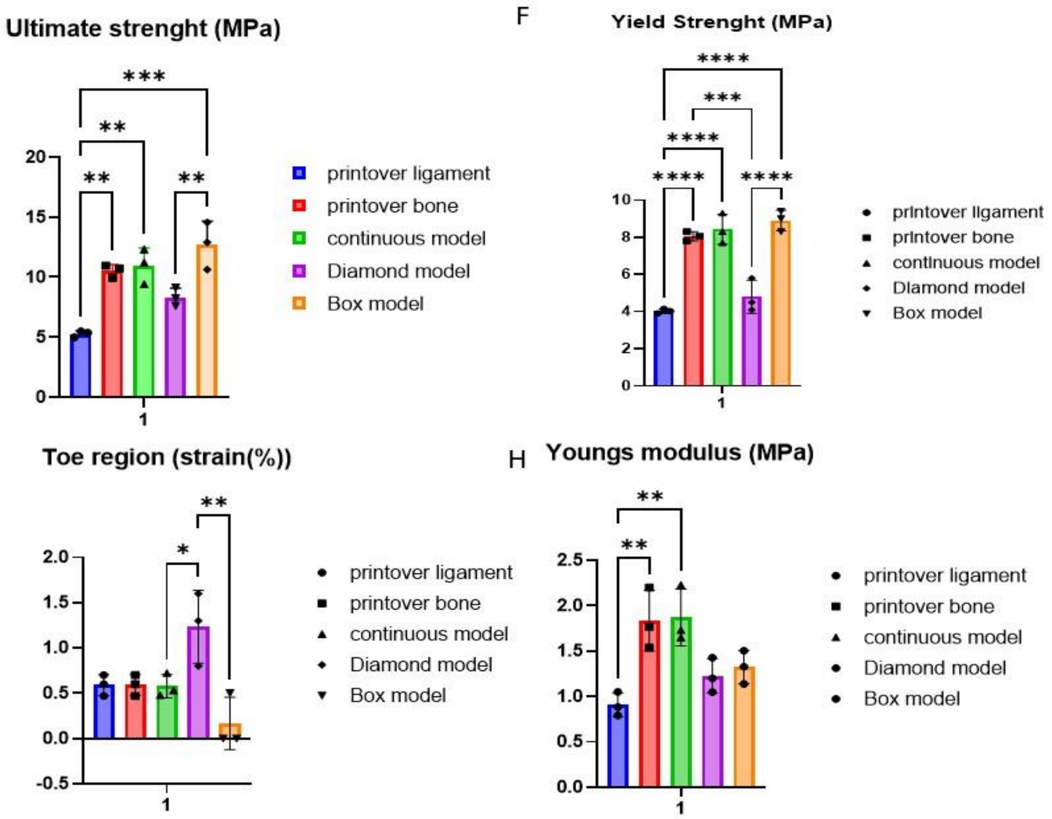

Figure 48: Tensile mechanical properties of the developed biphasic scaffolds, n=3. a) averaged force strain curve, b) enlargement of toe region area, c) averaged stress/strain curve, d) enlargement of the toe region area, e, f, g h) box plots of ultimate strength (e), Yield strength (f), toe region in percent strain (g), Youngs modulus (h) * notes $p<0.05$ significant difference, ** notes $p<0.001$ significant difference * notes $p<0.0005$ significant difference.**

in the ligament model the fibres are orientated in at a slight angle compared to their orientation, resulting in a weaker scaffold.

In conclusion mechanical tests show that both designs can be used to create a biphasic scaffold without a build-up of stress at the interface region, and while keeping the mechanical properties of both sections. In the print over model the bone section was shown to be the site of plastic deformation. While in the continuous model the ligament section was shown to be the site of plastic deformation.

4 Discussion

Currently ACL injury is a common soft tissue injury and places a significant socioeconomic burden on society. [1] In addition ACL injury shows a worrisome trend of increasing incidence rates in young adults, which is especially worrying as 50% of people suffering from an ACL injury are shown to develop osteoarthritis in the knee joint in 20 years' time, leading to a significant decrease of quality of life. [77, 78] Current surgical procedures are plagued by several complications, including aforementioned osteoarthritis, re-rupture of the ACL, degradation of knee cartilage, [12,79] introducing a need for Tissue Engineered solutions. A great deal of work has been done in researching scaffolds for tissue engineering. The main issue being designing a scaffold that both mimics the mechanical strength of native ACL, and features sufficient porosity to facilitate cell infiltration, has proven to be quite elusive. [34, 44] An additional challenge is the fact that produced scaffolds which do match the ACL's mechanical properties, such as braided electrospun fibres, or knitted silk scaffolds have insufficient cell migration. And the few cells migrating, are not provided with directional guidance to produce crimped fibres. [83, 35] To overcome this issue, a porous scaffold, which matches the ACL's mechanical properties, and provides directional guidance has to be developed. A relatively novel solution to try to achieve this is Melt Electrowriting (MEW), it has been shown that MEW printed scaffolds display exceptionally high cell migration and proliferation. Being able to provide directional guidance for fibres formed by said cells as well. [46, 66, 75] The main issue with MEW scaffolds is their relatively low mechanical strength, as observed in the previous mechanical tests the Youngs Modulus of the scaffolds ranged from 1 to 2 MPa, meanwhile the Youngs Modulus of the native ligament has been established to be between 60 and 120 MPa. [21, 23] It has to be pointed out that this is not the full picture. When a MEW scaffold is properly seeded with cells, these cells will form collagen fibres with parallel orientation to the MEW fibres, significantly increasing the mechanical strength. [46] The main hypothesis is that it is possible to print a MEW scaffold which mimics the mechanical properties of the ACL, save for the mechanical strength. Said scaffold can be seeded with cells which lay down fibres in a similar pattern as the printed MEW fibres, copying the mechanical properties induced by said pattern and significantly increasing the mechanical strength. This cell laden scaffold would then match all mechanical properties of the ACL and consist mainly of cells and their produced ECM. Which in turn would facilitate biological integration, while matching the mechanical properties of the ligament.

Another issue with tissue engineering a ligament is the attachment of said engineered ligament to the bone. This process is currently the main bottleneck in ligament tissue engineering. While research has been done in tissue engineering the interface between the bone and the ligament parts, a suitable model has not been developed yet. Current research did show that by designing a multi-phasic scaffold, consisting of a ligament section and a bone section, it is possible to tissue engineer a Bone-ligament interface, or enthesis as well. The main drawback of these studies is that while electrospun fibres and 3d printed fibres were used for directional guidance. This directional guidance did not match the direction of the collagen fibres in the BLJ. Studies consisted of distinct layers, each promoting either bone or ligament formation, with no fibres being placed going from one section to the other. As a result, the resulting enthesis were significantly less organised than the original tissue. [52-55] It is hypothesised that by designing a MEW fibrous scaffold, which consists of a bone section, a ligament section, which contains fibres travelling from one section to the other. It would be possible to provide directional guidance for the collagen fibres to connect from one section to the other, resulting in a significantly better organised interface section.

For the development of said interface section, as well as for the development of a scaffold which matches the mechanical properties, it would be beneficial to be able to predict the mechanical response of said scaffold. As shown during the mechanical testing, the scaffolds are very delicate, as a force as less as 1N could cause plastic deformation. Said delicacy, combined with the fact that a small pre-load must be applied, in order to ensure the scaffold is fully straight, make it difficult to determine a toe region. In addition, for the biphasic scaffold, it is crucial that there is no build-up of stress in the interface section between both sections, which is very difficult to determine using tensile testing. For these reasons a FEA model was developed consisting of a scale model of one printed layer of the scaffold design.

4.1 Develop an FEA model to predict the mechanical response from a MEW scaffold.

Regarding both the distribution of stress, as well as the toe region, the FEA model showed high accuracy, showing a similar toe region as the tensile test, as well as correctly pointing out the points of failure. Especially for the biphasic scaffold, the predictions which area would have the highest stress. Together with the fact that the FEA model predicted that only the diamond section of the scaffold would be thinned out in a similar fashion to during mechanical testing. While the diamond model retained its width, as expectation was that the diamond model would become thinner at the interface as well. However, from the many optimization steps necessary it was clear that the Ansys FEA model was not designed for such scaffolds. In order for Ansys to work as intended the mesh size had to be made half the size of the fibre diameter of the model, resulting in a very high mesh number, resulting in high simulation times (around 30 hours for the diamond models, and up to 120 hours for the biphasic models.) This high mesh number mend that the simulated scaffolds could only contain so many repeating units. If not taking the scaffold height/height/number of layers into account and adjusting for the fact that the FEA models are scale models. Then the size of the FEA models was around 1% of the size of the MEW printed the modelled scaffolds.

This is a limitation as especially the diamond model, which was shown to display a significantly larger toe region when it was rolled up. For this specific reason the models were made with a similar ratio between dimensions and showed great similarity. It was attempted to model the diamond scaffold while it was rolled up, unfortunately said model resulted in the used computer repeatably crashing. Additional limitations in the FEA model was that the comparison with the mechanical test showcased that only the reaction force was a reliable parameter to compare, which is not surprising in itself, as the internal stress can easily be affected by a high stress occurring in one specific part. The downside of this fact are the heavy oscillations shown by the reaction force, when simulating either the diamond or wave model. It was shown to be possible to use damping to reduce the oscillations to a point where they could be made readable using the movable average function of Excel. However, said steps do decrease the accuracy, and add additional computation time. The final limitation is that the FEA model can be used to model the mechanical response of a MEW scaffold by itself. However, MEW scaffolds are often being coated with chemicals to increase their biological potency, [83] something the FEA model does not take in account. Similarly, seeding cells on a MEW scaffold would alter its mechanical response as well, as these cells will mechanically interact with the scaffold, and again the FEA model cannot account for this. That being said, these two factors can be accounted for by altering the design, to account for a larger toe region. As said cells and coating are more likely to decrease the toe region, rather than increase it. This process would require a certain amount of finetuning, testing multiple scaffold designs, to establish the effect cells and coatings would have on the mechanical response of the scaffold. In conclusion, despite all the alterations that are needed to be made in order to use the model, the developed FEA model can be used to accurately determine the mechanical response of different designs for both single and biphasic scaffolds. However, it does take significant computational capacity and is limited to small models, which are not altered in any other way post printing.

4.2 Developing a MEW printed scaffold for ligament tissue engineering

This study has compared using MEW to print a crimped wave pattern scaffold or using a diamond scaffold for ligament tissue engineering. It has been shown during mechanical testing that both scaffolds can be utilised to produce a scaffold possessing a toe region, mimicking those of the native ligament. Out of those two scaffold the diamond model has been shown to be printed far more reliably. Diamond scaffolds were printed at a far smaller angle of 7° compared previously performed 30° in literature. [56] Diamond scaffolds were printed with less variability compared to the wave model. While the parameters for the wave model needed to be adjusted for every scaffold printed based on factors as humidity, but also the amount of time the MEW printer has been printing as well. It was observed that the profile of the printing jet, and with it the CTS changed slightly over the duration of the print, even when humidity stayed the same. These small changes were observed to interrupt the wave pattern. That the reliability of a print decreases when the time of printing increases is a serious issue. As the largest scaffolds printed did match the ACL in length of 30 mm, they did not match the ACL cross-section area. The cross Area of the wave model was around 1.4 mm^2, indicating a need for a roughly 30 times larger scaffold print to match the cross-section area of the ACL. Opposite to this, the diamond model showed no difference in printing accuracy based on the time the MEW printer was in use. Making the diamond model far more suitable for large scale production. Or printing larger samples in general. The diamond model does have the drawback that its mechanical properties can be altered by the way it is handled, as demonstrated by the fact that the toe region was significantly larger in the rolled-up model. The counterargument to this is that these differences were reliably shown by all of the diamond scaffolds. This lack of variability makes mapping the different factors that affect the toe region significantly more accurate, allowing designs to be planned around said factors.

A more serious concern for the diamond scaffold is the way cells would react to the diamond model compared to the wave model. A crimped wave model was partially chosen in the hope that perfectly mimicking the native collagen, including its crimped pattern, would encourage cells to differentiate into ligamentocytes. One major counterargument to this is the fact that the crimp pattern in native ACL is around 23-25µm in length and 5µm in height. [4, 8, 9] This is approximately 12 times smaller than the 300µm crimp length printed in the wave scaffold. Smaller crimp patterns can unfortunately not be printed. But this difference in size does raise a question: As the crimp pattern is roughly 12 times larger, does the similarity of the crimped shape of the native ACL have any influence? Or does any pattern that causes a similar toe region result in a similar effect, and are factors as material used for printing and pore size of more importance? To answer this question, cellular work would need to be done, and cells would be seeded on both scaffolds. To monitor and measure collagen production and orientation in both models, to ensure that the diamond scaffold can show similar results to the wave model. The second concern with the diamond scaffold, which again could only be answered with cellular work has to do with the small printing angles used. As outlined in table 2, on page 42 in chapter 2.2, in the 7° printing the distance between two fibres in the longitudinal direction, or the direction designed can be up to 1642 µm, while distance between crossing fibres is 827µm, despite the pore size, e.g., the shortest possible distance between two fibres only being 200µm. For comparison in the wave model the distance between fibres is between 300µm and 500 µm, depending on direction. The issue that arises is that current work on with cells has shown that the addition of cross fibres improves the cellular adhesion of the scaffold. It is shown that cross fibres help give cells additional structures to adhere and attach to. [83, 84] The fact that this diamond design leaves such a large distance between mentioned corners does raises concerns for the ability of cells to adhere to the scaffold. Again, this question could be answered using cellular work, measuring the adherence of cells and seeing if produced collagen still is influenced by fibre direction, as is shown in scaffolds with a 90° printing angle. It should be noted that because it is likely that the toe region will decrease after introduction of cells. Additionally, diamond scaffolds with a larger printing angle (up to 45°) feature a larger toe region, and a shorter distance between cross fibres, as shown in chapter 2.2. These two facts combined could mean that the previously mentioned concerns could be resolved by using a larger printing angle. The final concern regarding both the wave and diamond models, is the fact that the scaffolds are very weak, showing a Youngs modulus between 1 and 1.5 MPa. Native ACL has a Youngs modulus between 120 and 60 MPa, which is a significant difference in mechanical strength to overcome solely by seeding cells on the scaffold. The main limitation in this regard is the fact that for MEW printing PCL is by far the golden standard, limiting the scaffolds to its mechanical properties. [59] In conclusion this study has shown that a diamond model is significantly easier to print and can be used to mimic the mechanical properties of the ACL as well as a crimped wave pattern can do. However cellular work would be needed to confirm if said diamond scaffold would facilitate cell deposition as well due to its low printing angle and subsequent distance between fibres crossing one another.

4.3 Designing a biphasic scaffold containing a bone and ligament compartment.

This study showed the possibility of printing a biphasic scaffold where each section of the scaffold kept their specific mechanical properties. It has been shown during mechanical testing that no stress build up at the interface section. In addition, it showed that the diamond models retained their toe section. Surprisingly while the ligament section of the scaffold became thinner to form its toe section, no such effect was observed in the bone section. Strongly indicating the individual sections keep their mechanical properties. Surprisingly, literary findings show that MEW biphasic scaffolds do show failure at the interface site between both regions. [66] A possible explanation for this could be that the Tensile and Ultimate strengths of both sections of the scaffold are similar to one another in the designs found in literature. In the designs shown in this study this was not the case, as both designs featured one section having lower Tensile and Ultimate strength than the other. The result could be that because one section was mechanically weaker, it absorbed most of the stress away from the rest of the scaffold, including the interface. While in a design were both sections are equally strong, the stress would not be directed to one section, and the failure would occur at the interface region. If this is the case, it would mean that printing a biphasic scaffold using the box and the wave design would be difficult, since both have similar mechanical strengths.

For the current used designs, both the print over model and the continuous model do have their own advantages and disadvantages. For the print over model, the main disadvantage is that with MEW printed scaffold, the edges of the scaffold tend to be printed with a lower accuracy caused by the printhead ‘turning around’ when finishing printing one fibre and moving to print the next fibre. Normally this is not a concern, as the edges of the scaffold can be cut out. In fact, it is standard procedure to use a biopsy punch, to create small scaffolds to seed cells on, completely avoiding the decrease in accuracy at the edges of the scaffold. In the print over model, this cannot be done, as the edge of both bone and ligament sections are an essential part of the scaffold. This study has demonstrated that it is possible to significantly increase said accuracy by adding and adjusting a waiting step when the printing pattern turns a corner. However, as the printing jet lag increases based on the length of the fibre printed (assuming all other parameters stay the same) this value will have to be adjusted for every scaffold design. The continuous model does not have mentioned drawback. Furthermore, in the continuous model the fibres continue straight from the ligament section into the bone section. This indicates that the continuous model provides far better directional guidance for fibres to form from the ligament section into the bone section, connecting the two tissues. This being said, the continuous model has severe drawbacks on its own. The first being that the pore size of the bone section must be half the pore size of the ligament section. This difference is due to the fact that the ligament section consists of two groups of diagonal fibres, with both fibres continuing to the bone model. Therefore, from the fibres present in the bone model, half of the fibres become one group of diagonal fibres at -7° angle. While the other group becomes the other half of diagonal fibres at 7° angle. Essentially doubling the pore size in the ligament region. Which is problematic in regard to the concerns for the diamond scaffold mentioned in 4.3 concerning the distance between fibres crossing one another. The other downside is that in the continuous model, plastid deformation occurs in the ligament section, while in the print over model, said deformation occurs in the bone region. Essentially, in the print over model, when placed under strain, first the ligament section elongates for the toe region. Afterward the majority of stress, and consequent deformation is placed on the bone region, indicating the scaffold will transfer the force to the bone

region. Similar to the native ligament. [13] In the continuous model however, the plastic deformation occurs in the ligament section. When placed under deformation, the ligament has to absorb all of the stress, instead of passing said stress on into the bone section. In addition, in the print over model the pore size for one of the two sections can be changed without altering the pore size in the other section. Since both sections are printed independent, this alteration can be made to adjust mechanical properties.
It should be noted that this conclusion regarding mechanical strength is limited to the MEW scaffolds by themselves. The mechanical properties could drastically change when the scaffolds are seeded with cells, and ECM produced by said cells start altering the mechanical properties. This is especially the case if issue with the bigger pore size in the continuous model can be overcome.

In conclusion, both approaches show promise in that the individual regions retain their mechanical properties in both models. Regarding the distribution of stress, and location of plastic deformation occurring, the print over model shows improved mechanical properties, and a greater adjustability of said mechanical properties.

4.4 Limitations

The main limitation of this study lies in the fact that no cell work could be performed to validate if the mechanical properties of the MEW models, translate to the ECM deposited by seeded cells. Especially regarding the biphasic scaffold, as the different printing patterns are not likely to cause two distinct tissues to develop. A way to overcome this is the previously mentioned coating of MEW scaffolds. It has been shown that coating a MEW scaffold in hydroxy apatite does significantly increase mineralisation and bone formation. [75] If only bone section is coated, or if the bone section is coated multiple times, each time only coating a slightly smaller part of the scaffold to create a degree of mineralisation. While similar approaches can be used for the ligament section as well. [59] Examples include using reactive star shaped polyethylene oxide based prepolymers (NCO-sP(EO-stat-PO) as a coating in order to improve the hydrophilic abilities of the scaffold and increase the cellular response. [85]
The main reason cellular work was not performed was due to time, time was needed to learn to properly utilise the MEW, to optimise the scaffolds, to develop the FEA model. Cellular studies would have taken up a significant portion of time.

Especially since out of recent studies, the only study where the cells occupy over 95% of the scaffold, did incubate their scaffolds for 6 weeks. [46, 66, 84]

Other limitations of the study include the fact that the ECM of a ligament is a complex structure containing far biological molecules more than just the collagen fibres. These molecules include elastin and proteoglycans, which are not mimicked in this study.

Another limitation of this study is the general flatness of the produced scaffolds, being 35 times larger in width than in height, and 150 times larger in length, compared to width. In comparison the ACL has a more cylindrical shape, with width and length being similar to one another, and around 4 times smaller than the height. [2]

This could be remedied by rolling up the scaffold, as demonstrated in this study. The main issue is that the fabricated scaffolds are very delicate and careful handling is necessary. This delicacy makes rolling up the scaffold difficult. In this study the scaffolds were rolled up using cigarette paper as an intermediate to reduce the force transmitted to the scaffold. Then the paper was rolled around a small metal pin, to reduce variability. This method raises several concerns regarding sterilisation of the scaffolds before cellular testing. And this method also leaves a hollow section in the middle, something which native ACL does not possess.

4.5 Impact and future work

This study presented an accurate FEA model to predict the mechanical response of a MEW scaffold. In addition, this study provided insight in the multiple approaches to alter the mechanical response of a MEW scaffold using different scaffold designs, and the limitations of said methods. Additionally, this study showed the possibility of creating multi-phasic MEW scaffold, without the interface being the region of failure. Where both regions retain their mechanical properties, as well the possibility of providing directional guidance between said sections.

Future work is needed to biologically evaluate the results of this study and if the properties of the MEW scaffolds will translate into tissue engineered on those scaffolds. Most crucial is if it is possible to significantly increase the mechanical strength of the MEW scaffolds, by the ECM deposited by the cells. As of now the MEW scaffolds on their own are far too weak to replace an ACL. If the scaffold is still mechanically insufficiently strong, it is possible to combine the mew scaffold with another material. Examples would include braided electrospun fibres, which are far more dense, and mechanically stronger.

Alternative approaches would include MEW but using another polymer, currently MEW is largely limited to PCL, but this could change in the future. Other improvements for future work include improving the method of rolling up the scaffold, to closer match the ligaments dimensions. Or a similar method could be used, with the scaffold being rolled up around another material being used to reinforce the scaffold, to ensure sufficient mechanical strength.

Lastly, mechanical testing would need to be done regarding cyclic loading of the ligament, as native ACL undergoes cyclic loading during the gait cycle. Resulting in a need to explore the any scaffolds response to cyclic loading, before considering the scaffold for ligament TE.

5 Conclusions

ACL injuries are one of the most common soft-tissue injuries, often requiring surgical intervention due to their poor healing capacity. Current surgical solutions have severe drawbacks, leading to a rising demand for Tissue engineering solutions. Despite decades of research, developing a scaffold for tissue engineering has proven to be quite elusive. The main difficulties being regarding the complex, load bearing, non-linear mechanical properties of the ligament. To match these properties and have sufficient porosity in the scaffold to allow for proper biological integration has proven to be difficult.

In addition, a current bottleneck in tissue engineering of a ligament is the attachment of said ligament to the bone.

In this study, it has been shown that multiple MEW based scaffold designs can be used to match the non-linear response of the ligament, not just a wave pattern. Diamond scaffolds were shown to also be able to mimic the ligaments non-linear response, while showing far more reliable printability. Both designs were printed and underwent extensive mechanical testing, establishing the toe region developed in both scaffolds. The diamond model was shown to possess a toe regions similar to the wave pattern. Combined with the ease of printability the diamond model was shown to be the most valid design of the two.

To accurately predict the mechanical properties of a scaffold without the need to develop printing protocols for said scaffold, an FEA model was developed. This printing model has been validated against multiple scaffold designs and is shown to accurately determine a potential toe region, as well as area of failure.

Biphasic scaffolds were simulated using the validated FEA model and based on its results designs were chosen to be MEW printed. Extensive mechanical testing of printed biphasic scaffolds showed either section in the scaffold retained their mechanical properties, even toe regions in the diamond. In conclusion this study showed the possibility of printing biphasic scaffolds for bone-ligament tissue engineering. Featuring vastly different mechanical properties in either region, without mechanical failure occurring in the interface.

List of Literature

[1] Kuo, C. K., Marturano, J. E., & Tuan, R. S, Novel strategies in tendon and ligament tissue engineering: Advanced biomaterials and regeneration motifs. *BMC Sports Science, Medicine and Rehabilitation*, *2*(1), 20, 2010.

[2] Duthon, V. B., Barea, C., Abrassart, S., Fasel, J. H., Fritschy, D., & Ménétrey, J. Anatomy of the anterior cruciate ligament. *Knee Surgery, Sports Traumatology, Arthroscopy*, *14*(3), 204-213, 2006.

[3] Menghini, D., Kaushal, S. G., Flannery, S. W., Ecklund, K., Murray, M. M., Fleming, B. C., & Kiapour, A. M. Three-dimensional magnetic resonance imaging analysis shows sex-specific patterns in changes in anterior cruciate ligament cross-sectional area along its length. *Journal of Orthopaedic Research*, 2022.

[4] Lim, W. L., Liau, L. L., Ng, M. H., Chowdhury, S. R., & Law, J. X. Current Progress in Tendon and Ligament Tissue Engineering. *Tissue Engineering and Regenerative Medicine*, *16*(6), 2019.

[5] Bandyopadhyay, A., & Shaharudin, S. Anterior Cruciate Ligament Injuries in Soccer Players : An Overview, International Journal of Sports Science and Engineering, 03 (01), 50-64, 2009.

[6] Zantop, T., Petersen, W., Sekiya, J. K., Musahl, V., & Fu, F. H. Anterior cruciate ligament anatomy and function relating to anatomical reconstruction. *Knee Surgery, Sports Traumatology, Arthroscopy*, *14*(10), 982-992, 2006.

[7] Mahalingam, V., Wojtys, E. M., Wellik, D. M., Arruda, E. M., & Larkin, L. M.Fresh and Frozen Tissue-Engineered Three-Dimensional Bone–Ligament–Bone Constructs for Sheep Anterior Cruciate Ligament Repair Following a 2-Year Implantation. *BioResearch Open Access*, *5*(1), 289-298, 2016.

[8] Van Kampen, C., Arnoczky, S., Parks, P., Hackett, E., Ruehlman, D., Turner, A., & Schlegel, T. (2013). Tissue-engineered augmentation of a rotator cuff tendon using a reconstituted collagen scaffold: a histological evaluation in sheep. *Muscles, ligaments and tendons journal*, *3*(3), 229-235, 2013.

[9] Weiss, M., Unterhauser, F. N., & Weiler, A. Crimp frequency is strongly correlated to myofibroblast density in the human anterior cruciate ligament and its autologous tendon grafts. *Knee Surgery, Sports Traumatology, Arthroscopy*, *20*(5), 889-895, 2012.

[10] Murray, M. M., Spindler, K. P., Ballard, P., Welch, T. P., Zurakowski, D., & Nanney, L. B. Enhanced histologic repair in a central wound in the anterior cruciate ligament with a collagen–platelet-rich plasma scaffold. *Journal of Orthopaedic Research*, *25*(8), 1007-1017, 2007.

[11] Mayr, H. O., Stoehr, A., Herberger, K. T., Haasters, F., Bernstein, A., Schmal, H., & Prall, W. C. Histomorphological Alterations of Human Anterior Cruciate Ligament Grafts During Mid-Term and Long-Term Remodeling. *Orthopaedic Surgery*, *13*(1), 314-320, 2021

[12] Marieswaran, M., Jain, I., Garg, B., Sharma, V., & Kalyanasundaram, D. A Review on Biomechanics of Anterior Cruciate Ligament and Materials for Reconstruction. *Applied Bionics and Biomechanics*, 2018

[13] Doblaré, M., & Merodio, J. (2015) An Introduction to Biomechanics and Mechanobiology., 1-37, EOLSS Publications

[14] Sensini, A., & Cristofolini, L. Biofabrication of Electrospun Scaffolds for the Regeneration of Tendons and Ligaments. *Materials*, *11*(10), 1963, 2018.

[15] J. J. Collins, “The redundant nature of locomotor optimization laws,” *Journal of Biomechanics*, vol. 28, no. 3, 1994.

[16] Morrison, J. B. (1970). The mechanics of the knee joint in relation to normal walking. *Journal of Biomechanics*, *3*(1), 51-61. https://doi.org/https://doi.org/10.1016/0021-9290(70)90050-3

[17] Griffin, L. Y., Albohm, M. J., Arendt, E. A., Bahr, R., Beynnon, B. D., DeMaio, M., Dick, R. W., Engebretsen, L., Garrett, W. E., Hannafin, J. A., Hewett, T. E., Huston, L. J., Ireland, M. L., Johnson, R. J., Lephart, S., Mandelbaum, B. R., Mann, B. J., Marks, P. H., Marshall, S. W., . . . Yu, B. Understanding and Preventing Noncontact Anterior Cruciate Ligament Injuries: A Review of the Hunt Valley II Meeting, *The American Journal of Sports Medicine*, *34*(9), 1512-1532, 2006.

[18] Woo, S. L. Y., Hollis, J. M., Adams, D. J., Lyon, R. M., & Takai, S. Tensile properties of the human femur-anterior cruciate ligament-tibia complex. *The American Journal of Sports Medicine*, *19*(3), 217-225, 1991.

[19] Hosseinzadeh, S., & Kiapour, A. M. Age-related changes in ACL morphology during skeletal growth and maturation are different between females and males. *Journal of Orthopaedic Research*, *39*(4), 841-849, 2021.

[20] Hasegawa, A., Otsuki, S., Pauli, C., Miyaki, S., Patil, S., Steklov, N., Kinoshita, M., Koziol, J., D'Lima, D. D., & Lotz, M. K. Anterior cruciate ligament changes in the human knee joint in aging and osteoarthritis. *Arthritis & Rheumatism*, *64*(3), 696-704. 2012

[21] Noyes, F. and E. Grood, The Strength of the Anterior Cruciate Ligament in Humans and Rhesus. J Bone Joint Surg Am, 58, 1074-1082, 1976.

[22] Hashemi, J., Chandrashekar, N., Mansouri, H., Slauterbeck, J. R., & Hardy, D. M. The human anterior cruciate ligament: Sex differences in ultrastructure and correlation with biomechanical properties. *Journal of Orthopaedic Research*, *26*(7), 945-950. 2021

[23] Chandrashekar, N., Mansouri, H., Slauterbeck, J., & Hashemi, J. Sex-based differences in the tensile properties of the human anterior cruciate ligament. *Journal of Biomechanics*, *39*(16), 2943-2950, 2006.

[24] Rossetti, L., Kuntz, L. A., Kunold, E., Schock, J., Müller, K. W., Grabmayr, H., Stolberg-Stolberg, J., Pfeiffer, F., Sieber, S. A., Burgkart, R., & Bausch, A. R. The microstructure and micromechanics of the tendon–bone insertion. *Nature Materials*, *16*(6), 664-670. 2017

[25] Shengnan, Q., Bennett, S., Wen, W., Aiguo, L., & Jiake, X. The role of tendon derived stem/progenitor cells and extracellular matrix components in the bone tendon junction repair. *Bone*, *153*, 116172, 2021.

[26] Sensini, A., Massafgra, G., Gotti, C., Tissue Engineering for the Insertions of Tendons and Ligaments: An Overview of Electrospun Biomaterials and Structures, Frontiers in Bioengineering and Biotechnology, 2021.

[27] Lei, T., Tao, Z., Ju, W., Chen, X., Heng, B., Shen, W., & zi, Y. Biomimetic strategies for tendon/ligament-to-bone interface regeneration. *Bioactive Materials*, *6*, 2491-2510, 2021.

[28] Rezende, F. C., Moraes, V. Y., Franciozi, C. E., Debieux, P., Luzo, M. V., & Belloti, J. C. One-incision versus two-incision techniques for arthroscopically assisted anterior cruciate ligament reconstruction in adults. *Cochrane Database Syst Rev*, *12*(12), Cd010875, 2017.

[29] Jonkergouw, A., Van Der List, J. P., & Difelice, G. S. Arthroscopic primary repair of proximal anterior cruciate ligament tears: outcomes of the first 56 consecutive patients and the role of additional internal bracing. *Knee Surgery, Sports Traumatology, Arthroscopy*, *27*(1), 21-28, 2019.

[30] Buerba, R. A., Boden, S. A., & Lesniak, B. Graft Selection in Contemporary Anterior Cruciate Ligament Reconstruction. *JAAOS Global Research & Reviews*, *5*(10), 2021.

[31] Heusdens, C. H. W., Hopper, G. P., Dossche, L., Roelant, E., & Mackay, G. M. Anterior cruciate ligament repair with Independent Suture Tape Reinforcement: a case series with 2-year follow-up. *Knee Surgery, Sports Traumatology, Arthroscopy, 27*(1), 60-67, 2019.

[32] Smith, P. A., & Bley, J. A. Allograft Anterior Cruciate Ligament Reconstruction Utilizing Internal Brace Augmentation. *Arthroscopy Techniques*, *5*(5), e1143-e1147, 2016

[33] Ruiz-Alonso, S., Lafuente-Merchan, M., Ciriza, J., Saenz-del-Burgo, L., & Pedraz, J. L. Tendon tissue engineering: Cells, growth factors, scaffolds and production techniques. *Journal of Controlled Release*, *333*, 448-486, 2021.

[34] Laurent, C., Liu, X., De Isla, N., Wang, X., & Rahouadj, R. Defining a scaffold for ligament tissue engineering: What has been done, and what still needs to be done. *Journal of Cellular Immunotherapy*, *4*(1), 4-9, 2018.

[35] Altman, G. H., Horan, R. L., Lu, H. H., Moreau, J., Martin, I., Richmond, J. C., & Kaplan, D. L. Silk matrix for tissue engineered anterior cruciate ligaments. *Biomaterials*, *23*(20), 4131-4141, 2002.

[36] Araque-Monrós, M. C., Gamboa-Martínez, T. C., Santos, L. G., Bernabé, S. G., Pradas, M. M., & Estellés, J. M. New concept for a regenerative and resorbable prosthesis for tendon and ligament: physicochemical and biological characterization of PLA-braided biomaterial. *J Biomed Mater Res A*, *101*(11), 3228-3237, 2013.

[37] Kuo, C. K., Marturano, J. E., & Tuan, R. S. Novel strategies in tendon and ligament tissue engineering: Advanced biomaterials and regeneration motifs. *BMC Sports Science, Medicine and Rehabilitation*, *2*(1), 20, 2010.

[38] Gurkan, U. A., Cheng, X., Kishore, V., Uquillas, J. A., & Akkus, O. Comparison of morphology, orientation, and migration of tendon derived fibroblasts and bone marrow stromal cells on electrochemically aligned collagen constructs. *J Biomed Mater Res A*, *94*(4), 1070-1079, 2010.

[39] Font Tellado, S., Bonani, W., Balmayor, E. R., Foehr, P., Motta, A., Migliaresi, C., & van Griensven, M. Fabrication and Characterization of Biphasic Silk Fibroin Scaffolds for Tendon/Ligament-to-Bone Tissue Engineering. *Tissue Eng Part A*, *23*(15-16), 859-872, 2017

[40] Deepthi, S., Nivedhitha Sundaram, M., Deepti Kadavan, J., & Jayakumar, R.. Layered chitosan-collagen hydrogel/aligned PLLA nanofiber construct for flexor tendon regeneration. *Carbohydrate Polymers*, *153*, 2016.

[41] Biobrace impant, how it works, consulted at 26-07-2022, http://biorez.com/how-it-works

[42] Poggie. R, Biorez incorporated, FDA approval for the Biobrace implant, April 30, 2021, https://www.accessdata.fda.gov/cdrh_docs/pdf20/K203267.pdf

[43] McMillan, S., Arciero, R., & Ford, E. The next frontier for rotator cuff augmentation? Strength+ bio-induction. *Journal of Orthopaedic Experience & Innovation*, 28081, 2021.

[44] Oh, S. H., Park, I. K., Kim, J. M., & Lee, J. H. In vitro and in vivo characteristics of PCL scaffolds with pore size gradient fabricated by a centrifugation method. *Biomaterials*, *28*(9), 1664-1671, 2007.

[45] Lin, Z., Zhao, X., Chen, S., & Du, C. Osteogenic and tenogenic induction of hBMSCs by an integrated nanofibrous scaffold with chemical and structural mimicry of the bone–ligament connection. *Journal of Materials Chemistry B*, *5*(5), 1015-1027, 2017.

[46] Bosworth, L. A., Lanaro, M., O'Loughlin, D. A., D'Sa, R. A., Woodruff, M. A., & Williams, R. L. (2022). Melt electro-written scaffolds with box-architecture support orthogonally oriented collagen. *Biofabrication*, *14*(1), 015015, 2022.

[47] Robinson, T. M., Hutmacher, D. W., & Dalton, P. D. The Next Frontier in Melt Electrospinning: Taming the Jet. *Advanced Functional Materials*, *29*(44), 1904664, 2019.

[48] Murray, M. M., Kiapour, A. M., Kalish, L. A., Ecklund, K., Freiberger, C., Henderson, R., Kramer, D., Micheli, L., Yen, Y. M., & Fleming, B. C. Predictors of Healing Ligament Size and Magnetic Resonance Signal Intensity at 6 Months After Bridge-Enhanced Anterior Cruciate Ligament Repair. *Am J Sports Med*, *47*(6), 1361-1369, 2019.

[49] Murray, M. M., Fleming, B. C., Badger, G. J., Freiberger, C., Henderson, R., Barnett, S., Kiapour, A., Ecklund, K., Proffen, B., Sant, N., Kramer, D. E., Micheli, L. J., & Yen, Y. M. Bridge-Enhanced Anterior Cruciate Ligament Repair Is Not Inferior to Autograft Anterior Cruciate Ligament Reconstruction at 2 Years: Results of a Prospective Randomized Clinical Trial. *Am J Sports Med*, *48*(6), 1305-1315, 2020.

[50] Sanborn, R. M., Badger, G. J., Yen, Y. M., Murray, M. M., Christino, M. A., Proffen, B., Sant, N., Barnett, S., Fleming, B. C., Kramer, D. E., & Micheli, L. J. Readiness to Return to Sport at 6 Months Is Higher After Bridge-Enhanced ACL Restoration Than Autograft ACL Reconstruction: Results of a Prospective Randomized Clinical Trial. *Orthop J Sports Med*, *10*(2), 23259671211070542, 2022.

[51] Monk, A. P., Davies, L. J., Hopewell, S., Harris, K., Beard, D. J., & Price, A. J. Surgical versus conservative interventions for treating anterior cruciate ligament injuries. *Cochrane Database Syst Rev*, *4*(4), Cd011166, 2016.

[52] Chen, C., Shi, Q., Li, M., Chen, Y., Zhang, T., Xu, Y., Liao, Y., Ding, S., Wang, Z., Li, X., Zhao, C., Sun, L., Hu, J., & Lu, H. Engineering an enthesis-like graft for rotator cuff repair: An approach to fabricate highly biomimetic scaffold capable of zone-specifically releasing stem cell differentiation inducers. *Bioactive Materials*, *16*, 451-471, 2022.

[53] Chae, S., Sun, Y., Choi, Y.-J., Ha, D.-H., Jeon, I., & Cho, D.-W. 3D cell-printing of tendon-bone interface using tissue-derived extracellular matrix bioinks for chronic rotator cuff repair. *Biofabrication*, *13*(3), 035005, 2021.

[54] Rothrauff, B. B., & Tuan, R. S. Cellular therapy in bone-tendon interface regeneration. *Organogenesis*, *10*(1), 2014.

[55] Yang, R., Zheng, Y., Zhang, Y., Li, G., Xu, Y., Zhang, Y., Xu, Y., Zhuang, C., Yu, P., Deng, L., Cui, W., Chen, Y., & Wang, L. Bipolar Metal Flexible Electrospun Fibrous Membrane Based on Metal–Organic Framework for Gradient Healing of Tendon-to-Bone Interface Regeneration, *Advanced Healthcare Materials*, *11*(12), 2200072, 2022.

[56] Youssef, A., Hrynevich, A., Fladeland, L., Balles, A., Groll, J., Dalton, P. D., & Zabler, S. The Impact of Melt Electrowritten Scaffold Design on Porosity Determined by X-Ray Microtomography. *Tissue Eng Part C Methods*, *25*(6), 367-379, 2019.

[57] Shiroud Heidari, B., Ruan, R., Vahabli, E., Chen, P., De-Juan-Pardo, E. M., Zheng, M., & Doyle, B. Natural, synthetic and commercially-available biopolymers used to regenerate tendons and ligaments. *Bioactive Materials*, *19*, 179-197, 2022.

[58] McMaster, R., Hoefner, C., Hrynevich, A., Blum, C., Wiesner, M., Wittmann, K., Dargaville, T. R., Bauer-Kreisel, P., Groll, J., Dalton, P. D., & Blunk, T. Tailored Melt Electrowritten Scaffolds for the Generation of Sheet-Like Tissue Constructs from Multicellular Spheroids *Advanced Healthcare Materials*, *8*(7), 1801326, 2019.

[59] Kade, J. C., & Dalton, P. D. Polymers for Melt Electrowriting. *Advanced Healthcare Materials*, *10*(1), 2001232, 2021.

[60] Eshraghi, S., & Das, S. Mechanical and microstructural properties of polycaprolactone scaffolds with one-dimensional, two-dimensional, and three-dimensional orthogonally oriented porous architectures produced by selective laser sintering. *Acta Biomaterialia*, *6*(7), 2467-2476, 2010.

[61] Castilho, M., Feyen, D., Flandes-Iparraguirre, M., Hochleitner, G., Groll, J., Doevendans, P., Vermonden, T., Ito, K., Sluijter, J., & Malda, J. Melt Electrospinning Writing of Poly-Hydroxymethylglycolide-co-ε-Caprolactone-Based Scaffolds for Cardiac Tissue Engineering. *Advanced Healthcare Materials*, *6*, 2017.

[62] Han, Y., Lian, M., Wu, Q., Qiao, Z., Sun, B., & Dai, K. Effect of Pore Size on Cell Behavior Using Melt Electrowritten Scaffolds [Original Research]. *Frontiers in Bioengineering and Biotechnology*, *9*, 2021.

[63] Dalton, P. D. Melt electrowriting with additive manufacturing principles. *Current Opinion in Biomedical Engineering*, *2*, 49-57, 2017.

[64] Haag, H., Dalton, P. D., & Bloemen, V. The Synergy of Biomimetic Design Strategies for Tissue Constructs. *Advanced Functional Materials*. 2022.

[65] Saidy, N. T., Fernández-Colino, A., Heidari, B. S., Kent, R., Vernon, M., Bas, O., Mulderrig, S., Lubig, A., Rodríguez-Cabello, J. C., Doyle, B., Hutmacher, D. W., De-Juan-Pardo, E. M., & Mela, P. Spatially Heterogeneous Tubular Scaffolds for In Situ Heart Valve Tissue Engineering Using Melt Electrowriting. *Advanced Functional Materials, 32*(21), 2022.

[66] Xiong, J., Wang, H., Lan, X., Wang, Y., Wang, Z., Bai, J., Ou, W., Cai, N., Wang, W., & Tang, Y. Fabrication of bioinspired grid-crimp micropatterns by melt electrospinning writing for bone–ligament interface study. *Biofabrication, 14*(2), 2022.

[67] Hochleitner, G., Chen, F., Blum, C., Dalton, P. D., Amsden, B., & Groll, J. Melt electrowriting below the critical translation speed to fabricate crimped elastomer scaffolds with non-linear extension behaviour mimicking that of ligaments and tendons. *Acta Biomaterialia, 72*, 110-120, 2018.

[68] Kiss, R. S. Development Of Crimped Fibrous Scaffolds For Ligament Tissue Engineering Using Melt Electrowriting (MEW), 2021. [Master's thesis, Trinity College Dublin, school of engineering, department of Biomedical engineering]

[69] Saidy, N. T., Fernández-Colino, A., Heidari, B. S., Kent, R., Vernon, M., Bas, O., Mulderrig, S., Lubig, A., Rodríguez-Cabello, J. C., Doyle, B., Hutmacher, D. W., De-Juan-Pardo, E. M., & Mela, P. Spatially Heterogeneous Tubular Scaffolds for In Situ Heart Valve Tissue Engineering Using Melt Electrowriting. *Advanced Functional Materials, 32*(21), 2022.

[70] Eichholz, K. F., Gonçalves, I., Barceló, X., Federici, A. S., Hoey, D. A., & Kelly, D. J. How to design, develop and build a fully-integrated melt electrowriting 3D printer. *Additive Manufacturing, 58*, 2022.

[71] Afghah, F., Dikyol, C., Altunbek, M., & Koc, B. Biomimicry in Bio-Manufacturing: Developments in Melt Electrospinning Writing Technology Towards Hybrid Biomanufacturing. *Applied Sciences, 9*(17), 2019.

[72] Hrynevich, A., I. Liashenko, and P.D. Dalton, Accurate Prediction of Melt Electrowritten Laydown Patterns from Simple Geometrical Considerations. Advanced Materials Technologies, 2020. 5(12)

[73] Beyer, W. H. (Ed.). CRC Standard Mathematical Tables, 28th ed. Boca Raton, FL: CRC Press, p. 125, 1987.

[74] E.W. Yates, A. Rupani, G.T. Foley, W.S. Khan, S. Cartmell, S.J. Anand, Ligament Tissue Engineering and Its Potential Role in Anterior Cruciate Ligament Reconstruction, Stem Cells International, 2012.

[75] Eichholz, K. F., & Hoey, D. A. Mediating human stem cell behaviour via defined fibrous architectures by melt electrospinning writing. *Acta Biomaterialia, 75*, 140-151, 2018.

[76] Hochleitner, G., Jüngst, T., Brown, T. D., Hahn, K., Moseke, C., Jakob, F., Dalton, P. D., & Groll, J. Additive manufacturing of scaffolds with sub-micron filaments via melt electrospinning writing. *Biofabrication, 7*(3), 035002, 2015.

[77] Leathers, M. P., Merz, A., Wong, J., Scott, T., Wang, J. C., & Hame, S. L. Trends and Demographics in Anterior Cruciate Ligament Reconstruction in the United States. *J Knee Surg, 28*(5), 390-394, 2015.

[78] Norris, R., Thompson, P., & Getgood, A. The effect of anterior cruciate ligament reconstruction on the progression of osteoarthritis. *Open Orthop J, 6*, 506-510, 2012

[79] Schilaty, N. D., Nagelli, C., Bates, N. A., Sanders, T. L., Krych, A. J., Stuart, M. J., & Hewett, T. E. Incidence of Second Anterior Cruciate Ligament Tears and Identification of Associated Risk Factors From 2001 to 2010 Using a Geographic Database. *Orthopaedic Journal of Sports Medicine*, 2017.

[80] Ragaert, K., De Baere, I., Cardon, L., & Degrieck, J. Bulk mechanical properties of thermoplastic poly-e-caprolactone. In 6th Polymers & Mould Innovations International Conference, 339-344, 2014.

[81] Rao. S, (2017) Mechanical vibrations, 6th edition, Pearson.

[82] Gudas, R., Rimkūnas, A., & Staškūnas, M. Large-Diameter Anterior Cruciate Ligament Reconstruction Technique With 8-Strand Semitendinosus and Gracilis Graft. *Arthroscopy Techniques*, *10*(4), e981-e986, 2021.

[83] Rothrauff, B. B., Lauro, B. B., Yang, G., Debski, R. E., Musahl, V., & Tuan, R. S. Braided and Stacked Electrospun Nanofibrous Scaffolds for Tendon and Ligament Tissue Engineering. *Tissue Eng Part A*, *23*(9-10), 378-389, 2017.

[84] Xie, C., Gao, Q., Wang, P., Shao, L., Yuan, H., Fu, J., Chen, W., & He, Y. Structure-induced cell growth by 3D printing of heterogeneous scaffolds with ultrafine fibers. *Materials & Design*, *181*, 108092, 2019.

[85] Bertlein, S., Hochleitner, G., Schmitz, M., Tessmar, J., Raghunath, M., Dalton, P. D., & Groll, J. Permanent Hydrophilization and Generic Bioactivation of Melt Electrowritten Scaffolds [https://doi.org/10.1002/adhm.201801544]. *Advanced Healthcare Materials*, *8*(7), 1801544, 2019.

List of Appendices

Appendix 1: Tri-phasic code used to print the crimped wave pattern scaffold.

```
'Axis 4 = pressure
SERVO AXIS(4)=OFF
pressure=0.5 'Bar
DAC AXIS(4)=(pressure/10)*2048

'Axis 6 = current (3mA max) scale:0-2048
SERVO AXIS(6)=OFF
DAC AXIS(6)=10

'Axis 5 = voltage
SERVO AXIS(5)=OFF
initial_voltage=6 'kV
voltage=initial_voltage
DAC AXIS(5)=(voltage/30)*2048

raster_speed1=3.6'(mm/s)
raster_speed2=19'(mm/s)
raster_accel=1000 '(mm/s/s)
raster_decel=1000
pause=200 '(ms) variable

pore_size_x=0.5 '(mm)
pore_size_y=0.35 '(mm)
layer_number=10 '
wave_length=0.3 '(mm) variable
height=0.048 '(mm) variable
end_x=wave_length/2
end_y=0 '(mm) variable


length_x=10 'amount of waves, has to be dividable by 5
length_y=4 'amount of fibres, actual amount will be (length_y * 2+1)
printing_distance_y1=1.4 '(pore_size_y * lenght_y)
printing_distance_y2=1.05 '(pore_size_y *(lenght_y-1)
extra_side_x=2 '(mm) extra space before turning
extra_side_y=5
```

```
scaffold_x=(length_x*wave_length*2)+2*extra_side_x '(mm) total lenght of scaffold
scaffold_y=(length_y*(pore_size_y*(2+1))+2*extra_side_y)
straight_fibre_number=(length_x*wave_length)/pore_size_x ' amount of vertical fibres


FWD_IN AXIS(0)=0 'limit switch end of carriage away from motor. Forward direction is motion of carriage away from motor
REV_IN AXIS(0)=1
FWD_IN AXIS(1)=2
REV_IN AXIS(1)=3
FWD_IN AXIS(2)=4
REV_IN AXIS(2)=5


BASE(0)
ATYPE=43
SPEED=raster_speed1
ACCEL=raster_accel
DECEL=raster_decel

BASE(1)
ATYPE=43
SPEED=raster_speed1
ACCEL=raster_accel
DECEL=raster_decel
WDOG=ON

BASE(0,1,2) 'set base array

MOVE(10,0)
WAIT IDLE
WA(pause)

layer=0
REPEAT
  MOVE(0,-extra_side_y)
  MOVE(0,-pore_size_y) 'move down initially with extra side y
  l=0
  REPEAT
    WAIT IDLE
```

```
    WA(pause)
    MOVE(extra_side_x,0) 'move right initially with extra side x
    WAIT IDLE
    WA(pause)
    'part with the wavy line starts now
    i=0
    REPEAT
        MOVE(end_x,-height)
        MOVE(end_x,height)
        MOVE(end_x,height)
        MOVE(end_x,-height)
        i=i+1
    UNTIL i=length_x 'repeat length_x times
    MOVE(extra_side_x,0)
    MOVE(0,-printing_distance_y1)
    WAIT IDLE
    WA(pause)
    MOVE(-extra_side_x,0)

    'repeat in opposite direction
    j=0
    REPEAT
        MOVE(-end_x,height)
        MOVE(-end_x,-height)
        MOVE(-end_x,-height)
        MOVE(-end_x,height)
        j=j+1
    UNTIL j=length_x  'repeat length_x times
    MOVE(-extra_side_x,0)
    MOVE (0,printing_distance_y2)
    l=l+1
UNTIL l=length_y

MOVE(0,printing_distance_y1)
MOVE(0,pore_size_y)
' return to original side.
MOVE (extra_side_x,0)
k=0
REPEAT
    MOVE(end_x,-height)
```

```
    MOVE(end_x,height)
    MOVE(end_x,height)
    MOVE(end_x,-height)
    k=k+1
  UNTIL k=length_x 'repeat length_x times
  MOVE(extra_side_x,0)
  WA(pause)
  MOVE(0,extra_side_y)
  WAIT IDLE
  WA(pause)

  MOVE(-extra_side_x,0)
  WAIT IDLE
  WA(pause)



  BASE(0) ' speed increase for the fibres in y direction.`
  ATYPE=43
  SPEED=raster_speed2
  ACCEL=raster_accel
  DECEL=raster_decel

  BASE(1)
  ATYPE=43
  SPEED=raster_speed2
  ACCEL=raster_accel
  DECEL=raster_decel
  WDOG=ON

  BASE(0,1,2) 'set base array
  MOVE(0,-scaffold_y)
  WAIT IDLE
  WA(pause)
  WA(pause)
' print the vertical fibres
  p=0
  REPEAT
    MOVE(-pore_size_x,0)
    WAIT IDLE
```

```
    WA(pause)
    WA(pause)
    MOVE(0,scaffold_y)
    WAIT IDLE
    WA(pause)
    WA(pause)
    MOVE(-pore_size_x,0)
    WAIT IDLE
    WA(pause)
    WA(pause)
    MOVE(0,-scaffold_y)
    WAIT IDLE
    WA(pause)
    WA(pause)
    p=p+1
UNTIL p=straight_fibre_number
WAIT IDLE
WA(pause)

'change the speed back



BASE(0)
ATYPE=43
SPEED=raster_speed1
ACCEL=raster_accel
DECEL=raster_decel

BASE(1)
ATYPE=43
SPEED=raster_speed1
ACCEL=raster_accel
DECEL=raster_decel
WDOG=ON

BASE(0,1,2) 'set base array

WAIT IDLE
WA(pause)
WA(pause)
```

```
   MOVE(-extra_side_x,0)
   MOVE(0,scaffold_y)
   WAIT IDLE
   WA(pause)
   layer=layer+1

UNTIL layer=layer_number 'repeat layer_number times

WAIT IDLE
WA(pause)
MOVE (-10,0)
DAC AXIS(5)=0 ‘ these three lines turn the machine off after print
DAC AXIS (4)=0
OP(18,OFF)
```

Appendix 2: Tri-phasic code used to print diamond scaffold

```
'Axis 4 = pressure
SERVO AXIS(4)=OFF
pressure=0.5 'Bar
DAC AXIS(4)=(pressure/10)*2048

'Axis 6 = current (3mA max) scale:0-2048
SERVO AXIS(6)=OFF
DAC AXIS(6)=10

'Axis 5 = voltage
SERVO AXIS(5)=OFF
voltage=6.0'kV
DAC AXIS(5)=(voltage/30)*2048

raster_speed=9'(mm/s)
raster_accel=500 '(mm/s/s)
raster_decel=1000
pause=250 '(ms)
pore_size=0.25 '(mm)
length_x=50
length_y=6.139 ‘has to be adjusted based on angle of scaffold printed.
layer_number=20
fibres = 5
fibres1=fibres
difx = 2
corner=11
cornerx=6
cornery=0.639
scaffold=fibres*0.5+corner*0.5
FWD_IN AXIS(0)=0 'limit switch end of carriage away from motor. Forward direction is motion of carriage away from motor
REV_IN AXIS(0)=1
FWD_IN AXIS(1)=2
REV_IN AXIS(1)=3
FWD_IN AXIS(2)=4
REV_IN AXIS(2)=5
```

```
BASE(0)
ATYPE=43
SPEED=raster_speed
ACCEL=raster_accel
DECEL=raster_decel
BASE(1)
ATYPE=43
SPEED=raster_speed
ACCEL=raster_accel
DECEL=raster_decel
WDOG=ON

BASE(0,1,2) 'set base array
MOVE(10,0)
WAIT IDLE
WA(pause)
layer=0
REPEAT
  k=0
  REPEAT ‘fill the corner first
    cornerx = cornerx + difx
    cornery = cornery + pore_size
    MOVE(cornerx,-cornery)
    WAIT IDLE
    WA(pause)
    MOVE(difx,0)
    WAIT IDLE
    WA(pause)
    cornerx = cornerx + difx
    cornery = cornery + pore_size
    MOVE(-cornerx,cornery)
    WAIT IDLE
    WA(pause)
    MOVE(0,pore_size)
    k=k+1
  UNTIL k=corner

  j=0 ‘ the diagonal lines crossing the entire scaffold
  REPEAT
```

```
    MOVE(length_x,-length_y)
    WAIT IDLE
    WA(pause)
    MOVE(0,pore_size)
    MOVE(-length_x,length_y)
    WAIT IDLE
    WA(pause)
    MOVE(0,pore_size)
    j=j+1
UNTIL j=fibres

l=0
REPEAT ‘fill the opposite corner
    MOVE(cornerx,-cornery)
    WAIT IDLE
    WA(pause)
    MOVE(0,pore_size)
    WAIT IDLE
    WA(pause)
    cornerx = cornerx - difx
    cornery = cornery - pore_size
    MOVE(-cornerx,cornery)
    WAIT IDLE
    WA(pause)
    MOVE(difx,0)
    cornerx = cornerx - difx
    cornery = cornery - pore_size
    l=l+1
UNTIL l=corner
MOVE(cornerx,0)
MOVE(difx,0)
MOVE(0,-scaffold)
MOVE(-difx,0)
m=0
REPEAT ‘repeat for fibres with the opposite angle
    cornerx = cornerx + difx
    cornery = cornery + pore_size
    MOVE(-cornerx,-cornery)
    WAIT IDLE
    WA(pause)
```

```
   MOVE(-difx,0)
   WAIT IDLE
   WA(pause)
   cornerx = cornerx + difx
   cornery = cornery + pore_size
   MOVE(cornerx,cornery)
   WAIT IDLE
   WA(pause)
   MOVE(0,pore_size)
   m=m+1
UNTIL m=corner
p=0
REPEAT
   MOVE(-length_x,-length_y)
   WAIT IDLE
   WA(pause)
   MOVE(0,pore_size)
   MOVE(length_x,length_y)
   WAIT IDLE
   WA(pause)
   MOVE(0,pore_size)
   p=p+1
UNTIL p=fibres
n=0
REPEAT
   MOVE(-cornerx,-cornery)
   WAIT IDLE
   WA(pause)
   MOVE(0,pore_size)
   WAIT IDLE
   WA(pause)
   cornerx = cornerx - difx
   cornery = cornery - pore_size
   MOVE(cornerx,cornery)
   WAIT IDLE
   WA(pause)
   MOVE(-difx,0)
   cornerx = cornerx - difx
   cornery = cornery - pore_size
   n=n+1
```

```
    UNTIL n=corner
    MOVE(-cornerx,0)
    MOVE(-difx,0)
    MOVE(0,-scaffold)
    MOVE(difx,0)
    layer=layer+1
UNTIL layer=layer_number
MOVE(-10,0)
DAC AXIS(5)=0 ' turns the machine off after print
DAC AXIS(4)=0
OP(18,OFF)
```

Appendix 3: Standard Operating Procedure for operating the MEW printer.

SOP – MEW (Parsons) operating procedure

SOP #: MEW-1 **Implementation Date: 09/09/2020**

Revision #: 02 **Approval Authority: Angelica Federici**

Note this is a general protocol to be used as a reference for trained users. It is not an extensive list containing all of the necessary instructions. Please get training before carrying out any of the below work.

Start-up

1. Before starting:
    - On the high voltage power supply, ensure the toggle switch is set to “Ext” (left position), and the current and voltage dials are turned fully counter-clockwise
    - On the control boxes, ensure all switches are in the OFF (down) position
    - **Ensure EMERGENCY STOP button is reset (not activated)**
    - Turn on the computer (PW: Bioengineering!)
    - Turn on the air pressure at the outlet and set to 1/1.5 psi: open valve using tool, ensure meter on right is around 100. Using black knob, turn clockwise until meter on right reaches 1 bar

Ensure toggle switch is set to “Ext” (left position)

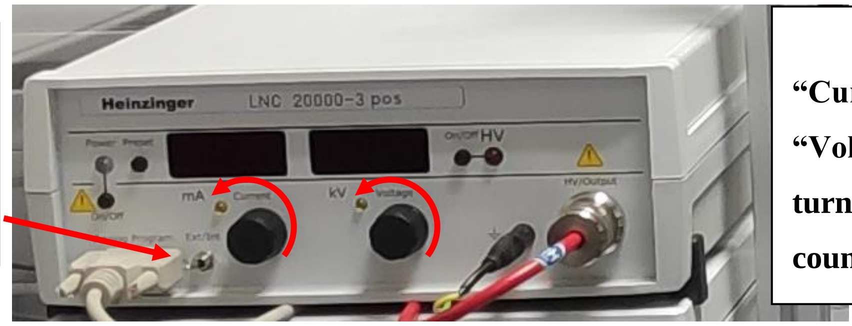

Ensure “Current” and “Voltage” dials are turned fully counter-clockwise

2. Load a syringe in the print head
3. Turn on the “DinoCapture” software on the computer and ensure the camera is adequately positioned
4. Close the door of the enclosure
5. Turn on power strip underneath desk
6. Turn on the temperature controller in this specific order:
    - Fan: two small wires on top of controller box
    - Controller: switch on front of box
    - Heater: two large plugs at back of box

NB: Ensure that temperatures start converging to the set-point within 10 seconds of powering on. If temperatures either [A. Do not begin rising] or [B. Rise above the set point without dropping within 10 seconds], power off the controller immediately.

7. Turn on the “CONTROLLER POWER” switch on the main control box (check that the main bottom light turned on)
8. Start the “Motion Perfect” software on the computer and wait until software fully initialized and establish a connection in synchronized mode (bottom right-hand corner)
9. Press “Drive Enable” bottom on the software
10. Press the “RESET” button on the main control box (check that the green light is on)
11. Run the “INITIALISE_SYSTEM” program, ensure “ready” appears at bottom left
    NB: Do not change the “INITIALISE_SYSTEM” program.
12. Establish needle hight (5mm) by aligning with line on black tool by adjusting the Z-direction (Axis 2)

NB: Keep hand on the EMERGENCY STOP button and push if it appears the needle may strike the print plate

Reset procedure

If the Emergency stop button is pressed, follow the below procedure to restart the system:

1. Twist the E-Stop button to retract it
2. Click on the “Motion Stop” icon in the Motion Perfect software

```
' Draws square-plus
start:
  basespeed=320
  baseaccel=222
  tickswait=2000
  baseaxis=1
  setatypes=FALSE
  servostate=ON

' Initialize axes
```

3. Click on the “Drive enable” button in the Motion Perfect software
4. Press the reset button on the main control box
5. Verify that all lights on the main box are turned on again

13. Define initial variables in the “SET_AUXILARY_VARIABLES” program and run
14. Turn on the “PRESSURE” switch on the main control box
15. Move the print head to the back-left corner of the print plate by adjusting the X and Y directions (Axes 0 and 1)
16. Using “SET_AUXILLARY_VARIABLES” script, increase pressure to 0.5 Bar (up to 1 if needed) and wait until material begins extruding from needle. Do not change voltage or current.

17. **Once material is extruding**, turn on the “HV POWER” switch on the back of the HV control box
18. Press the “On/Off” button on the LEFT side of the high voltage power supply (under the “Power” light).
19. Turn on the “VOLTAGE” switch on the main control box
20. Using “SET_AUXILLARY_VARIABLES” script, increase voltage starting at 2 kV up to 6/6.5 KV until polymer droplet begins to drop. Once polymer hits the build plate, move the needle away to prevent material sticking to the extruder.
21. Begin “Raster Test” script using a velocity of 1mm. After 10ish minutes to ensure the material is homogeneous, begin increasing the velocity until the critical transition speed is reached (polymer stretches the same amount in both directions)
22. Run desired script using ideal variables found when tuning.

Shut down

1. Move the print head away from the scaffold
2. Turn off the “VOLTAGE” switch on the main control box
3. Turn off the “HV POWER” switch on the back of the HV control box, after turning off the button in the front
4. Turn off the “PRESSURE” switch on the main control box and close the air pressure at the outlet
5. Turn off the temperature controller box in this specific order (temperature plug, wait until the temperature is below 50, turn of the controller and the fan)
6. Close the “Motion Perfect” and “DinoCapture” software on the computer
7. Turn off the “CONTROLLER POWER” switches on the main control box
8. You can now open the door to remove you scaffold
9. Turn off the socket extension under the desk.

NB: Do not scratch the print plate. Use plastic tweezers if possible. Make sure you are not wearing jewelry that may scratch the print plate.

Appendix 4: Standard Operating Procedure for operating the Zwick mechanical tester.

ZWICK

Fundamentals

1. Changing the load cell
2. Starting Up
3. Checking the State of the load cell.
4. Reference the platens
5. Before you start testing

- Changing the load cell

Always do this with the machine switched off ie the isolator at the back of the machine

Attach load cell using the pin and then connect the plug at the back of the machine.
Vice versa for taking out the load cell.
Please be careful not to drop the load cell when taking it out.

If using the 50N of 5N cells remember how delicate they are ie. don't put any torsion on the cell when screwing it in.

- Starting Up

Switch on the isolator on the back of the machine, then open the software
Open your folder
Open the desired test method

You will be prompted to press the on button on the machine ie. To make the link.
If the Ct value on the bottom of the screen corresponds with the actual position of the crosshead then switch on the machine

When switching off close down the software and then switch off the isolator.

To start a method, it is best to copy someone else’s method into your folder and edit it and then save it as your own.
First put a folder with your name on it on the c drive or desktop

Click open on a test method of your choosing
When you open a file in that folder if a method does not show up in the large dialog box, then it is not a method file.

Once you have found it and opened it choose save as and save it to your folder. Now if you closed down and reopen it from your folder you can’t damage their method. Now you are free to edit the method file to suit yourself.

- Checking the state of the load cell before testing

Open Machine icon at the top left had corner of the screen
Click “expanded” in the bottom right hand corner of the window that opens
Then double click the load cell in this window
Then click “state”
Then you will see if it has been overloaded before and if so when
Then open the log book and sign in.
If the load cell has been overloaded make a note of it in the log book.

- Reference the platens

Attach the compression platens or tensile grips
The pins should slide in easily, if they don’t, don’t force them.

When the compression platens or tensile grips are in position
Use the positioning buttons to move the platens close together without touching

WHEN YOU GET CLOSE WITH THE PLATENS JUST GENTLY TAP THE POSITIONING BUTTON. THIS TAKES PRACTISE.

Zero the force on the load cell by clicking on the icon at the top of the screen

Go into machine at top of screen
Choose crosshead
Pick reference

Choose a low force value ie. Max 1.0 Newton for a 200 N load cell
.05 N for 5 Newton Load Cell
Choose a slow speed ie. 1mm/minute

Click reference

When the reference is completed close the reference dialog box but don't close the machine dialog box behind it.
In here you will see upper and lower softend
Click the A beside lower softend
This will make the lower software limit the same as the crosshead value which is in the bottom right hand corned of the machine

- Before you start testing

At this stage you have edited and saved your method and you are ready to start testing
<u>So you want to save the series in advance(so that you will have all the graphs etc to replay if needed)</u>

Click "Save as" from top menu
Choose ZSE(For test series) on bottom of dialog box
Choose a generic filename of your choosing
Click Ok
Make sure it's saving in your folder or where you want it

<u>Now you want to set up the raw data files</u>
<u>It will save these automatically and number them</u>
So choose "Export Interfaces" at top of screen under File
Choose graphs

Click edit
Choose generic filename of your choosing and dictate the path that it will go to ie. its folder
Choose automatic numbering
Go into channels and check that you are exporting the channels that you require ie. Force(N) standard travel(mm)

Use **tab** and **dot period** as the settings for the output file which will be a TRA file Then click ok
No need to click export now

Then start testing
It will ask you at the end of all your tests if you want to save the series
It will automatically save the individual raw data files that it has exported using automatic numbering.
If you open excel and then choose all files and then open one of the raw data TRA files, choose delimited, select comma and then finish.
It will open for you and when you are finishing save it as an excel workbook.

Appendix 5: Link to google drive folder containing videos of Ansys FEA simulations

A few videos from the FEA simulations have been placed in the google doc folder below to better illustrate the oscillation problem as well as videos of the simulated biphasic designs. Both URL’s lead to the same file in google docs.

HTTPS://DRIVE.GOOGLE.COM/DRIVE/FOLDERS/1FPFMULDWBRWQ8C2CNIQRVMCV8RQJF4UE?USP=SHARING

HTTPS://TINYURL.COM/ANSYSVID